Charles University in Prague

Faculty of Mathematics and Physics

DOCTORAL THESIS

Jan Fikáček

Physical phenomena in Ytterbium- and Cerium-based compounds

Department of Condensed Matter Physics

Supervisor of the doctoral thesis: prof. RNDr. Vladimír Sechovský, DrSc.

Study programme: Physics (P1701)
Specialization: Physics of Condensed Matter and Materials Research

Prague 2014

Acknowledgements

Here I would like to thank especially to professor Vladimír Sechovský, my supervisor, who led me during the past four years of my PhD studies. His wide knowledge of the problematic of strongly electron systems and many ideas helped me most during experimental investigations and writing publications.

Great thanks belong to Dr. Jeroen Custers. Without his revisions of the text and many suggestions for interpretation of the data during the past three years, I would not be able to finish the thesis in the actual shape.

I would like to acknowledge Dr. Jiří Prchal for his advices and leadership during performing electrical resistivity and high-pressure measurements and many others.

Big thanks belong to Dr. Jan Prokleška for the measurements of dilatometry around the structural transitions in CeRuSn, many useful advices during performing of almost all experiments at cryogenic temperatures and many ideas for explanation of the measured data.

I would also like to acknowledge to Dr. Ivana Císařová for measurements of X-ray single crystal diffraction on CeRuSn and Dr. Martin Míšek for measurements of electrical resistivity under high-pressure on CeRuSn at high temperatures.

I must not forget about Dr. Jiří Pospíšil, who taught me how to perform the Czochralski method and his hints during single-crystals separation.

Many thanks belong to Dr. Stanislav Daniš for his help during single-crystal orientation and solving of X-ray powder diffraction patters.

I declare that I carried out this doctoral thesis independently, and only with the cited sources, literature and other professional sources.

I understand that my work relates to the rights and obligations under the Act No. 121/2000 Coll., the Copyright Act, as amended, in particular the fact that the Charles University in Prague has the right to conclude a license agreement on the use of this work as a school work pursuant to Section 60 paragraph 1 of the Copyright Act.

In Prague date 10.6.2014 signature

Název práce: Fyzikální jevy ve sloučeninách na bázi Ytterbia a Ceru

Autor: Jan Fikáček

Katedra / Ústav: Katedra fyziky kondenzovaných látek

Vedoucí doktorské práce: prof. RNDr. Vladimír Sechovský, DrSc., Katedra fyziky kondenzovaných látek, Matematicko-fyzikální fakulta, Univerzita Karlova v Praze

Abstrakt: tato práce se zabývá studium sloučeniny CeRuSn vykazuje dva strukturní přechody v 290 and 256 K oba spojené s velkou teplotní hysterezí. Během nich dochází ke kontrakci podél osy c. V nízkých teplotách se sloučenina uspořádává antiferomagneticky pod teplotou 2.8(1) K. Silná magnetokrystalová anisotropie je způsobena výskytem velmi zkrácených Ce-Ru vzdáleností přibližně podél osy c. V důsledku silné hybridizace se 2/3 Cerových atomů vyskytují ve stavu neceločíselné valence.

Prvotně připravené monokrystaly sloučenin $YbPt_2Si_2$ a $Yb_2Pt_3Si_5$ se neuspořádávají magneticky. Maximum pozorovatelné v teplotní závislosti magnetizace je u nich způsobeno teplotou vyvolanou populací magnetického 3+ stavu atomů Ytterbia.

Klíčová slova: Cer, Ytterbium, neceločíselná valence, magnetické uspořádání

Title: Physical phenomena in Ytterbium- and Cerium-based compounds

Author: Jan Fikáček

Department / Institute: Department of Condensed Matter Physics

Supervisor of the doctoral thesis: prof. RNDr. Vladimír Sechovský, DrSc.
Department of Condensed Matter Physics, Charles University in Prague

Abstract:

This work contains a study of CeRuSn, which undergoes two structural transitions at 290 K and 256 K both connected with large temperature hysteresis. During the transitions the lattice shrinks along the *c*-axis. At low temperatures the compound orders antiferromagnetically below 2.8(1) K. A strong magnetocrystalline anisotropy is caused by very shortened Ce-Ru separations pointing approximately along the *c*-axis. Due to a strong hybridization, two thirds of Cerium atoms are in a non-integer valence state.

For the first time synthesized single-crystals of $YbPt_2Si_2$ a $Yb_2Pt_3Si_5$ show no magnetic ordering. A maximum, which is visible in the temperature dependences of magnetic susceptibility originate in thermal population of the magnetic Yb^{3+} state.

Keywords: Cerium, Ytterbium, non-integer valence, magnetic ordering

Contents

Introduction

This thesis is dealing with Cerium and Ytterbium intermetallic compounds, which were prepared and studied in the facilities of the Department of Condensed Matter Physics on Charles University in Prague.

The text is divided into seven chapters and further subsections. In the second chapter there is a theoretical background starting from physical properties of Cerium and Ytterbium compounds and ending with a theory needed for experimental methods. The third chapter gives details about experiments used in this thesis. The fourth chapter includes a study of CeRuSn. During our investigations, the problematic of this compound appeared to be so interesting that it consumes the biggest portion of the thesis. Due to that, the fifth and sixth part presents results of basic measurements of two Ytterbium compounds, $YbPt_2Si_2$ and $Yb_2Pt_3Si_5$. The thesis ends with the chapter number seven where an outlook of the thesis and future research plans are sketched.

The first part of results is dedicated to CeRuSn, which appeared during its investigation to be a very unique case of a Cerium compound, where a coexistence of Cerium atoms with different valence states can be found. The crystal structure of this compound is very sensitive to external conditions such as temperature and external pressure. CeRuSn undergoes both structural and magnetic phase transitions where an illustrative connection between crystal structure, Cerium valence and magnetic properties can be observed. Our study involved all steps of experimental investigation, from the synthesis and characterization, to the measurements of physical properties where some of them were additionally probed under high hydrostatic pressure. The reader should obtain a consistent picture about the very interesting physics, which can be found in CeRuSn.

The second and third part of results deal with $YbPt_2Si_2$ and $Yb_2Pt_3Si_5$. The two Ytterbium-based compounds were for the first time prepared in single crystal form by the solvent growth method. The second single crystal was not only synthesized as a novel compound, but it was also obtained in a very high quality. Because most of the time was devoted to the study of CeRuSn, the part on the Yb compounds became considerably shorter. Nevertheless we measured basic physical properties under ambient conditions and also electrical resistivity under high

pressure, which prove that these Ytterbium compounds are far from the magnetic QCP, where a magnetic ordering would be induced by pressure.

In the last chapter we summarize the findings from our investigations and give an idea about future plans for the study of these and other Ytterbium and Cerium compounds.

1. Theoretical background

In this part, a basic theoretical background will be presented in order to support the reader to understand the physics, which will be discussed in this thesis. At first we will focus on rare earth intermetallic compounds with emphasis on Cerium- and Ytterbium-based ones. In the next step, we will provide a theory for experimental methods mentioned in the following chapter.

1.1. Magnetism of *f*-electron systems

When one seeks interesting groups of magnetic materials, there are not many such fascinating like those with partially filled 4*f*-shell. Lanthanides are located in the periodic table of elements between lanthanum (La^{57}) and lutetium (Lu^{71}). Together with scandium (Sc^{21}) and yttrium (Y^{39}) they form the group of rare earth elements. Their electronic configuration can be described by xenon´s electron configuration with additional valence electrons. Among them the chemical properties are very similar due to the same outermost shells $5s^2$ $5p^6$, but they differ in the 4*f* shell, which is gradually populated by electrons when going from lanthanum towards lutetium. This is accompanied by the so-called Lanthanide contraction, where the ionic radius decreases continuously through the series. Magnetic properties are mostly governed by indirect interactions due to the fact that the partially filled 4*f*-shell is well screened by other electrons and spreads only approximately 0.3 Å from the core. Most rare-earth based compounds are magnetically ordered at low temperatures. More intriguing, in a few cases they are both magnetic and superconducting.(1,2)

1.1.1. Magnetic moments

In an atom energy levels split into so-called terms, which are characterized by angular momentum L and total spin momentum S given by the sum of each electron´s angular momentum and spin, respectively. Both L and S can have projections into the z-axis, which may attain values between $-L,\ldots,L$ and $-S,\ldots,S$. Thus the electrons in an atom can organize in $(2L+1)(2S+1)$ ways. In case of rare earth ions, it is anticipated that Russel Saunder´s approximation is valid. Coulomb

repulsion is the most important force and spin-orbital interaction is considered only as a perturbation. Owing to the fact that *f*-electrons in rare earths are not much affected by crystal field, because they lie closer to the core than other electrons, we can apply three empirical Hund´s rules in order to determine ground state multiplet of an *f*-metal:

1. Electrons in an atom occupy an atomic orbital in a way that total spin *S* is maximized in concordance with the Pauli Exclusion Principle.

2. For a given *S*, the electrons organize in the shell in order to maximize the orbital angular momentum *L*.

3. The total angular momentum *J* is given by $|L - S|$ for less than half-filled shell and by $L + S$ for more than half-filled shell.

Resulting energy levels in an atom are $(2J+1)$-fold degenerate. Multiplets higher in energy are usually well separated from the lowest one and we may not consider them. An exception is Samarium, where the first excited multiplet is below room temperature and hence cannot be neglected.

An assembly of randomly oriented magnetic moments in the paramagnetic state, which are partly aligned in an external magnetic field, may be described by an effective moment μ_{eff} yielding for given values of *J*, *L* and *S*:

$$\mu_{eff} = g_J \mu_B \sqrt{J(J+1)}, g_J = \frac{3J(J+1) + S(S+1) - L(L+1)}{2J(J+1)} \quad (1)$$

μ_B is the Bohr magneton, g_J is the Landé g-factor reflecting mutual orientation of *J*, *L* and *S* in real space. Tetravalent Cerium has no bounded *f*-electron, so it cannot carry any magnetic moment. The same holds for Yb^{2+}, which has its 4*f*-shell filled up. Magnetic Ce^{3+} ions with $S = ½$, $L = 3$ and $J = 5/2$ have the effective moment $\mu_{\text{eff}} = 2.54\ \mu_B$, while Yb^{3+} has $S = ½$, $L = 3$ and $J = 7/2$ resulting in the effective moment $\mu_{\text{eff}} = 4.54\ \mu_B$. In a magnetically ordered state, magnetic moment equals to the product $g_J.J$ giving value $2.16\ \mu_B$ for a Ce^{3+} ion and $4\ \mu_B$ for a Yb^{3+} ion.

1.1.2. Magnetic interactions

Interatomic distances between neighboring rare earth ions are usually considerably larger than the distance for a direct overlap between *f*-electron orbitals. In addition the 4*f*-electrons are usually well screened by other electrons. Hence

magnetic ordering in Cerium and Ytterbium systems is mostly induced by indirect interactions.

The first type of indirect exchange interaction is superexchange visualized in Fig. 1.1a). That occurs mostly in semiconducting materials such as oxides and fluorides where magnetic ions are surrounded by atoms having affinity enough big to take unpaired electrons from them. These are then oriented in a way that satisfies Pauli Exclusion Principle with considering the orientation of electron spins on ligand orbitals.

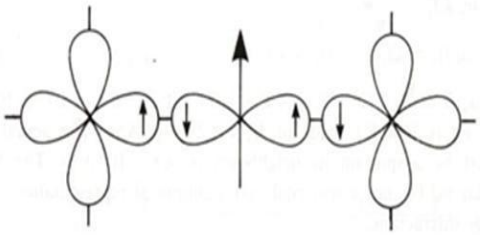

a)

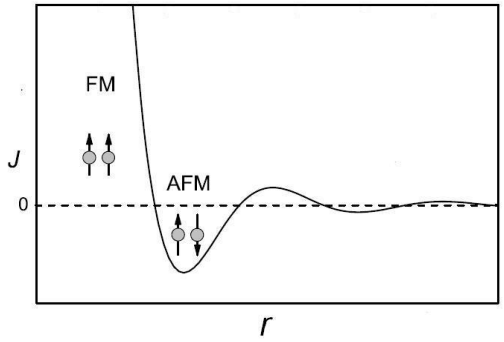

b)

Fig. 1.1: a) A schematics of superexchange interaction on the example of a transition metal oxide (the picture taken from(3)). The electrons from *d*-orbitals on the sides interact with the electrons from oxygen *p*-orbitals in the center. That results in antiferromagnetic coupling of magnetic moments on transition metal atoms. b) The dependence of RKKY interaction coupling constant *J* on the distance between neighboring ions.

Another mechanism, which has a big importance in Cerium and Ytterbium systems, is hybridization induced exchange interaction(4) arising from the mixing of partly localized *f*-states with band states (rare earth 5*d*-states and other elements *d*-states). This interaction is very anisotropic and crucially depends on the density of *d*-states close to the Fermi level. Higher density of states enhances the hybridization. This causes disturbing of crystal field effects and consequently smaller separations between crystal field levels in some Cerium compounds. Also the magnetic state can be qualitatively anticipated considering hybridization.

The last kind of indirect interaction is the Ruderman-Kittel-Kasuya-Yosida interaction (RKKY).(5,6) It can be found in systems where rare earth ions are in a metallic environment, because the interaction is mediated by conduction electrons. These electrons are polarized by magnetic ions and transfer the information from one

to another, as shown in Fig. 1.1b). One can write a Heisenberg Hamiltonian for this interaction:

$$H_{RKKY} = \sum_{i \neq j} J(r_i - r_j).J_i.J_j, J(r) = \frac{(r.\cos r - \sin r)}{r^4} \quad (2)$$

Conduction electrons are then polarized in a modulated fashion, which may give rise to a variety of possible magnetic orders from simple antiferromagnetic and ferromagnetic to complicated helical orders. Theoretical calculations confirm that in order to have quantitatively correct ordering temperatures, the RKKY interaction has to be included.(7)

1.1.3. Magnetocrystalline anisotropy

Magnetocrystalline anisotropy is a special case of magnetic anisotropy, where an energy distribution is connected with orientation of magnetic moments towards different directions. The energy difference arising by a rotation of magnetic moment from its preferred direction is called magnetocrystalline anisotropy energy (MAE). It is of electrostatic origin between two atoms,(8) which arises mainly due to spin-orbit interaction.(9) The total magnetic moment of one atom´s electrons is coupled to the local charge density of electrons, which interacts with crystal electric field created by surrounding ions. This gives a first order contribution to MAE. Another contribution to MAE arises due to direct magnetic dipole-dipole interaction, which is long ranged and thus depends also on the crystal dimensions and causes the shape anisotropy. Due to time reversal invariance, angular dependence of MAE for a particular symmetry can be expressed using an even power expansion of directional cosines of magnetization. Coefficients which belong to each term of the expansion are anisotropy constants. They are usually determined experimentally, but may also be obtained e.g. from band structure or density functional theory calculations(10,11) for zero temperature values. Anisotropic constants are strongly temperature-dependent. They also decrease in a vicinity of magnetic transitions. Some of them may become zero in case of ferromagnets, making the system isotropic.

.

1.2. Cerium and Ytterbium compounds

Among *f*-electron elements, Cerium (Ce^{58}) and Ytterbium (Yb^{70}) have very intriguing properties and therefore Ce- and Yb-based compounds are of the main interest in this thesis. Cerium has only one electron in its *f*-shell. Its electron shell configuration can be written as [Xe] $6s^2$ $5d^1$ $4f^1$.(12) The *f*-shell occupancy is often fragile to external conditions (magnetic field, temperature, pressure) or to chemical variation by for example element substitution in a compound. As a result, the only Cerium *f*-electron may be promoted into the conduction band, which makes Cerium non-magnetic. Thus for Cerium we usually observe two possible valence states 3+ and 4+. In the former, *d*- and *s*-electrons realize bonding (Ce^{3+}) and the *f*-electron is localized. In the latter one, all four electrons participate in bonding (Ce^{4+}) leaving Cerium´s *f*-shell empty. On the other hand Ytterbium has in a pure form and in most compounds filled its 4*f*-shell. This corresponds to the electronic configuration [Xe] $6s^2$ $4f^{14}$ and to valence 2+. In case that one *f*-electron becomes delocalized, the number of valence electrons increases to 3 (Yb^{3+}) and the *f*-shell contains one hole making Ytterbium magnetic. Both Cerium and Ytterbium carry stable magnetic moment in the 3+ case or if the valence is very close to it, because in this case the *f*-shell is partly filled and unpaired electrons are present. Sometimes both electronic configurations have non-zero probability and atoms are varying between them, what is then referred to as valence-fluctuating state. The average life time of each configuration is so small that most experiments do not distinguish them. The elements then appear to be in a non-integer valence state located somewhere between the two possible valence states. Compounds where different crystallographic sites are occupied by the same atoms, e.g. Yb, where each Yb-site has a different valency, are called mixed valent.(13)

The hybridization strength, which estimates the instability of the *f*-shell, can be expressed via the relation:

$$\Gamma = \pi V^2 n(E_F) \tag{3}$$

V is the matrix element for hybridization in the Anderson Hamiltonian and $n(E_F)$ is the density of states at the Fermi level. When we compare Γ with the binding energy needed for an electron to leave or enter the *f*-shell, three situations may occur. (1) The binding energy prevails; Cerium and Ytterbium have non-empty and non-filled

f-shells, respectively. One can observe a stable magnetic moment coming from the *f*-shell. (2) The two variables are comparable and the Kondo regime arises. This regime is characterized by formation of electron singlets built up by one *f*-electron and one conduction electron with opposite oriented spins. The Kondo singlet formation manifests in the physical properties by a logarithmic increase of the electrical resistivity and reduced sizes of the magnetic moments in the magnetically ordered and paramagnetic state. Moreover Pauli paramagnetic susceptibility and electronic coefficient of the specific heat are strongly enhanced at low temperatures, whereas Curie-Weiss behavior is restored at elevated temperatures. In general, the valence of Ce and Yb ions only slightly deviates from integer values. (3) The binding energy is smaller than the hybridization strength. In this case a significant mixing of localized and delocalized states occurs resulting in valence strongly deviating from integer values. Such systems are usually non-magnetic.

Ytterbium systems are often considered as the hole analogs to Cerium ones, although energy scales and the interplay between them, which determine magnetic state, have different response on external conditions. The Kondo temperature T_K, which is a measure of the strength of Kondo interaction,(14) should be strengthen by pressure due to increase of hybridization between *f*-electrons and conduction electrons when the volume is being reduced. But another parameter playing role is the elastic energy coming from variation of the ionic radius when valence changes. Pressurizing Cerium reduces the elastic energy due to a smaller ionic radius of non-magnetic Ce^{4+} ions. Thus the pressure stabilizes Ce^{4+} valence state. In contrary, the pressure usually stabilizes 3+ valence of Ytterbium since Yb^{3+} has a smaller volume. Another point of view is considering Doniach´s picture (Fig. 1.2),(15) where the magnetic state depends on the ratio between T_{RKKY}, a measure for the RKKY interaction, and T_K. RKKY interaction promotes magnetic ordering and hence goes against Kondo interaction, which favors a non-magnetic ground state by means of screening local moments by conduction electrons (Kondo single formation). The magnetic state then depends on which temperature prevails. Both characteristic temperatures can be scaled for Cerium systems by the coupling constant J proportional to the hybridization strength:

$$\Gamma = J.n(E_F) \quad (4)$$

While $T_{RKKY} \approx J^2 n(E_F)$, $T_K \approx \exp\left(-\frac{1}{2Jn(E_F)}\right)$. The consequence of these scaling relations is illustrated in Fig. 1.2.

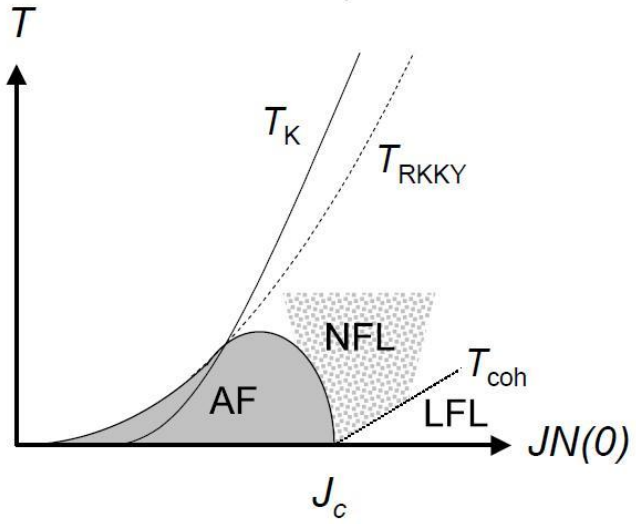

Fig. 1.2: Doniach´s phase diagram taken from Ref.(16) J_C marks the point (QCP) where magnetic order is suppressed to $T = 0$.

In Cerium compounds both T_K and T_{RKKY} increase with pressure, but T_K does it more steeply. The parameter J has a critical value J_C, where the magnetic ordering disappears at a quantum critical point (QCP) at zero temperature and a non-magnetic state is established. The term QCP refers to the fact that at zero temperature no thermal fluctuations are present, so the driving mechanism cannot be the same like in a classical order-disorder phase transition, and hence only quantum fluctuations can induce a transition from magnetic to non-magnetic state. These quantum fluctuations manifest in the physical properties resulting in a considerable deviation from the standard Landau Fermi liquid description.(17) Systems are then in non-Fermi liquid state (NFL). Upon raising J, the standard Landau-Fermi liquid state is being restored. On the left side from J_C in the diagram, we may often find Heavy fermion state, which is characterized by strong interactions between electrons forming quasiparticles. These have hugely enhanced effective masses (100 – 1000 times the bare electron mass). In some Heavy fermion systems, we can find superconductivity emerging around the QCP.(18,19)

For Cerium, an external pressure enhances the coupling constant J, to which f-level broadening and thus the hybridization are proportional. This strengthens valence fluctuations, which also augment T_K. On the other hand both T_{RKKY} and T_K in

Ytterbium compounds initially decrease at low pressures going through a broad minimum as can be seen in Fig. 1.3.(20) The coupling constant *J* here decreases too, and so valence fluctuations are suppressed by pressure supporting appearance of localized moments. Hence the system can be driven into magnetically ordered state in case that T_{RKKY} prevails over T_K (QCP_1^{Yb}). Then *J* again slowly raises and pressure pushes the system towards a second QCP (QCP_2^{Yb}), which is a transition from magnetically ordered state into a non-magnetic one again.

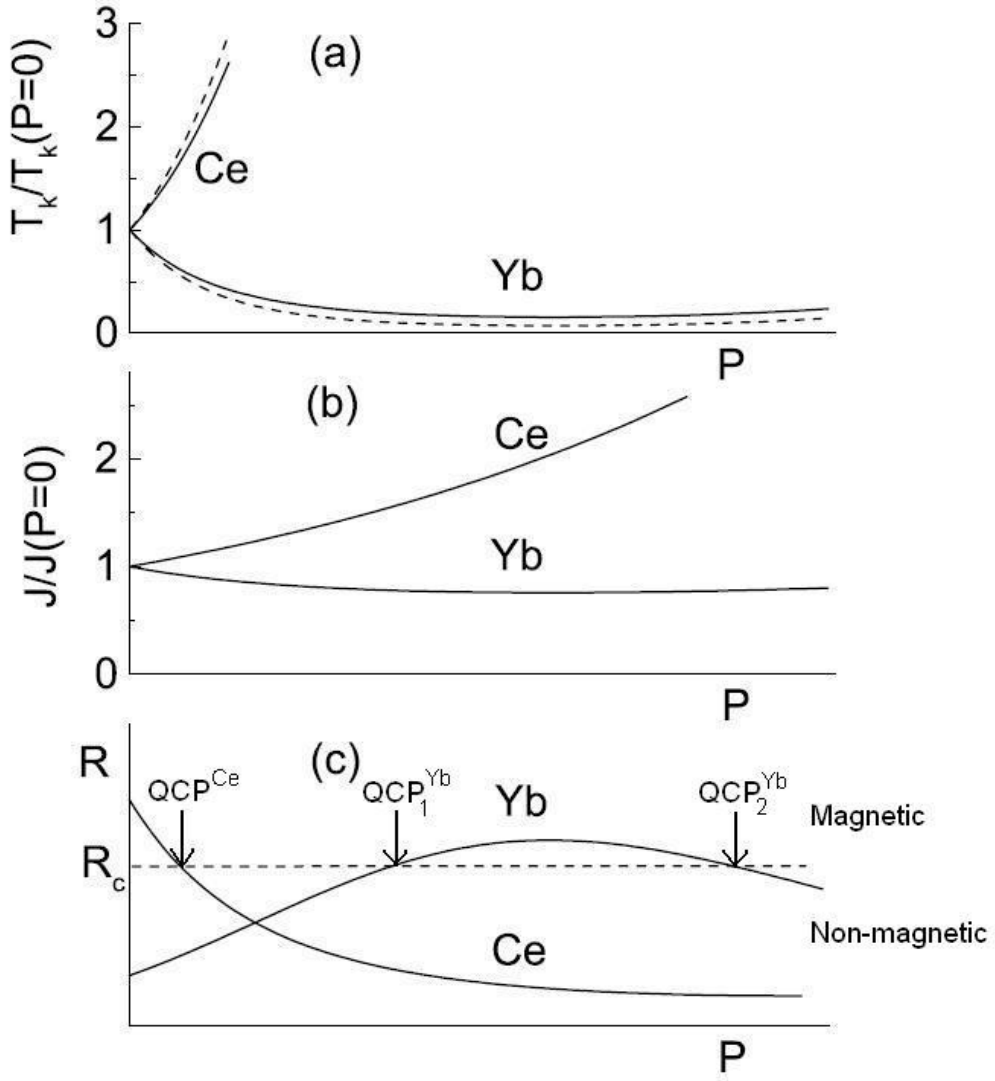

Fig. 1.3: Three variables as functions of pressure in Ce- and Yb-based systems as shown in Ref.(20) a) The Kondo temperature T_K. b) The coupling constant *J*. c) The ratio between T_{RKKY} and T_K . When the R_C is crossed from above, a QCP will take place and the system becomes non-magnetic. QCP^{Ce} marks the QCP for Cerium-based compounds, QCP_1^{Yb} and QCP_2^{Yb} denote the QCP for Yb-based ones.

1.3. Physical properties of magnetic materials

Now we will present a theoretical description of regular and exceptional phenomena, which may occur during measurements used in our study.

1.3.1. Magnetization and magnetic susceptibility

Magnetic moments in paramagnetic range are randomly oriented due to thermal fluctuations. When an external magnetic field is applied, they orient towards field direction, which results in an increase of the volume magnetization *M*. The magnetic susceptibility χ calculated from magnetization behaves with varying temperature according to a modified Curie-Weiss law:

$$\chi = \frac{M}{H} = \frac{\mathrm{N_A}\mu_0\mu_\mathrm{B}^2\mu_\mathrm{eff}^2}{3\mathrm{k_B}(T-\theta_\mathrm{p})} + \chi_0 \tag{5}$$

where θ_p is paramagnetic Curie temperature, which gives information about prevailing correlations in the paramagnetic state. χ_0 is a correction to Van Vleck temperature-independent paramagnetism and to averaged magnetocrystalline anisotropy in polycrystals.

1.3.2. Specific heat

There are various processes contributing to the specific heat of metals. A thermal energy given to matter is transformed into vibrations of individual atoms (phonons). In compounds which have lattice periodicity, the phonon contribution can be derived by merging the Debye description, assuming spectral dependence of phonons on frequency, and the Einstein description, where phonon energies are expected to be constant:

$$C_{phon} = 9\mathrm{k}_B\mathrm{N}_A(T/\theta_D)^3\int_0^{\frac{\theta_D}{T}}\frac{x^4e^x}{(e^x-1)^2}\mathrm{d}x + \mathrm{k}_B\mathrm{N}_A\sum_{i=1}^{6}\left(\frac{\theta_{E_i}}{T}\right)^2\frac{e^{\frac{\theta_{E_i}}{T}}}{\left(e^{\frac{\theta_{E_i}}{T}}-1\right)^2} \tag{6}$$

Here θ_D and θ_E are Debye and Einstein temperatures, respectively. The first term describes well acoustic phonons. For low temperatures ($T << \theta_\mathrm{D}$) this one goes to zero with temperature varying as T^3. On the other hand the second term is suitable

for description of optical phonons, which are more frequency-independent. At temperatures much higher than the Debye temperature, C_{phon} saturates to the 3R value per one mole of material (R is the gas constant).

In metallic materials there is always a contribution present, brought by electrons close to the Fermi level:

$$C_{el} = \frac{1}{3}\pi^2 n(E_F)\mathrm{k}_B{}^2 T = \gamma_{el} T \tag{7}$$

in this relation, $n(\mathrm{E_F})$ is the electronic density of states at the Fermi level.

Another contribution accompanies magnon excitations below the transition temperature in magnetic materials. If a magnetic transition is sensitive to external magnetic fields, so are the magnons, and hence the corresponding anomaly in the specific heat. An anomaly in the specific heat accompanies superconducting transition too. But here it is caused by a gap in the electron energy spectrum due to Cooper pairs formation.

In magnetic materials there is another contribution to specific heat coming from a gradual population of crystal field levels, which are split due to magnetic ion´s environment. This contribution is also called Schottky contribution and may be expressed in the following way:

$$C_{Schottky} = \frac{-\partial^2(\mathrm{k}_B T \ln Z)}{\partial T^2}, Z = \sum_i e^{-E_i/\mathrm{k}_B T} \tag{8}$$

Z is the partition sum determined from crystal field levels E_{i}.

From specific heat we can calculate entropy via the formula:

$$S(T^*) = \int_0^{T^*} \frac{C}{T}\mathrm{d}T \tag{9}$$

When the ground state of an R^{3+} ion is split by crystal field effects, its magnetic entropy can be expressed according to the relation:

$$S = \mathrm{R}\ln(2J+1) \tag{10}$$

1.3.3. Electrical resistivity

When one wants to estimate sample´s quality seriously, it is very suitable to measure electrical resistivity first. For most of materials there are a few contributions

to the electrical resistivity, which in the first approximation may be considered being independent of each other. According to the Mathiessen´s rule (Matthiessen, 1864):

$$\rho = \rho_0 + \rho_{\text{e–e}} + \rho_{\text{phonon}} + \rho_{\text{spd}} \tag{11}$$

The residual resistivity, ρ_0, arises due to lattice imperfections such as vacancies, impurity atoms, stacking and line faults etc. This contribution is usually treated as temperature independent and is the only part of electrical resistivity persisting down to lowest temperatures, unless the compound transforms into a superconducting state. Then the electrical resistivity falls to zero in all cases. Calculating the residual resistivity ratio (*RRR*) given by the ratio between electrical resistivity at high and lowest temperatures, where no other contribution than ρ_0 is expected, one can estimate the sample´s quality. The higher *RRR* is, the better quality of the measured material. In super clean materials, *RRR* can reach values of a few hundreds. Another contribution in (11) is $\rho_{\text{e-e}}$ caused by scattering of conduction electrons by other electrons. This term is proportional to the second power of temperature multiplied by a constant, which is proportional to the electron density at the Fermi level. The phonon part, ρ_{phonon}, comes from scattering of electrons on lattice vibrations and is usually proportional to the fifth power of temperature at low temperatures and becoming linear at higher temperatures. The last, usually considered, contribution in magnetic materials is ρ_{spd}. This contribution is temperature independent in the paramagnetic state and occurs due to electron scattering on randomly oriented magnetic moments. In ferromagnetically ordered state, ρ_{spd} is reduced, because for some electrons having suitable spin orientation it is easier to pass around the magnetic moments.

An additional contribution to electrical resistivity arises from crystal field levels E_{i} population,(21) which is temperature dependent. This contribution is analogous to the Schottky contribution to specific heat. It can be calculated by following expression:

$$\rho_{CF} = \rho_a \text{Tr}(PQ), P_{ij} = \frac{\exp(E_i / k_B T)}{\sum_{k=1}^{2J+1} \exp(E_k / k_B T)} \cdot \frac{(E_i - E_j) k_B T}{1 - \exp(-(E_i - E_j)/k_B T)},$$
$$Q_{ij} = \left|\langle i | J_z | j \rangle\right|^2 + \frac{1}{2}\left|\langle i | J_+ | j \rangle\right|^2 + \frac{1}{2}\left|\langle i | J_- | j \rangle\right|^2, J_\pm = J_x \pm i J_y \tag{12}$$

In antiferromagnets it may happen that resistivity increases in the ordered state. This occurs when additional boundaries for conduction electrons are created in the Brillouin zone due to a different the lattice periodicity.(22) Then one may introduce the truncation factor(23) g giving proportionality to the system net magnetization included in the term emerging in the denominator of eq. (11):

$$\rho = \frac{\rho_0 + \rho_{\text{e–e}} + \rho_{\text{phonon}} + \rho_{\text{spd}}}{1 - gm(T)} \tag{13}$$

An unusual contribution can be found in case of compounds exhibiting Kondo effect. Here the screening of magnetic impurity by conduction electrons enhances the electrical resistivity when temperature decreases. This increase is logarithmic, but in first approximation using a description(24) similar to standard Landau-Fermi liquid can be replaced by the following term:

$$\Delta\rho \propto 1 - (\alpha T / T_{\text{K}})^2 \tag{14}$$

1.3.4. Thermal expansion, magnetostriction

Important information about the state of matter is given by its lattice properties. Structural transitions, lattice distortions, rearrangement of atoms and their inter-atomic distances, all these are reflected in crystal dimensions. These can be determined by thermal expansion measurements. Ordinary materials expand with temperature due to anharmonicity in their phonon spectrum.

A book example is the structural transformation from γ→α in elementary Cerium,(25) which is accompanied by a tremendous collapse of volume. It is important to keep in mind that atoms of the same element with different valence states also differ in volume. Thus valence transitions are usually observed in thermal expansion measurements too.

Magnetostriction is a relative variation of lattice dimension coming from a change of the magnetic state.(26) It results from the balance between magnetic anisotropy and exchange interactions and elastic energy of the material.(27) Since magnetic properties are influenced by lattice anisotropy, magnetostriction is anisotropic too. Changes of lattice dimensions due to a temperature variation (e.g. entering a magnetically ordered state) are often termed as spontaneous magnetostriction. Another kind of magnetostriction is induced by magnetic field.

Unlike the case of ordinary metals with relative changes are of the order 10^{-5}, rare-earth compounds often exhibit giant magnetostriction being two orders of magnitude larger and reflecting a strong magnetoelastic coupling and magnetocrystalline anisotropy there. Magnetostriction as a function of magnetization decreases with temperature as $M^3(T)$ at low temperatures and as $M^2(T)$ when temperatures close to a magnetic ordering are reached.

2. Experimental methods

This chapter gives an overview of all experimental techniques used for obtaining our results, starting from sample preparation to evaluation of the measured data.

2.1. Preparation of single crystals

Single crystals are an indispensable source of information when it comes to investigation of physical properties of condensed matter. They provide information about anisotropy and have usually much better quality than polycrystalline samples, because they contain less lattice defects such as vacancies, atomic disorder, line and stacking faults and thermal strains, which all arise mainly due to much faster cooling after melting of polycrystals in mono-arc furnaces. There are certainly more methods for preparation of single crystals, but we will restrict our description to those used in our study.

2.1.1. Czochralski method

A standard technique for preparation of single crystals is Czochralski pulling method.(28) The principle is to slowly pull an ingot out of melt, which is kept liquid by arcs provided by electrodes placed around the crucible. A polycrystalline button, previously prepared in a monoarc furnace, serves as a source for the growing process. Both – the ingot and the crucible with melt have possibility to rotate. Rotation of both in opposite sense increases chance for a good material mixing during growth. The whole system is protected from oxidation by inert atmosphere (Ar of 6N purity; after previous vacuum of about 10^{-7} mbar). The Ar also serves as a medium for plasma stream between electrodes and the melt. The ingot diameter varies according to the current passing through the electrodes (responsible for heating the melt) and the pulling speed of the ingot. Ideally, one single crystal is being given preference to propagate when a narrow part is being made on the ingot (necking procedure). That is followed by slow increase of the diameter where only one single crystal should remain. The whole growing process lasts typically a few

hours. The method itself is suitable for congruently growing materials where the desired phase can crystallize instantly from the melt. In addition, all starting elements should have negligible evaporation. This method is self-cleaning, because for instance oxides have usually higher melting temperature. Thereby they are either pulled out at the beginning when the temperature is higher than the melting point of the prepared compound. Resulting ingot crystal size is limited by amount of the source button only.

2.1.2. Solvent growth method

Solvent growth method(29) is a very powerful tool in preparation of compounds growing incongruently or materials containing elements with high vapor pressures. The principle of this method is leaving crystals to grow inside a liquid element having lower melting point than the desired material. The solvent can either enter the prepared compound (self/true-flux method) or stay out of the compound (reacting flux). It usually does not only reduce the melting point of the prepared compound and starting elements, but it also protects the elements from oxidation and improves temperature homogeneity and stability during the growth. The elements have to be placed into an inert crucible – made of e.g. alumina, zirconia or boron nitride – and sealed under high vacuum or protective atmosphere inside for instance a quartz glass ampoule or a tantalum crucible. A special attention should be put to good polishing of the surface of oxidizing elements, because oxides will stay in the melt, where they may serve as crystallizing centers. The whole setup has to be heated up to temperature where all the elements melt. Then the temperature is slowly cooled down. During this cooling down or the growth phase, single crystals should form inside the solvent. At the end the single crystals are separated from the solvent by centrifuging. This is the only moment within the whole growth process when the crystals experience a significant temperature gradient. Single crystals usually have surface facets that make their orientation much easier. A typical yield from one growth process is displayed in Fig. 2.1. We often simply recognize twinned crystals by observing their shape. One disadvantage of solvent growth method is that there are too many free parameters like temperature range, cooling rate, the choice of a proper solvent and starting stoichiometry of the elements. In particular this last

point makes the situation quite complicated, since there are usually three or four starting elements while an appropriate temperature range can be only roughly estimated. Usually it is a matter of experience. Binary and ternary phase diagrams give the first starting point, but they are no longer valid in case of ternary compounds grown from true or reacting flux. Here ternary or quaternary phase diagrams would be needed, respectively. Another disadvantage of the solvent growth method is that solvents often remain on the surface of single crystals and have to be removed by acids. A bigger problem is when the solvent is present inside single crystals as inclusions. In this case, a different solvent has to be taken.

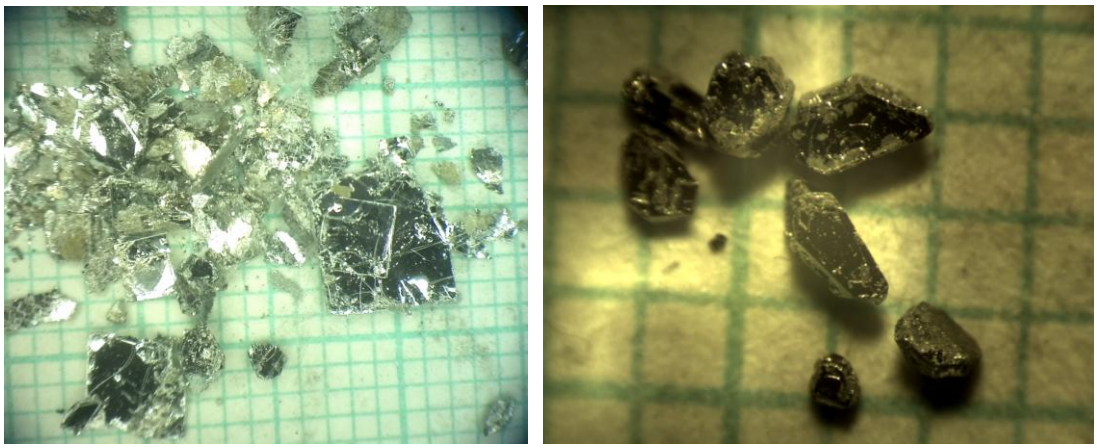

Fig. 2.1: Left panel - a content of one alumina crucible after decanting solvent. Majority of mass belongs to an unwanted binary compound.
Right panel – selected single crystals having the desired composition $YbPt_2Si_2$.

2.2. Characterization of single crystals

2.2.1. Laue backscattering X-ray diffraction

In order to confirm whether we have a single crystal or not, the most straightforward technique is X-ray Laue diffraction.(30) Due to much smaller penetration depth than in case of neutrons, backscattering technique is generally used for this purpose. The X-ray beam hits the surface of the material under investigation and is scattered back towards an image plate. A diffraction pattern without concentric circles and well defined diffraction spots is a clear sign of a good single crystal. In Laue diffraction a broad range of wavelengths is mandatory to have enough

reflections, in order to determine the correct crystal orientation. An alternative way to orient a single crystal is to use the standard Bragg-Brentano geometry with a single wavelength, which is described below.

2.2.2. X-ray powder diffraction

One way to examine material´s crystal structure is via measuring X-ray powder diffraction with the conventional Bragg-Brentano *θ-2θ* geometry.(31) Crystallographic planes create *n*-th maximum of intensity to diffraction angle θ according to Bragg´s formula:

$$2d_{hkl}.\sin\theta = n.\lambda \quad (1)$$

where λ is the wavelength of the incoming radiation, d_{hkl} denotes distance between planes with the respective *hkl* Miller indexes. Here a reasonable part of reciprocal space is scanned in order to get enough diffraction peaks. From this one obtains lattice parameters, atomic positions in the unit cell, information about preferential orientation of the powder, atomic displacement factors etc. But the information is collected solely from crystallites oriented parallel to the surface. Thus the powder should contain many randomly oriented grains in order to have good statistics.

In our lab we employed a Bruker D8 Advance diffractometer. It has a source of Cu $K\alpha_{1,2}$ radiation providing initial beam wavelength $\lambda(K\alpha_1)$ = 1.54056 Å and $\lambda(K\alpha_2)$ = 1.54439 Å. Diffraction patterns were typically collected between 10 and 80 degrees in steps of 0.05 deg and an acquisition time of few seconds per step. The patterns were evaluated using Rietveld method.(32,33) The FullProf program(34) treats the whole diffraction pattern at one time considering its profile according to the crystal structure and experimental conditions. Quality of the fit is judged by the refinement factor *R*:

$$R = \sum_j w_j (I_{jo} - I_{jc})^2 \quad (2)$$

I_j is the intensity at diffraction point *j*. Indexes o and c denote observed and calculated intensities, respectively, whose difference is weighted by w_j according to the peak size of the related crystal reflection.

2.2.3. Single crystal X-ray diffraction

The crystal structure of CeRuSn (see Chapter 4) below room temperature was investigated by means of single crystal X-ray diffraction. A single crystal was mounted into a Lindemann capillary. Due to transmission geometry of the method, crystal´s dimensions were restricted to less than 0.1 mm in all directions. The capillary was inserted into a Bruker Apex II diffractometer and irradiated by Mo *K*α radiation with wavelength 0.71073 Å. Low temperatures were achieved by a continuous flow of cold nitrogen gas. The crystal structure was resolved by direct methods and final refinement was done by full matrix least squares based on F^2.(35) The CeRuSn structure was resolved by fitting of ≈ 1600 reflections at room temperature and ≈ 3600 at 120 and 200 K, from which the fit described more than 96 % (297 K) and 99.5 % (120, 200 K), respectively.

2.2.4. Energy dispersive X-ray analysis (EDX, EDAX)

A possibility to probe the material´s composition is via energy dispersive X-ray analysis.(36) The method exploits the fact that each element has a characteristic spectrum of X-ray radiation, which is emitted after atoms were irradiated and its electrons excited by absorption of incoming high-energy electrons. Energy spectrum then contains maxima at energies characteristic for each element in the material together with some background, which arises due to Bremsstrahlung originating from the interaction between incoming electrons and the matter. After integrating peaks in energy for each element and comparing their areas, one obtains the sample stoichiometry within the accuracy of a few percent.

EDX measurements were performed by a scanning electron microscope Tescan Mira I LMH equipped by a Bruker AXS energy dispersive detector, which served for analysis of the energy spectra and demarcation of areas for each phase occurring in samples. The spectra were cleared of background contribution and fitted by software supplied by Bruker Company together with the diffractometer. The incident electron beam had energy ranging from 0 to 15 keV.

2.3. Measurements of thermodynamic and transport properties

The most important part of this thesis consists of measurements, by which we studied the electron properties of the selected compounds. Most of the experiments were performed utilizing the Physical Property Measurement System (PPMS) instruments from the company the Quantum Design. The equipment allows reaching temperatures between 1.7 and 1000 K and to apply magnetic fields up to 14 T in one direction. With additional ^{3}He inserts, the temperature range was extended down to 0.4 K for electrical resistivity and specific heat measurements. The magnetization was in a few cases measured by Quantum design´s Magnetic Property Measurement System (MPMS) with implemented Superconducting Quantum Interference Device (SQUID). Temperatures between 1.8 and 400 K were available together with magnetic fields up to 7 T. Some of the measurements of the electrical resistivity were realized using a closed-cycle refrigerator (CC). Here the available temperature range was 4 - 325 K.

2.3.1. Magnetization measurements

Magnetization as a function of magnetic field or temperature was mostly measured employing the PPMS using the Vibrating Sample Magnetometer (VSM) option. Samples (mass ≈ 5 - 40 mg) were glued to a plastic holder by GE7031 varnish, see Fig. 2.2. For temperatures above 400 K, we have used an oven extension for VSM. Samples were glued by Zircar cement provided by Quantum design Co. and wrapped into a Cu-foil. The foil served as a thermal connection between the sample and heaters on the holder. Between 10 and 400 K, we mostly used temperature ramps 1 K/min and above 400 K it was 4 K/min. Below 10 K the speed was lower, usually 0.2 and 0.1 K/min.

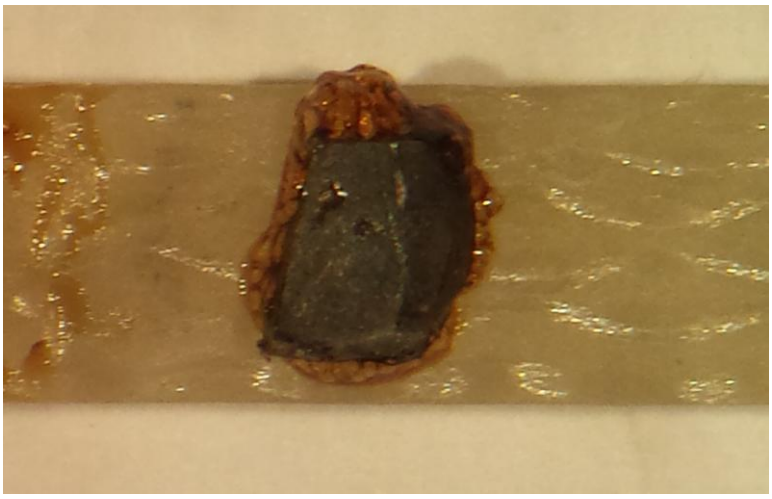

Fig. 2.2: A VSM holder with a glued single crystal of CeRuSn.

In a few cases we also used MPMS magnetometer to measure temperature and field dependences of the magnetization. The samples were stacked between plastic straws and additionally stack by a small amount of GE7031 varnish. The same temperature range was available here (1.8 - 400 K), but magnetic fields were limited to 7 T.

2.3.2. Specific heat

Heat capacity was determined by relaxation method, during which heat pulses were sent to the sample platform in order to heat it up by 2 % of the actual temperature. Thermal relaxation in vacuum towards initial temperature was realized through wires connecting the measurements puck with the platform where the sample was placed on. Time dependences of the platform´s temperature were fitted by a formula,(37) from which the heat capacity was calculated. Experimental error came mostly from deviation of the fitting curves from the measured ones. Additional errors arose due to the sample mass, addenda values and by estimating the amount of Apiezon. Samples should be well coupled to the platform, otherwise a huge enhancement in measurement´s uncertainty may occur.

For thermal connection of the sample with the platform, we used cryogenic vacuum grease Apiezon N. A view on a heat capacity puck for PPMS instruments with a sample attached to it is shown in Fig. 2.3. Samples had masses ranging from

2 to 12 mg. Sample´s specific heat itself was computed after subtraction of contributions from the glue and the puck (platform and connectors) provided by a previously measured bigger amount of Apiezon and the available puck´s addenda, respectively.

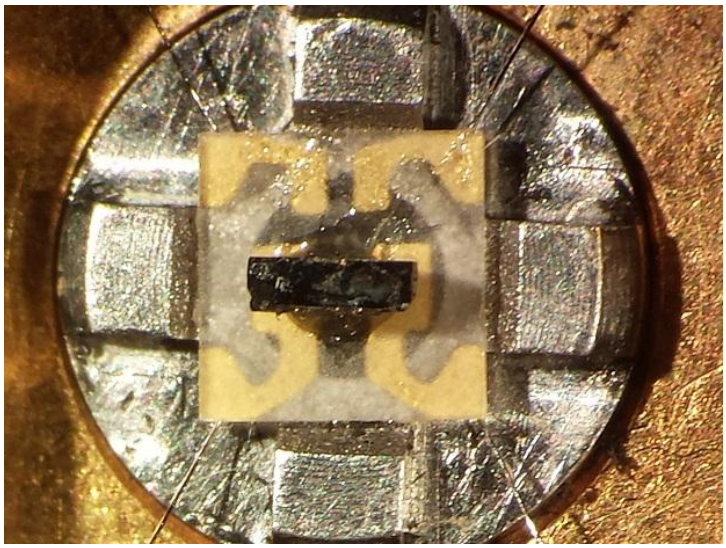

Fig. 2.3: A single crystal sample of $YbPt_2Si_2$ stuck to the platform of a He_3 heat capacity puck for measurements in PPMS instruments. The sample platform is connected to the puck via four wires.

2.3.3. Electrical resistivity

Electrical resistivity measurements were carried out by ACT current method, during which an alternating current went through the sample. This method eliminates possible charging of sample´s opposite parts. The frequencies we used ranged from 83 Hz up to 233 Hz. The precision of this method depends on the quality of fitting sinusoidal signal. In case of poor electrical contacts the impedance is dramatically modified. The signal becomes noisy and electrical resistivity values may differ significantly from real values. This causes a distortion of the sinus-wave signal. As a result, data points are usually scattered. With respect to absolute values, we have to add an uncertainty in measuring of the sample cross section and the voltage contacts separation.

Electrical contacts made of Cu- (50 μm in diameter) or Au-wires (25 μm in diameter) were attached to samples by silver paste or spot-welded, respectively (see

Fig. 2.4). They were placed in the way to satisfy the fourth-probe geometry, which allows neglecting resistivity of the contacts and the incoming wires. Samples were glued by GE varnish to the measuring pucks. A cigarette paper served as an insulating layer between the sample and the ACT puck. At temperatures above 10 K, 1 mA current was applied. Current lower than 0.5 mA was used in order to eliminate possible sample heating below 10 K. Between 350 and 10 K, the samples were being heated and cooled mostly by the rate of 1 or 2 K/min. Below 10 K, the speed in PPMS instruments was reduced to 0.2 K/min or less.

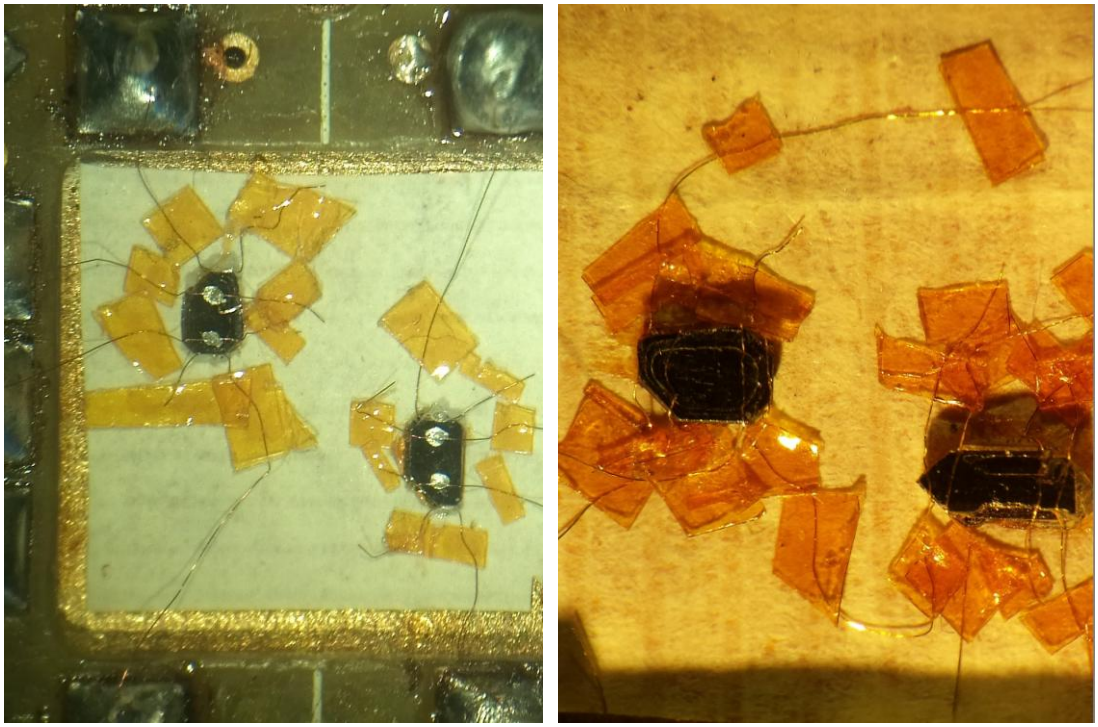

Fig. 2.4: Single crystals of $YbPt_2Si_2$ placed on ACT pucks and contacted for electrical resistivity measurements. On the left panel, contacts were attached by silver paste, whereas spot-welded contacts are shown in the right panel. The wires were additionally fixed by pieces of Kapton tape applicable at cryogenic temperatures.

2.3.4. Thermal expansion

In order to investigate changes of lattice, we measured thermal expansion in a miniature capacitance cell.(38) The capacitor plates were insulated via sapphire washes, which also allowed placing the samples without any glue.(39) Samples of typical height 0.5 - 2 mm were polished in order to have two parallel planes perpendicular to the measured direction. The capacity was being read out by an Andeen Hagerling 2500A capacitance bridge. From this information, the variation of sample dimension with temperature and magnetic field was calculated by a program using formulas from Ref.(38) The capacitor plate's separation was given by the inverse value of capacity multiplied by a complex formula containing parameters describing different parts of the cell and their variation with temperature. Temperature and magnetic field during our experiments were being controlled by PPMS instruments.

2.3.5. Differential thermal analysis

Differential thermal analysis(40,41) (DTA) is a widely used experimental measurement technique that is mainly applied on metals and alloys because these are good conductors of heat. A DTA instrument consists of a furnace and two crucibles with thermocouples (see Fig. 2.5). One crucible is for the sample being measured and the other, which is empty, is used as a reference. The voltage difference between both thermocouples is measured during heating and cooling cycles. The measurements are sensitive to the difference between the enthalpy vs. temperature relation of a sample and the enthalpy vs. temperature of a standard. Enthalpy vs. temperature relations of pure metals are well known and this information is primarily used for calibration. The results presented in this work were obtained by a Setaram instrument. Samples (mass ≈ 100 mg) were measured in Helium atmosphere.

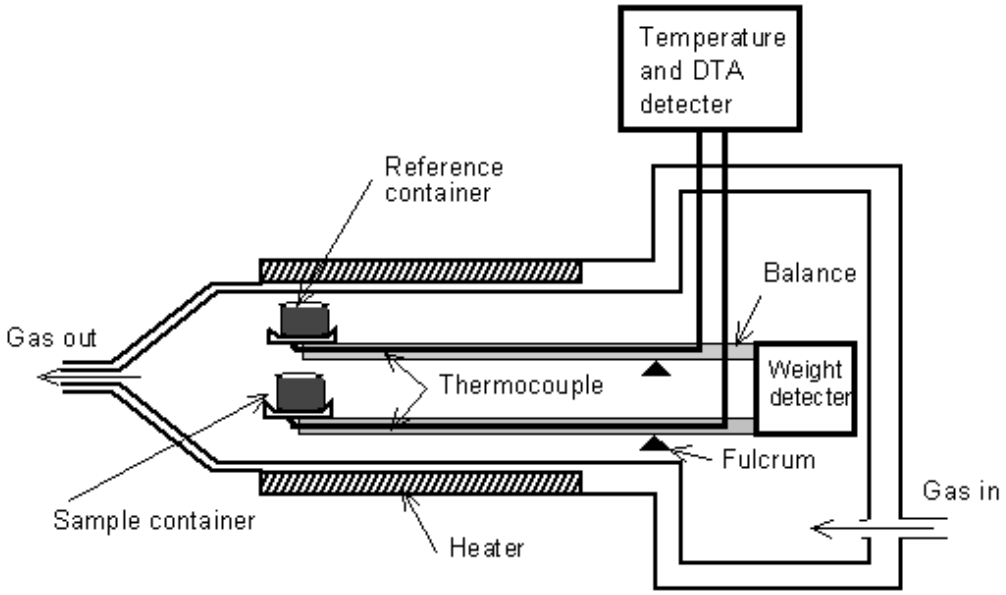

Fig. 2.5: A schematics of DTA measurement set up from Ref.(42)

2.4. High-pressure measurements

2.4.1. Electrical resistivity

For measurements of electrical resistivity under high pressure, we used a double-layered (CeBe/NiCrAl) piston cylindrical cells (Fig. 2.6), which allow application of hydrostatic pressure up to 3 GPa. The pressure slightly deteriorates with temperature by approximately 0.2 GPa when cooled from 300 K down to 2 K. To correct for this, from each applied pressure (pressure determined at room temperature) a value of 0.2 GPa was subtracted in the low-T data.

Fig. 2.6: A pressure cell designed for not only electrical resistivity measurements. From the left to the right: a reduction for connection with PPMS instruments, a plug support, a plug, the body of the cell, a piston, a piston support, and a pushing rod used during changing pressure inside the cell.

Samples contacted in four-probe geometry were glued on a cigarette paper by a GE varnish. The paper was glued on the wires passing through the plug and the Stycast epoxy sealing. All this, together with a manganin manometer, was inserted into a Teflon cap loaded by Daphne oil 7373,(43) which served as pressure medium. The pressure inside the cell was determined by measuring electrical resistivity of manganin manometers, see Fig. 2.7. Temperature scans above 10 K were measured with heating and cooling rates 0.5 K/min in order to eliminate effects (thermal gradients in the cell) coming from cell´s bigger heat capacity. Below 10 K, the rate was reduced to 0.2 K/min. All these measurements were performed in PPMS instruments. Sample dimensions were limited by the diameter (2 mm) and available length (1 cm) inside the Teflon cap.

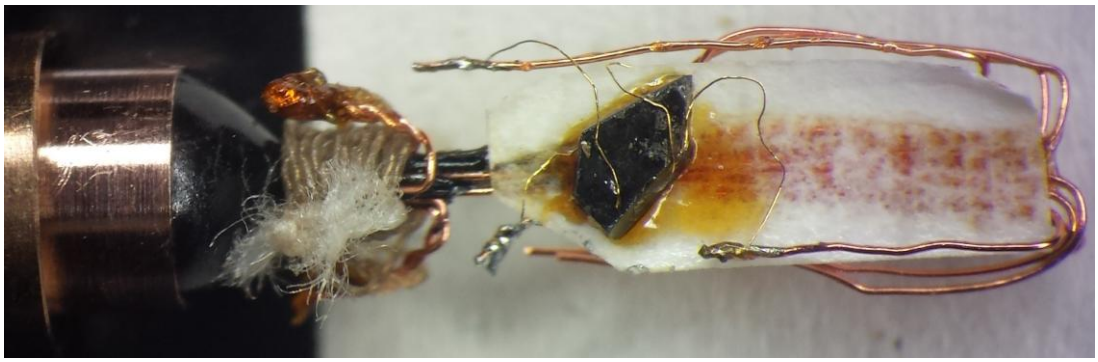

Fig. 2.7: A CeRuSn single crystal contacted for electrical resistivity measurements under high pressure. Next to it on the left, there is a manganin manometer twisted around Stycast epoxy sealing.

2.4.2. Magnetization under high pressure

A sample for magnetization measurements at low temperatures was pressurized in a clamp pressure cylindrical cell, which could reach pressures up to 1 GPa. The sample was glued with GE varnish to a copper holder, which was connected with the body of the cell as can be seen in Fig 3.8. Daphne oil 7373 was used as pressure medium. The pressure was determined by measuring the superconducting transition temperature of a piece of lead inserted into the pressure cell together with the holder by means of AC susceptibility.

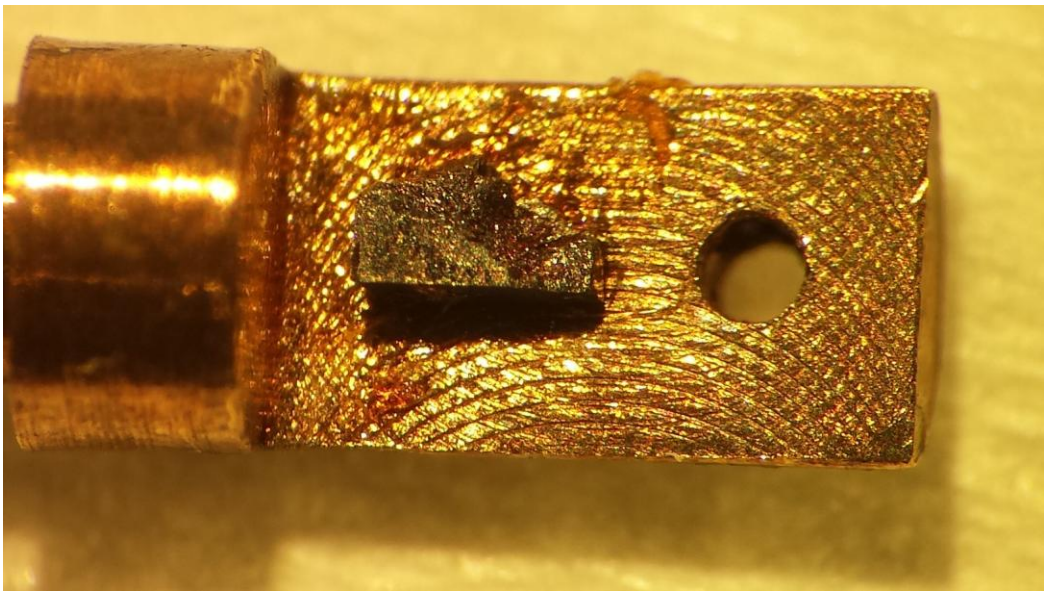

Fig. 2.8: A copper holder for magnetization measurements under high pressure. A piece of CeRuSn single crystal is glued onto it by GE varnish.

3. CeRuSn

3.1. Introduction

Cerium intermetallic compounds show a rich variety of fascinating phenomena, like unconventional forms of superconductivity, non-Fermi liquid behavior, quantum criticality and non-integer valence of Cerium atoms. But even among them there is a really unique one and that is CeRuSn. The compound crystallizes in a completely novel structure derived from the CeCoAl-type one.(44) That means it exhibits monoclinic symmetry, but in more striking the CeRuSn unit cell can be approximated by doubling the CeCoAl one along the *c*-axis. This doubling is due to slightly different interatomic distances. As can be seen in the left panel of Fig. 3.1, the originally Ce-*T* (*T* = transition metal) distances 2.61 and 2.67 Å in CeCoAl are modified in CeRuSn in such way that for one Cerium site (Ce1) the distance between Ce-Ru atoms is much shorter than its pendant in CeCoAl, yielding 2.33 and 2.46 Å. These are even less than the sum of Cerium and Ruthenium covalent radii 2.89 Å. On the other hand the second Cerium site (Ce2) has these distances larger being 2.91 and 2.88 Å. Reduced size of the effective moment in the paramagnetic range, which reaches only one half of expected for Ce^{3+} state, motivated S. F. Matar et al. to perform electronic structure calculations.(45) From these it was suggested that Ce1 accommodates intermediate-valent Cerium atoms, whereas Ce2 positions are occupied by Ce^{3+} atoms. These findings were later supported by X-ray near edge structure study(46) revealing that the average valence for Ce1 and Ce2 site is 3.18.

The situation becomes even more interesting when CeRuSn is cooled below room temperature (RT). First results on polycrystalline samples showed a distinct 1^{st} order type of anomaly at 187(2) K and 283(2) K during cooling and heating cycles, respectively. It was suggested this first order phase transition is due to a change in valency(44) or, more speculatively, might be a manifestation of the formation of a charge density wave.(47) The first possibility was expected from magnetic susceptibility measurements on polycrystalline samples where a huge hysteresis was found between cooling and heating cycles. The second was concluded from an increase of resistivity accompanying the transition and from its large temperature

hysteresis. First X-ray Absorption Near Edge Structure (XANES) measurements of CeRuSn(46) excluded a valence change due to the transition, whereas a recent revising study by the same group on freshly cleaved single crystals confirmed this possibility.(48) Accordingly the valence is reduced from 3.18 at 320 K to 3.15 at 100 K. The transition involves a transformation in the stacking sequence of the Cerium layers, as discussed later, and is accompanied by a shrinkage of the *c*-axis by 0.89 %.(46) Below 100 K CeRuSn was reported to be in an ill-defined modulated state close to the tripling of the CeCoAl-like structure. A powder neutron study(49) on a polycrystalline sample confirmed findings from the X-ray study(46) about the crystal structure modulations. But the sample was found to be multi-phase below 100 K preventing a meaningful analysis of the low temperature structure. This was apparently caused by its poor quality, which was further deteriorated by pulverizing for the powder measurements.

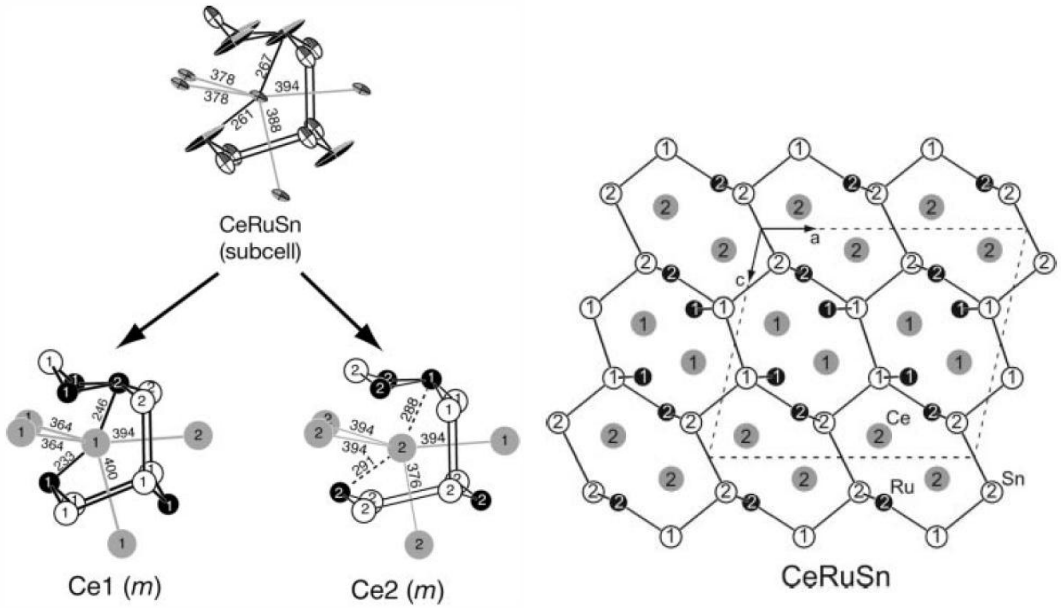

Fig. 3.1: Figures taken from ref. (44)

Left panel - Cerium coordination shell in CeCoAl (the upper one) and for two Cerium sites in CeRuSn. Grey dots represent Cerium atoms, black dots transition metal atoms and empty circles are Aluminum and Tin.

Right panel – The crystal structure of CeRuSn viewed from the *b*-axis direction at room temperature.

3.2. Sample preparation

Single crystals were prepared by the Czochralski method in a tri-arc furnace. A polycrystalline source button was arc-melted from a non-stoichiometric ratio of high purity elements (Cerium pieces 99.9% additionally purified by solid state electrotransport technique(50), Ruthenium powder 99.95%, Tin pieces 99.999% all provided by Alpha Aesar Co.). Several batches were prepared aiming to improve the sample´s quality. Due to appearance of little amount of Ce_5Sn_4 spurious phase, the Ruthenium content in later batches (from #11 on) was increased when making polycrystalline buttons. However, most of the low-T measurements were performed on single crystals from batches #2 and #4. Details about the used initial weights etc. are given in Appendix A.

During the growths currents on the electrodes (7 - 11 A) were being slowly varied in order to change the ingot diameter. The pulling speed was mostly kept smaller (2 mm/h) while making a neck on the ingot (≈ 1 mm in diameter) and then increased to 5 mm/h when the maximum diameter (≈ 5 mm) had been reached. A typical ingot is shown in Fig. 3.2. The ingots are rather brittle and were broken revealing boundaries between different grains. Ingots mostly split into two parts with smooth and shiny planes oriented perpendicularly to the reciprocal *a*-axis (square-like areas ≈ 5 - 20 mm^2, going through the whole ingot in the pulling direction). Alternatively, the material broke up by planes perpendicular to the reciprocal *c*-axis (≈ 3 - 8 mm^2, tilted by 45º from the ingot´s axis). Orientation of the planes was found and refined by psi-scans. Finally, we obtained single crystals by cutting the pieces by a wire saw and polishing the cut pieces by grinding wheels. The orientation was checked again afterwards. The prepared single crystals were annealed for one week in vacuum ($p = 10^{-6}$ mbar) at 700º C. Their overview is listed in Table 3.1. Parts of some pulled ingots were pulverized and inspected by powder X-ray diffraction. From the refinement of a powder X-ray diffraction pattern (Fig. 3.3) on a part of an as cast ingot from batch #5 we obtained lattice parameters yielding a = 11.555(3) Å, b = 4.752(1) Å, c = 10.211(2) Å and β = 102.96(2)º. These are in a very good agreement with the polycrystalline and single crystal data from literature.(44,46,48) Most of the main reflections are well described within the model of two times doubled unit cell of the CeCoAl-type. The disagreement of the fitted

and the observed intensity at 36º ((001) reflection)) occurs mainly due to a preferential orientation of the grains. A small amount (1.5 %) of foreign phase Ce_5Sn_4 was traced up in the pattern and is further discussed in Appendix A. We also found roughly 8 % of elemental Ruthenium, which may have been residing on the surface of the ingot, since it was not observed by EDX measurements (Fig. 3.4). Some amount of isolated Ruthenium inclusions was also found in the bottom part of the polycrystalline source button used for pulling by the Czochralski method. This would explain the presence of the Ce_5Sn_4-phase, which may have arisen due to the lack of Ruthenium atoms in the melt during the growth procedure.

Table 3.1: An overview of CeRuSn single crystals prepared by the Czochralski method.

Batch No.	Starting stoich.	Pulling rate	Result	SC label	*m*(mg)	dim (mm)	RRR (*a*,*b*,*c*)
1	$Ce:Ru:Sn_{1.06}$	8 mm/h	PC	none			
2	Ce:Ru:Sn	2 mm/h	SCs	#209	5.4	0.8x2.5x1	16,12,10
3	Ce:Ru:Sn	2/3 mm/h	fail	none			
4	Ce:Ru:Sn	2/3 mm/h	SCs	#401	2.8	0.6x1.8x0.9	11,12,7
5	Ce:Ru:Sn	2 mm/h	fail	none			
6	Ce:Ru:Sn	2/5 mm/h	grainy	none			
7	Ce:Ru:Sn	2/3 mm/h	SCs	#701	25	0.5x3x15	x,8,x
8	Ce:Ru:Sn	3 mm/h	grainy	none			
9	Ce:Ru:Sn	2/3 mm/h	SCs	#901	22.3		15,12,9
				#901A1	2.88	0.4x0.9x0.3	
10	Ce:Ru:Sn	2 mm/h	SCs	#101	10		12,9,7
11	$Ce:Ru_{1.1}:Sn$	3 mm/h	SCs	#111	17		
12	$Ce:Ru_{1.15}:Sn$	3 mm/h	SCs	#121	25	0.7x1.3x2	
13	$Ce:Ru_{1.2}:Sn$	2 mm/h	SCs	#131	149	3x5x3	
				#132	103	2x5x3	

In addition small pieces of annealed and as-cast single crystals were studied by X-ray single crystal diffraction from RT down to 180 K. The results will be presented in the Section 4.3.4.

Fig. 3.2: An ingot obtained from the growth #10 by Czochralski method. On the left end there is a tungsten holder serving as the starting seed. During this preparation two necking parts were made.

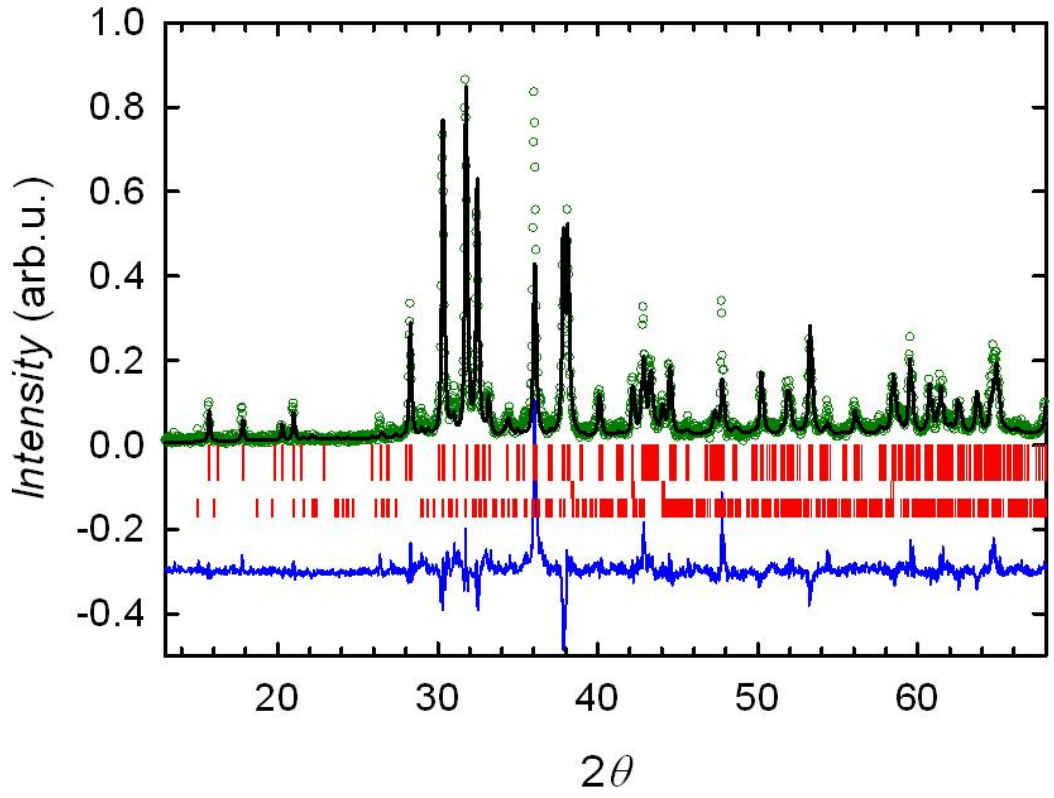

Fig. 3.3: A Rietveld refinement of a powder X-ray pattern taken on a crushed part of the ingot from batch #5. Measured data are represented by the green circles, the fitted intensity by the black curve and their difference by the blue curve. The red dashes signify Bragg´s positions (the first two rows – CeRuSn, the 3rd row – Ce_5Sn_4, the 4th – Ru).

In Fig. 3.4, a view made by electron microscope on a polished surface of a sample from batch #9 and is shown. The biggest fraction of the area belongs to the CeRuSn phase. Brighter areas represent Ce_5Sn_4 phase. We can see that the foreign phase takes only a few percent of the overall surface. Main phase has the expected stoichiometry in the range of method´s precision, see Table 3.2. Darker areas have the same stoichiometry as the main phase. The contrast may be caused by slight oxidation of the sample´s surface prior to the measurement.

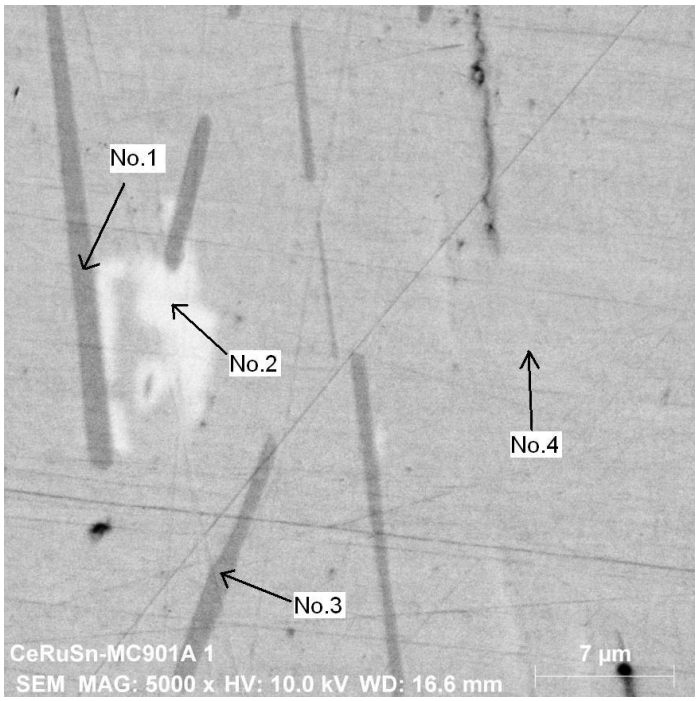

Fig. 3.4: A view on the surface of a sample from batch #9 grown from stoichiometric amount of pure elements. EDX spectra were collected at points marked by the arrows.

Table 3.2: The atomic fractions determined from EDX spectra measured at points marked in Fig. 3.4.

point No.	At. fraction Ce (%)	At. fraction Ru (%)	At. fraction Sn (%)
1	33(1)	35(1)	32(1)
2	43(2)	15(1)	42(1)
3	33(2)	35(1)	32(1)
4	33(2)	35(1)	32(1)

DTA was used to obtain information about behavior of the compound during heating up to high temperatures. Before we started the measurements of magnetic properties mentioned before, the thermal annealing had been made to improve homogeneity of our samples. During DTA measurements, two thermal cycles were applied on the studied sample. The heating/cooling rate was 10 K/min and maximum thermal cycle temperature was 1450 K. The results obtained in the second thermal cycle are shown in Fig. 3.5. The first thermal cycle data are not included for a simple reason; various thermal strains and meta-stable states (high temperature gradients appear in samples during fast cooling in monoarc furnaces) can exist in the sample after its preparation. All these effects were removed in the first thermal cycle. The temperature dependence of the heat flow presented in Fig. 3.5 had to consequence that the CeRuSn polycrystalline sample had only one phase with the melting point 1300(5) K. This value was determined from the onset of the transformation peak during heating. It can be seen that the melting as well as crystallization take place without hysteresis. Both transformation temperatures were practically the same. According to this, a suitable temperature for annealing being 700º was determined and all single crystals in our study were thermally treated for one week at this temperature in high vacuum (≈ 10^{-6} mbar).

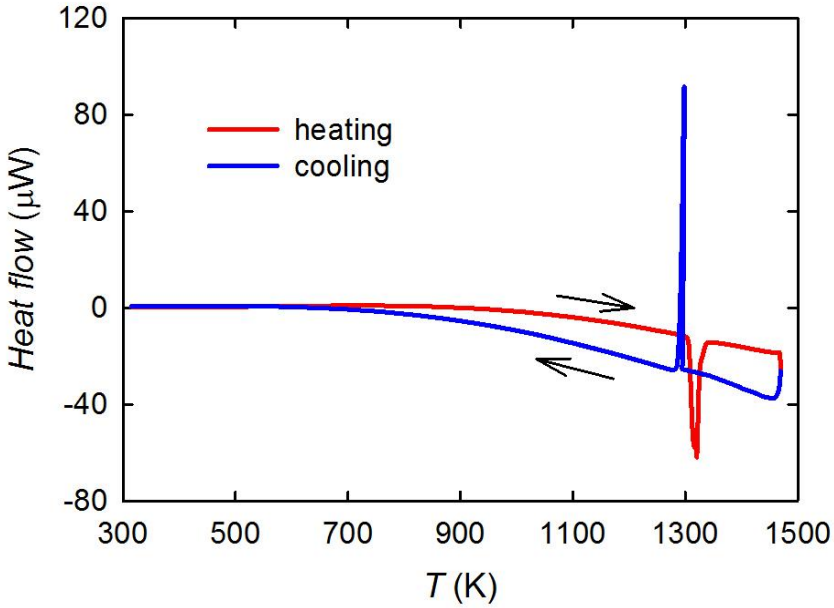

Fig. 3.5: Temperature dependence of the heat flow for a polycrystalline CeRuSn sample.

3.3. Physical properties at high temperatures

Due to expected connection between structure and physical properties, all our experiments were carried out on single crystals, except our first testing measurements of electrical resistivity on polycrystalline samples. In this chapter, our data provide a picture about physical properties at high temperatures, where structural transitions can be found. These data were mostly collected on crystals from batches #2 and #4. These carefully shaped and oriented samples showed to be of good quality and hence were subjected to most of the available experimental techniques, including high field magnetization measurements in pulsed fields and Laue neutron diffraction. The later one proved single grain nature of the sample from batch #4.

3.3.1. Electrical resistivity

In Fig. 3.6, the electrical resistivity measured along main crystallographic axes is depicted. Two anomalies were observed during cooling cycles. The first one at 290 K (T^{C}_{U}) is characterized by a step-like increase of the resistivity by some 7 %, whereas the second one at 226 K (T^{C}_{L}) expresses itself in the opposite way, although it seems smoother. Warming up the samples revealed that both transitions have the same shape but take place at much higher temperatures, namely at 256 (T^{W}_{L}) and 307 K (T^{W}_{U}), giving rise to a significant thermal hysteresis of ~ 40 K and ~ 20 K, respectively. This suggests that the anomalies are of first order nature, which is usually observed in case of structural transitions (ST). The transitions are intact even in magnetic field of 14 T. This is documented in Fig. 3.7 where the electrical resistivity of a sample from batch #2 is shown. We can see that positions and shape of the ST are the same in zero and 14 T field.

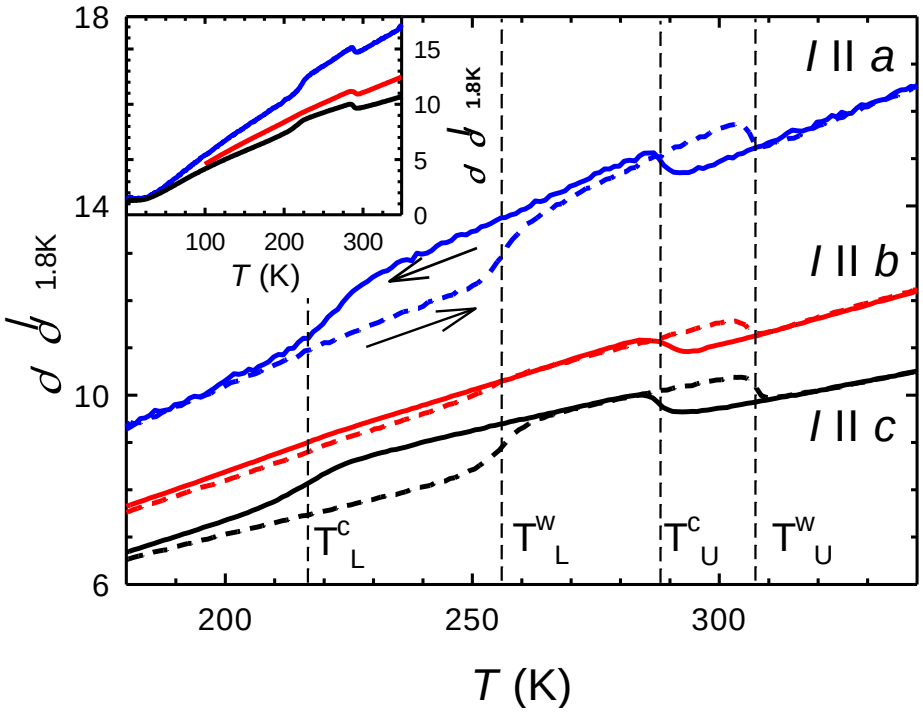

Fig. 3.6: Electrical resistivity of a CeRuSn sample from batch #2 along main crystallographic axes normalized by 1.8 K values. The vertical dashed lines mark positions of structural transitions. Indexes c and w signify positions during cooling and heating, respectively. The inset shows dependencies in the whole temperature range.

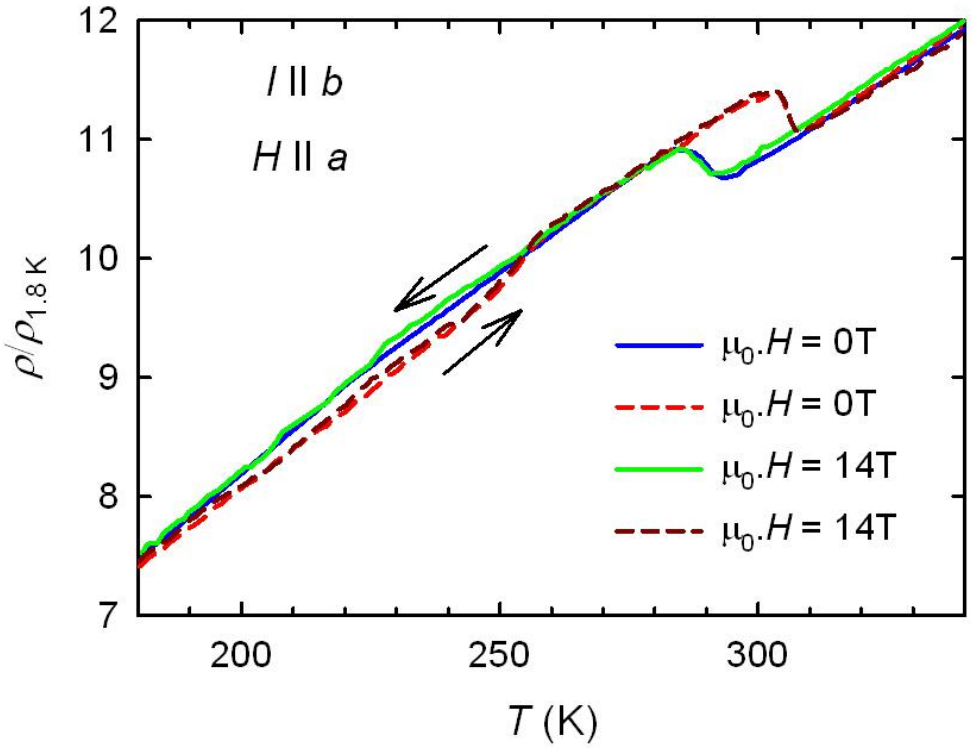

Fig. 3.7: Electrical resistivity of a sample from batch #2 in zero and 14 T magnetic field. The solid and dashed curves were obtained during cooling and heating cycles, respectively.

The RRR ratios ($\boldsymbol{RRR} = \frac{\rho_{320\,K}}{\rho_{1.8\,K}}$) pointed out a good quality of our single crystal reaching 16, 12 and 10 for *a*, *b* and *c*-axis, respectively. The different values for the three directions reflected the anisotropy of the phonon spectra of the compound. Comparing these values with polycrystalline data,(47) we can say that our single crystals are of much higher quality. That would explain why in the polycrystalline case (*RRR* ~ 2) the hysteresis is much bigger (~ 100 K) and only the first transition could be traced up, see Fig. 3.8. This is in some way analogous to the behavior of our as cast sample from batch #10, which had a very low value of *RRR* ~ 3.5. Only the first transition was identified too. Furthermore the transition was found at much lower temperatures ~ 190 K (cooling) and ~ 280 K (heating). Sample quality seems to be a very important factor influencing how well the transitions are pronounced. In case of worse samples, we may expect a smearing out of the ST,

because of a broad distribution of transition temperatures arising from different parts of the sample.

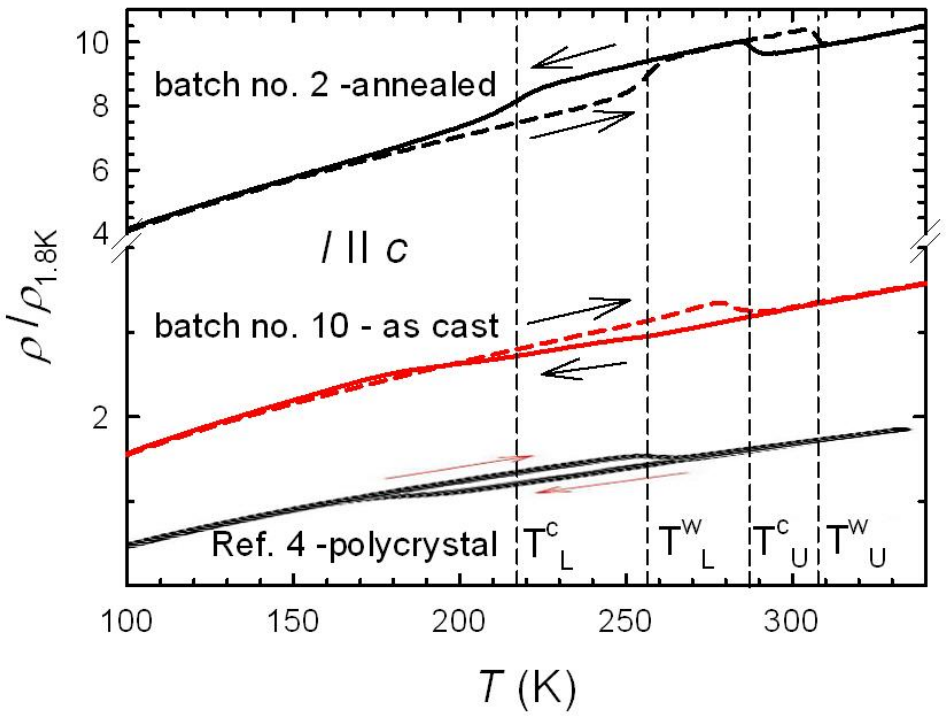

Fig. 3.8: A comparison of electrical resistivity measured along *c*-axis of an annealed sample (batch #2), an as cast sample (batch #10) and a polycrystalline sample from Ref.(47)

3.3.2. Magnetic susceptibility

The ST are also nicely reflected in the temperature dependences of magnetic susceptibility *M*/*H*. As can be seen in Fig. 3.9, the magnetization is highly anisotropic due to low local symmetry of the crystal electric field (CEF) acting on the *f*-orbital of Ce ions. Unlike the electrical resistivity, magnetic susceptibility manifests two similar step-like anomalies at the transitions temperatures. The former is approximately two times bigger than the latter. In both cases the drop may signal a change in Cerium valence or an enhancement of local screening by conduction electrons that is due to Kondo effect. In any case the effective moments obtained

from fitting the susceptibility M/H to a modified Curie-Weiss law formula (Fig. 3.11) decrease below the transitions for the *a*-axis, whereas in the other two directions they are not affected. All these parameters are summarized in Table 3.3. Effective moments do not reach the theoretically expected value for a free Ce^{3+} ion 2.54 μ_B, which goes in hand with previous results on polycrystalline samples where half of Cerium atoms were expected to be in a non-integer valence state.(44) The paramagnetic Curie temperatures and the χ_0 parameters did not exhibit any clear systematics, but they are mostly negative or close to zero revealing that antiferromagnetic correlation prevail in the paramagnetic range. The χ_0 values did not exceed 10^{-8} m^3/mol, hence we do not show them.

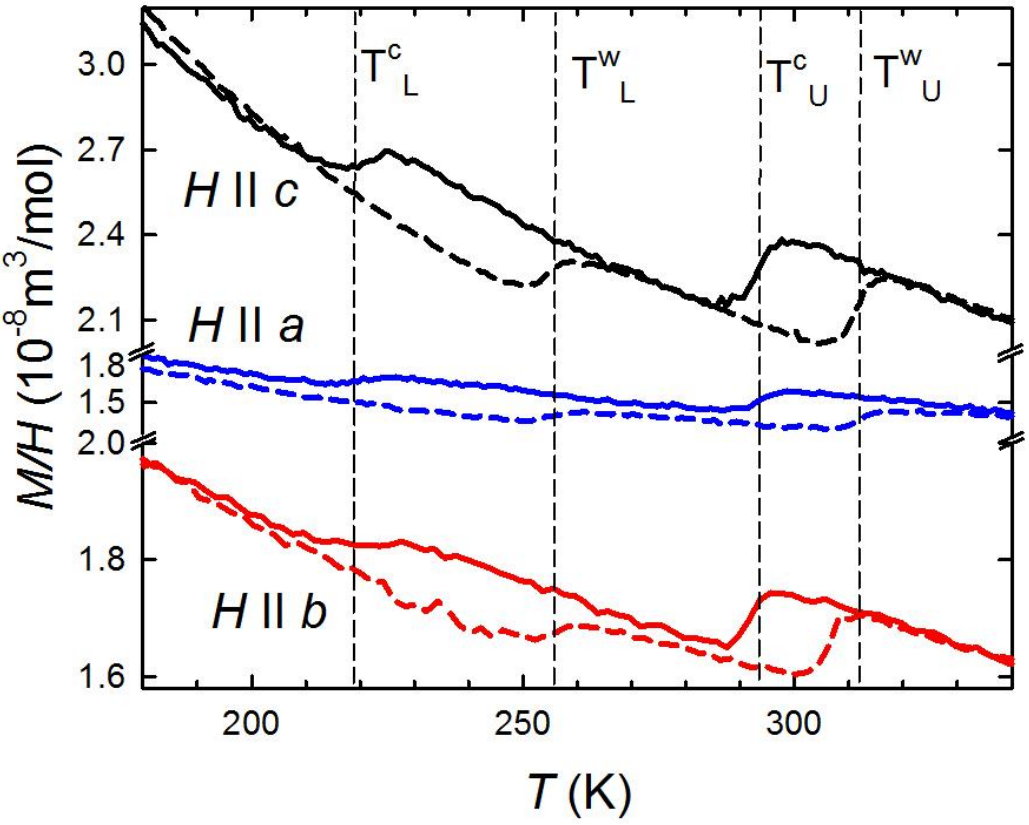

Fig. 3.9: The temperature dependences of magnetic susceptibility M/H along main crystallographic axes. The dashed and full lines are heating and cooling characteristics, respectively. Mind the differences and breaks in the *y*-axis scale. The vertical dashed lines again mark the ST.

It should be noted that magnetization is strongly influenced by sample quality. Exemplarily M/H dependences for two different batches are displayed in Fig. 3.9. Batch #4 was prepared by pulling from a stoichiometric polycrystalline button, whereas batch #13 originated from a button containing some excess of Ruthenium. While for the *c*-axes, curves are almost the same, in case of the *a*-axes, deviations are evident. Most significantly, the lower transition is worse defined in the batch #13 sample. It does not have the form of a step but only the slope of H/M curve changes at T_L^C. On the other hand during heating, an indication of a step (marked by an arrow in Fig. 3.10) can be seen. Another point is that the sample from the batch #13 had a bigger size and may have contained parts from the outer side of the ingot, which were not exactly oriented as the majority of the sample. The curvature ($T < 50$ K) visible along the *b*-axis of the batch #4 sample is reflected slightly in the $H \parallel a$ dependence of the batch #13 as here, in comparison to the $H \parallel a$ of the batch #4, one observes an additional bending.

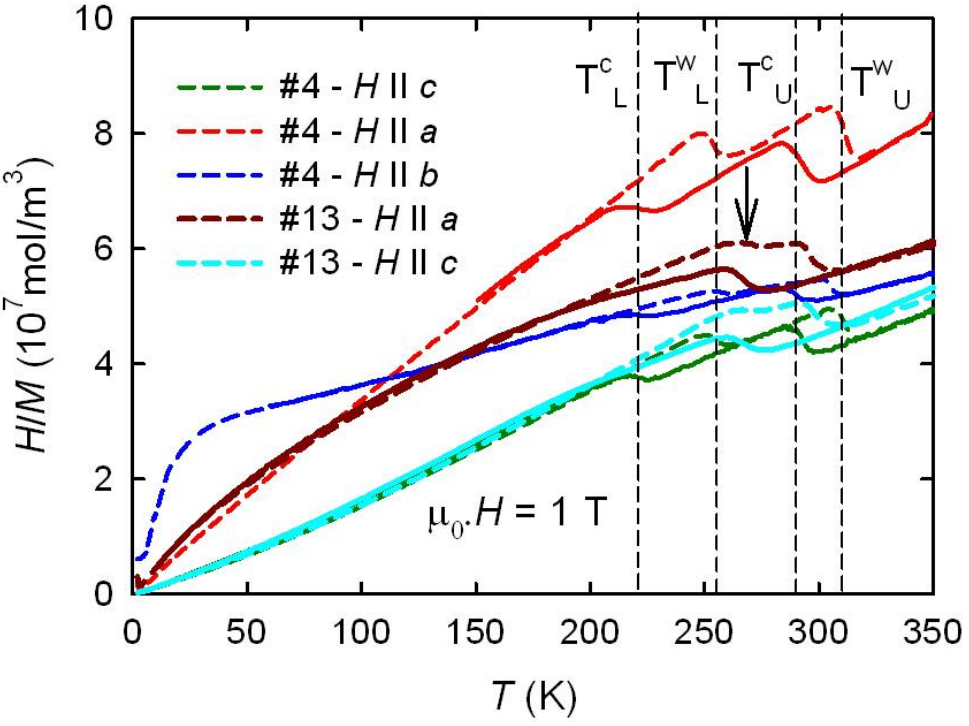

Fig. 3.10: The temperature dependences of H/M at the field of 1 T for two different samples from batch #4 and #13 measured along main crystallographic axes. Cooling and warming curves are given by the dashed and full lines, respectively.

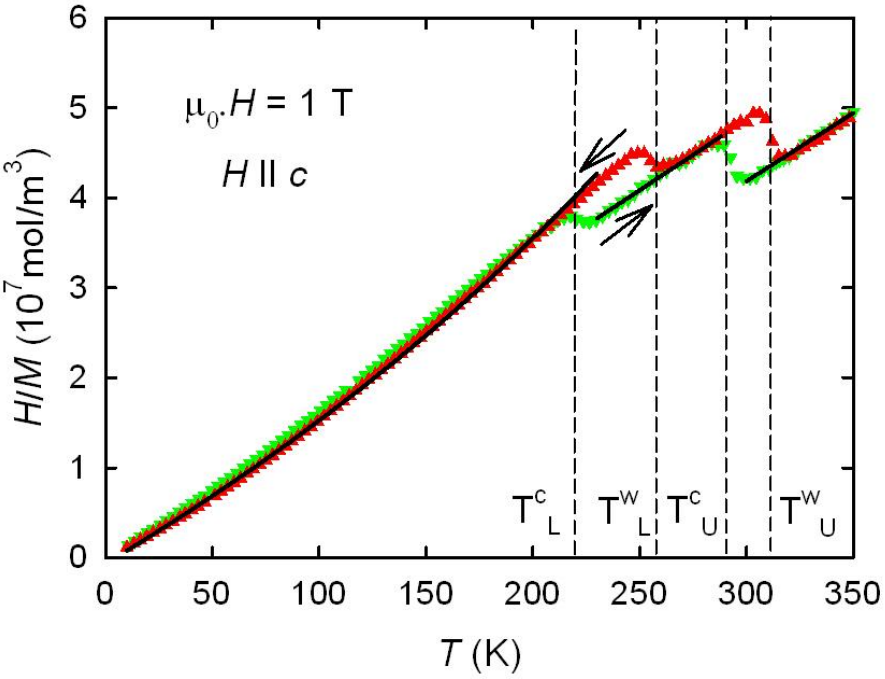

Fig. 3.11: *M*/*H* dependences measured along the *c*-axis of a sample from batch #4 are represented by red triangles (heating cycle) and green reversed triangles (cooling). Fittings of the experimental data by a modified Curie-Weiss law according to parameters from Table 3.3. in restricted temperature intervals are visualized by black lines.

Table 3.3: Parameters obtained from fitting the *H*/*M* curves shown in Fig. 3.10 to a modified Curie-Weiss law. Ce^{3+}/Ce values estimate fractions of Ce^{3+} ions in the samples at different temperature ranges.

batch #4					batch #13			
axis	T (K)	μ_{eff} (μ_B/f.u.)	θ_p(K)	Ce^{3+}/Ce	T (K)	μ_{eff} (μ_B/f.u.)	θ_p (K)	Ce^{3+}/Ce
a	10-230	1.36	-0.2	0.28	10-240	1.30	-5.8	0.26
a	288-230	1.14	42	0.20	258-202	1.34	-56	0.28
a	350-300	1.743	-41	0.47	400-300	2.21	-125	0.76
b	110-230	2.31	-210	0.83				
b	287-229	2.68	-315	1.11				
b	350-300	2.59	-236	1.04				
c	10-230	2.107	4.4	0.69	10-240	2.06	5.0	0.66
c	288-230	2.011	-9.7	0.63	250-190	1.82	-12	0.51
c	350-300	2.05	23.5	0.65	400-300	2.04	23	0.65

3.3.3. Thermal expansion

Since we were studying ST, getting direct information about lattice changes was highly desirable. The shaped single crystal from susceptibility measurements (batch #4) was also inspected by thermal expansion. Fig. 3.12 shows the result of our investigation. The indicated transition temperatures are taken from electrical resistivity measurements to keep the results comparable. When passing the ST during cooling, the crystal shrinks along the *c*-axis by roughly 0.4 % as a result of the first transition and by 0.2 % below the second one. On the other hand a slight expansion takes place along the other axes, whereas the overall contraction during cooling is much smaller. According to that, the evolution of volume is mainly reflected by the behavior of the *c*-axis. The volume reduces by 1.2 % from 340 to 180 K. The transitions take place at almost the same temperatures as in other experimental methods and are also connected with large thermal hysteresis. The volume reduction may be a consequence of change in Cerium valences on different sites, because Ce^{3+} ions have a bigger radius (115 pm) in comparison with Ce^{4+} ones (101 pm). This would also explain why effective moments in magnetization measurements reduce below each transition.

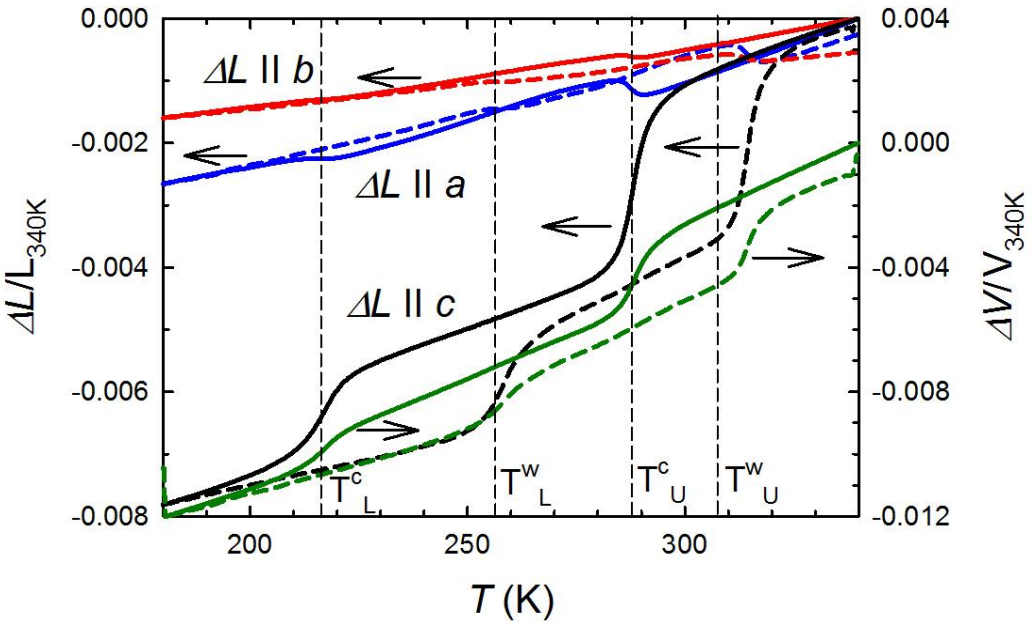

Fig. 3.12: Thermal expansion determined along different crystal directions.

3.3.4. Single crystal X-ray diffraction

From Fig. 3.5 we know that the room temperature structure is stable up to the melting point. In order to establish a complete picture about structure below RT, we measured X-ray single crystal diffraction on a piece of annealed single crystal from batch #2. We measured at five different temperatures during cooling and heating the sample to investigate all regions around the ST, see Fig. 3.13. The refinement of the diffraction patterns revealed that each three different structure polymorphs. These are depicted in Fig. 3.14. For all three the C2/m group is preserved. However tiny changes of inter-atomic distances give rise to different modulations along the *c*-axis. At RT the structure is in very good agreement with already published data(44) and with our powder X-ray diffraction measurements. The structure consists of two unit cells of CeCoAl-type stacked along the *c*-axis. Upon cooling through the first transition, the structure increases its modulation along the *c*-axis, becoming quintuple with respect to CeCoAl at 275 K. Accordingly the number of independent crystallographic sites increases from two to five. Finally below T^{C}_{L}, the unit cell describing the CeRuSn structure at 120 K can be viewed as a tripling of the CeCoAl unit cell. Three different Cerium sites can be distinguished. Table 3.4 summarizes lattice parameters and Table 3.5 gives information about the environment of different Cerium atoms and their fractional coordinates within the unit cells. Although the number of different Cerium sites is five, we can basically categorize them in three types of them: those having short distances from Ruthenium atoms Ce(S), those having large Ce-Ru separations Ce(L) and those having a combination of one short and one longer distance to neighboring Ru ions Ce(I), see Table 3.5 a). The change in stacking of these sites with each ST is as follows:

- L | L SS L | L SS L | L SS L | L SS L | L SS L | L SS L | L SS L | L SS
- LL S | S LL SI IS LL S | S LL SI IS LL S | S LL SI IS LL S | S LL
- LL SI | IS LL SI | IS LL SI | IS LL SI | IS LL SI | IS LL SI | IS LL

It can be seen that the first transition modifies the structure in such a way that it introduces two spacers of with Ce(I) sites in between every second SS layers.

The second transition again inserts an II layer combination into the structure separating the remaining SS layer pairs (see Fig. 3.14).

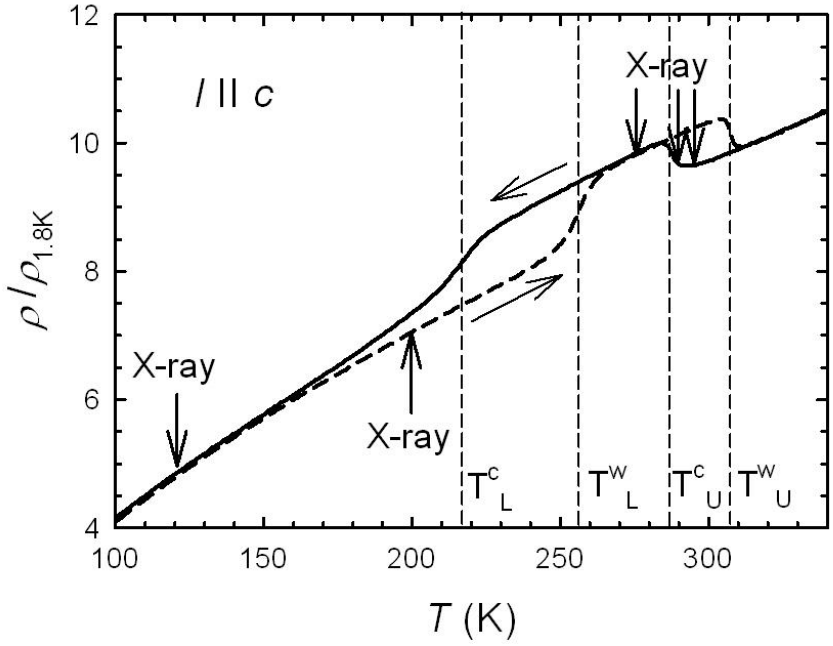

Fig. 3.13: Electrical resistivity of a CeRuSn sample (batch #2) measured along *c*-axis. The X-ray labels mark the temperatures where X-ray single crystal diffraction was measured.

As it is shown in Table 3.4, *a* and *b* lattice parameters do not evolve significantly with temperature contrasting to the drastic changes in the *c*-parameter. This one is not only modified due to different unit cell describing the actual crystal structure, but also shrinks in absolute values with temperature regardless of which modulation takes place. At 275 K, *c* decreases about 0.47 % and by another 0.29 % at 120 K when compared to the *c*-parameter at 297 K. These values quantitatively agree with direct measurements by thermal expansion. The authors in a different single crystal X-ray study(46) reported slightly bigger reduction 0.89 % of the *c*-axis, but this may due to taking a lower second temperature of 10 K for this calculation. The shrinkages can be explained by increasing number of short Ce-Ru separations, which are oriented almost entirely along the *c*-direction.

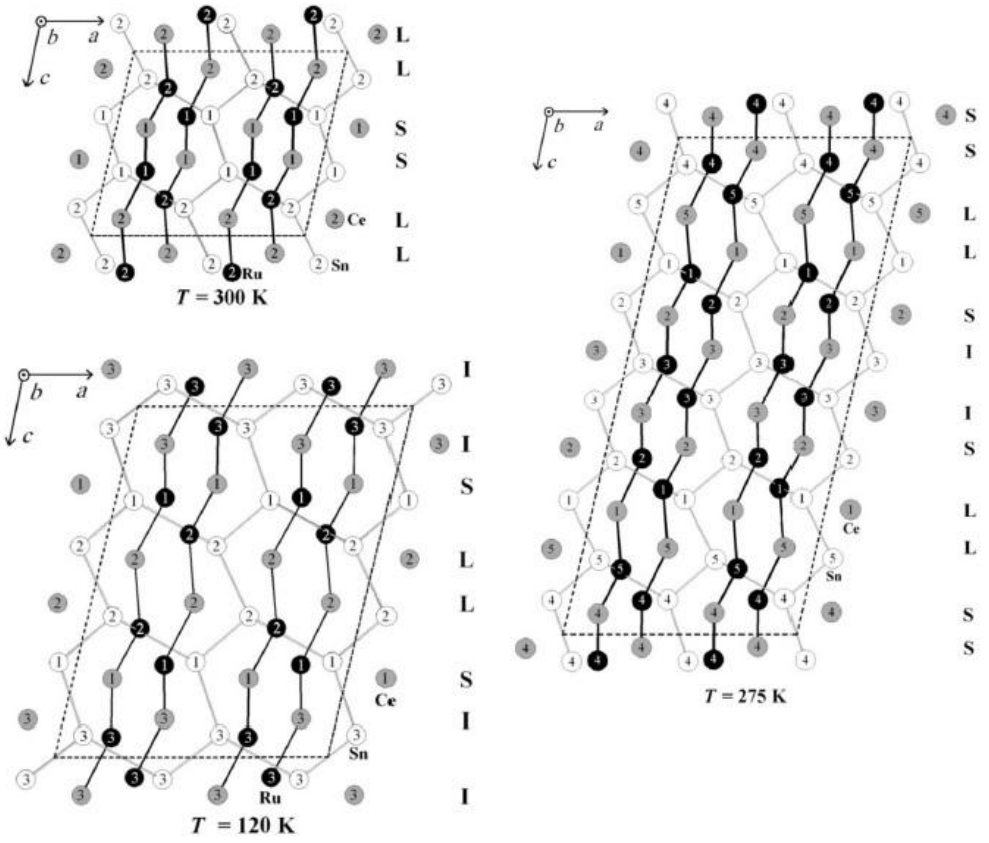

Fig. 3.14: Structure polymorphs found for CeRuSn at three different temperatures seen from the *b*-axis direction. Unit cells are highlighted by dashed rectangles. Letters on the right next to each structure mark different Cerium sites with shortly distanced (S), long-distanced (L) and intermediate-distanced (I) Ruthenium neighbors.

Table 3.4: Lattice parameters of CeRuSn determined by X-ray single crystal diffraction at various temperatures. Data are sorted according to temperature evolution during the experiment. $(c_T - c_{297\,K})/c_{297\,K}$ was calculated from the 297 K *c*-parameter in order to estimate real reduction of crystal dimension along the *c*-direction with temperature.

T (K)	a (Å)	b (Å)	c (Å)	β (deg)	V (Å^3)	$(c_T - c_{297\,K})/c_{297\,K}$ (%)
297	11.565(1)	4.7529(5)	10.2299(9)	103.028(2)	547.85(9)	-
290	11.560(3)	4.751(1)	10.227(3)	103.081(7)	547.1(2)	0.028(1)
275	11.576(2)	4.7556(7)	25.454(3)	102.959(4)	1365.6(3)	0.47(1)
120	11.566(2)	4.7477(6)	15.229(2)	103.554(4)	813.0(2)	0.76(2)
200	11.569(2)	4.7505(6)	15.237(2)	103.496(4)	814.3(2)	0.70(2)

Table 3.5: a) Closest Ruthenium neighbors of Cerium atoms in three CeRuSn structure polymorphs. Below each Cerium label, letters S, L and I denote sites with shortly-, long- and intermediate-distanced closest Ruthenium atoms, respectively.

b) Fraction atomic coordinates *x/a*, *y/b* and *z/c* in CeRuSn crystal structures above (300 K) and below (120 K) structural transitions.

a)

***T* = 300 K**			***T* = 275 K**		
Ce1	2.3277(9)	Ru1	Ce1	2.8882(19)	Ru5
S	2.4661(11)	Ru2	L	2.9247(19)	Ru2
Ce2	2.8783(10)	Ru1	Ce2	2.4331(18)	Ru1
L	2.9081(10)	Ru2	S	2.4380(19)	Ru3
***T* = 120 K**			Ce3	2.271(2)	Ru2
Ce1	2.4324(18)	Ru2	I	2.7575(18)	Ru3
S	2.4345(18)	Ru3	Ce4	2.3219(19)	Ru4
Ce2	2.9153(17)	Ru1	S	2.4779(18)	Ru5
L	2.9257(18)	Ru2	Ce5	2.8800(18)	Ru4
Ce3	2.2676(17)	Ru1	L	2.9453(19)	Ru1
I	2.7482(17)	Ru3			

b)

***T* = 300 K**			
Ce1	0.1396	0	0.4146
Ce2	0.1225	0	0.9063
Sn1	0.4265	0	0.3469
Sn2	0.4043	0	0.8486
Ru1	0.1827	0	0.6481
Ru2	0.1983	0	0.1973
***T* = 120 K**			
Ce1	0.6304	0	0.1073
Ce2	0.3567	0	0.2216
Ce3	0.6223	0	0.4375
Sn1	0.0857	0	0.9375
Sn2	0.0965	0	0.6007
Sn3	0.0696	0	0.2688
Ru1	0.6785	0	0.2607
Ru2	0.2991	0	0.3655
Ru3	0.3102	0	0.0571

3.3.5. Electrical resistivity under high pressure

As we know from the X-ray and thermal expansion measurements, the ST appeared to be intimately coupled to the volume and to interatomic distances between Ce, Ru and Sn atoms. Thus it can be expected that they will be sensitive to high external pressure. For our purpose, the most straightforward method to check this conjecture appeared to be measuring of electrical resistivity under hydrostatic pressure. Because of the shape of the sample, which was cut out of the single crystal studied most, we were forced to measure along the *b*-axis, although the transitions are less pronounced in this case. Various pressures were applied and the impact on the ST is documented in Fig. 3.15. The ST are rapidly pushed to higher temperatures by pressure with ratio 125 K/GPa, see Fig. 3.16. Considering the shrinkages of

the *c*-axis, which accompany both transitions, this behavior is consistent and can be understood as stabilization of the low-temperature crystal structure (with the tripled CeCoAl-type unit cell), in which CeRuSn has the smallest volume. The distance between the ST does not change due to high pressure, as can be seen in the last column in Table 3.6. On the other hand we may trace up a tendency to decrease the hysteresis connected with each ST, but higher pressures and particularly higher achievable temperatures are needed in order to confirm this assumption.

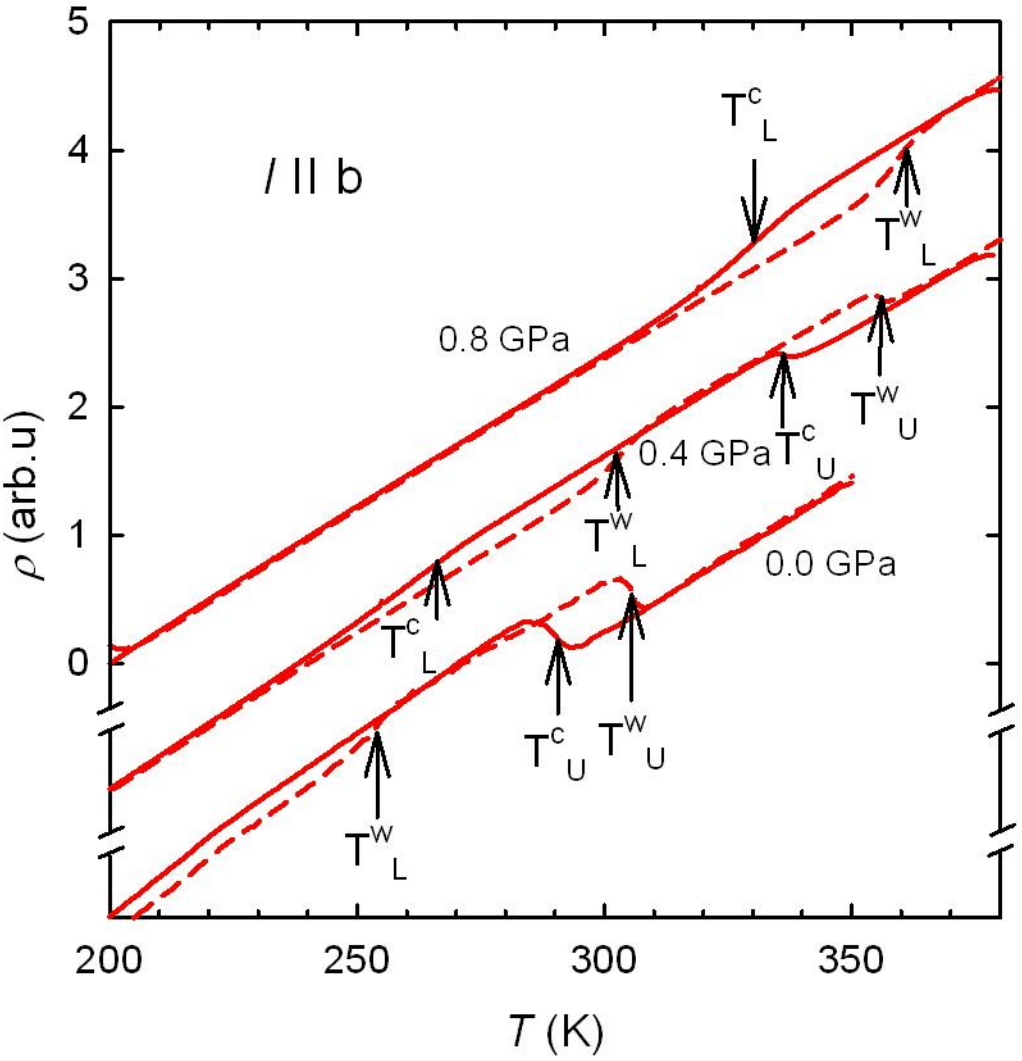

Fig. 3.15: Temperature dependences of electrical resistivity along the *b*-direction measured under high pressures and at ambient conditions. Heating and cooling measurements are depicted by dashed and full lines respectively. The curves are shifted for clarity.

Table 3.6: An overview of the transition temperatures at different hydrostatic pressures. Three last columns amount the size of temperature hysteresis of each transition and the distance between the ST during heating the sample.

p (Gpa)	T^{C}_{U} (K)	T^{W}_{U} (K)	T^{C}_{L} (K)	T^{W}_{L} (K)	$T^{W}_{U} - T^{C}_{U}$ (K)	$T^{W}_{L} - T^{C}_{L}$ (K)	$T^{W}_{U} - T^{W}_{L}$ (K)
0	290(3)	307(1)	219(3)	253(2)	17(3)	34(3)	54(2)
0.2	319(4)	336(1)	239(1)	281(1)	17(4)	42(2)	55(2)
0.4	339(4)	354(1)	262(4)	300(3)	15(5)	38(4)	54(3)
0.6	358(4)	371(1)	289(4)	316(1)	13(4)	27(4)	55(2)
0.8			332(3)	357(1)		25(3)	

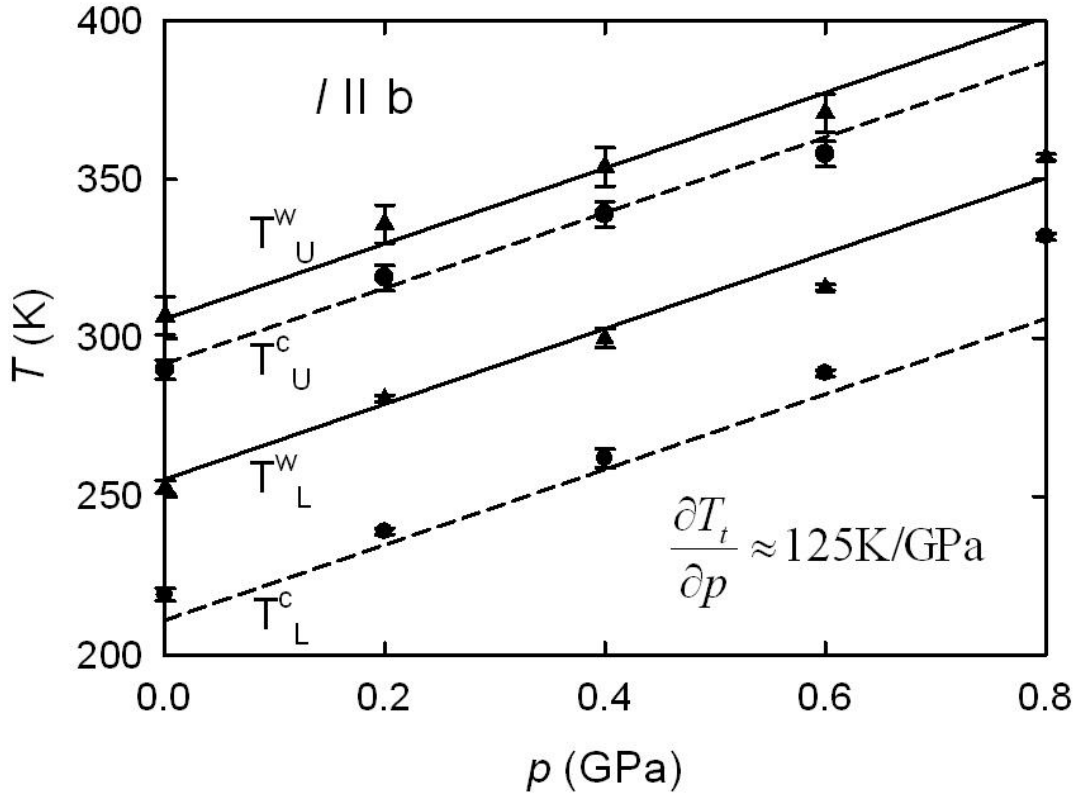

Fig. 3.16: Pressure dependences of the transition temperatures (Table 3.6) determined from electrical resistivity measured in the *b*-direction. Dashed and full lines have the same slope, which is written in the figure and connect transitions visible during cooling and heating.

3.4. Discussion on structural transitions

Both ST were visible in all available experimental methods. The transition temperatures well coincide among different physical properties, as can be seen in Fig. 3.17. A comparison of temperature derivatives of electrical resistivity, magnetic susceptibility and thermal expansion along the *c*-axis shows that maxima marking the ST are located at the same temperatures.

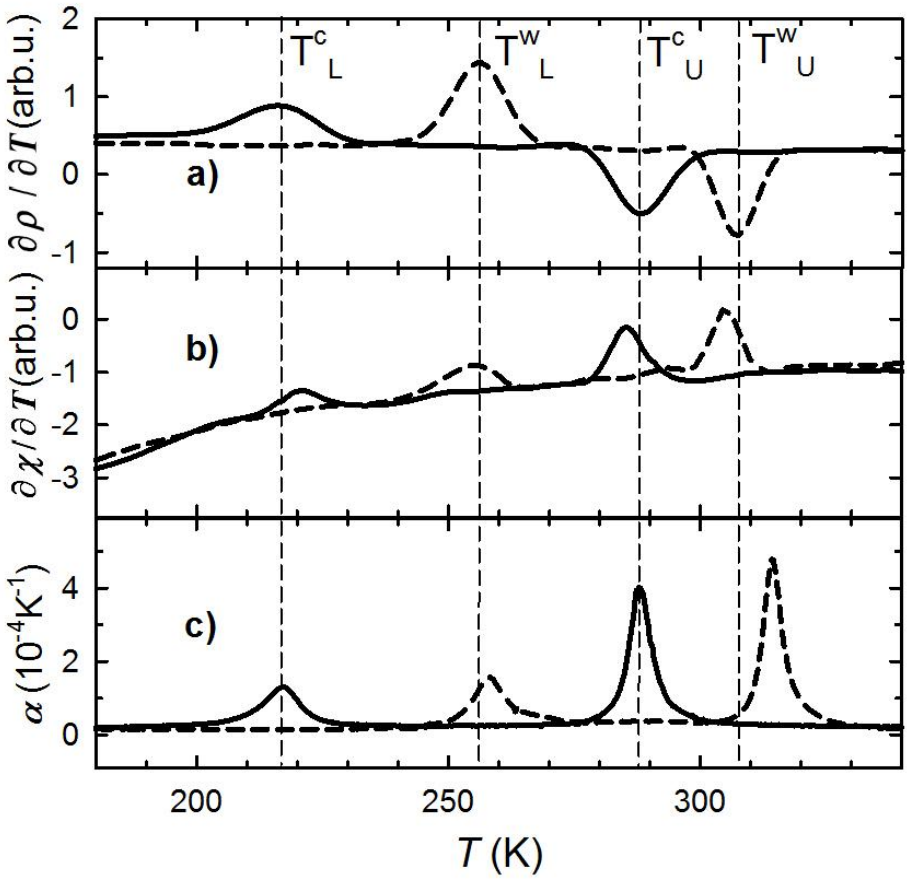

Fig. 3.17: Panels a) and b) – temperature derivatives of electrical resistivity (batch #2) and magnetic susceptibility (batch #4) measured along the *c*-axis. Panel c) – a coefficient of thermal expansion (batch #4) determined along the *c*-direction. All panels – heating and cooling dependences are represented by dashed and full lines respectively. Vertical dashed lines mark the transition temperatures established from electrical resistivity measurements.

From our measurements we got a picture about structural modifications in CeRuSn, which were visible in all experimental methods we used. Due to proximity of 4*f*-states to the Fermi level, we may expect that increase of electrical resistivity below T^{C}_{U} can be a manifestation of enhanced Kondo screening by conduction electrons. It would also explain why magnetic susceptibility on the contrary decreases. But it is not clear why electrical resistivity again falls below T^{C}_{D}. One possibility is that between the ST, a bigger modulation opens small gaps on the Fermi surface, which then decrease conductivity. Another explanation would be that the structure between the ST is more disordered and this has a similar impact on conduction electrons as would have more faults in the lattice, which would naturally increase residual resistivity. When the structure is stabilized with a smaller modulation below T^{C}_{D}, the resistivity again falls.

Our own study performed on single crystals(51) involving a big number of different experimental techniques revealed that there are in fact two isolated ST both connected with a large temperature hysteresis. The first occurs at 290 K and 307 K during cooling and heating, respectively. Analogically the second one can be found at 225 K and at 256 K. These temperatures are slightly sample-dependent, but the transitions are observable in all inspected physical properties, as can be seen in Figs. 4.17 and 4.18. The ST are manifested in the same way in the electrical resistivity and magnetic susceptibility along all axes, but they are least pronounced along the *b*-axis direction. Thermal expansion deviates from this scenario, when the ST cause contraction along the *c*-axis unlike the case of the remaining directions. That may origin in the fact that thermal expansion is somehow more coupled to the crystal lattice, while the other two methods are also dependent on the local electronic properties of the material. Our results confirm that the unit cell is at low temperatures three times larger than the basic CeCoAl-one, which is about one half bigger than for CeRuSn at RT. Below the ST, the number of inequivalent Cerium sites is increased from two to three, where two have significantly reduced Ce-Ru separations being smaller than the sum of Cerium and Ruthenium covalent radii. A significant contraction accompanies the structural transitions (ST) due to an increased number of short Ce-Ru distances per unit cell. This observation is supported by impact of high-pressure, which stabilizes the low temperature structure

and pushes the transitions towards higher temperatures. The enormous unit cell volume drop of 1.2 % is reminiscent to the γ→α transition in elemental Ce. Here the driving force for the volume collapse is still a matter of discussion.(52,53) Moreover, the increase of short Ce-Ru distances implies a change in overall valency. A recent study by XANES measurements(48) revealed that valence does decrease below ST and the drop may occur on one sixth of Cerium sites. The volume contraction derived from the valence change has the same magnitude as the real contraction determined by our thermal expansion measurements.(51) That confirmed our presumption about similarity with the elemental Cerium γ → α transition, which is also accompanied by a decrease of volume and change in valence.

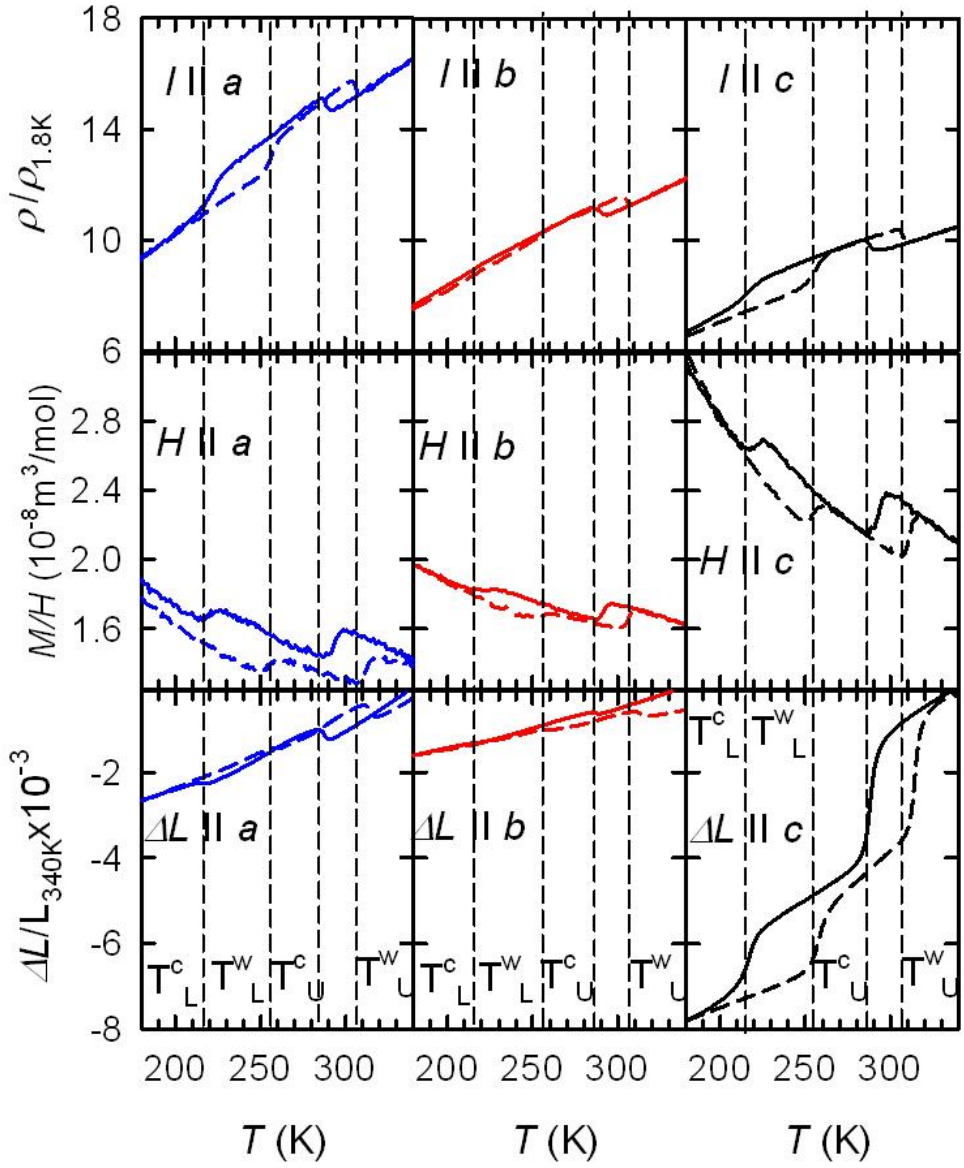

Fig. 3.18: A comparison of the ST anomalies in different experimental methods for each main crystallographic axis. From the top to the bottom: electrical resistivity curves, magnetic susceptibility curves M/*H* and thermal expansion.

At the same time, the CeRuSn crystal structure at low temperatures was investigated also by Feyerherm et al.(46) utilizing synchrotron radiation. They reported a superstructure formation manifested by additional peaks in diffraction patterns. These superstructures could be ascribed to nearly integer inverse-folded *c*-components of propagation vectors having all other components zero. The first additional reflections appeared just below RT changing the ½ modulation into

1/5-like one in accordance with our data. At 210 K the spectral weight moves from the 1/5-like superstructure peaks towards ¼-like ones. Below 180 K a 1/3-like modulation is dominant, but those two aforementioned modulations (1/5, 1/4) are still present down to lowest achieved temperatures (100 K). We cannot see a direct evidence for arising of the ¼-like modulations in our electrical resistivity, magnetization or thermal expansion data. Such ¼-modulation was also not recognized in our own X-ray diffraction study. Considering the discrepancy in literature about the CeRuSn valence, which was firstly reported to stay constant(46) throughout the ST and then to slightly decrease below the ST, we may speculate that the ¼-like modulation was caused by some sample imperfections. On the other hand our refinement did not take into account all available satellites and our low-temperature structure is only an approximation to the real one, although to a very good degree. More recent crystal structure study via neutrons by Prokeš et al.(49) states that below ST CeRuSn transforms into an incommensurate structure describable by a propagation vector (0 0 0.35). That is very close to one third concluded from our data and we cannot basically distinguish between them.

DTA measurements helped to find out if the RT structure is the final form, which is stable up to the melting point, or it is to be replaced by some having form of CeCoAl with only one Cerium site per unit cell. No sign of the latter scenario was found in our data, which would be marked by a clear anomaly in DTA curves. That confirms a tentative picture where the low temperature structure withdraws in two steps during temperature annealing. Less complicated structures subsequently arise during each transition via excluding layers containing two sets of I Cerium sites.

A point, which should be clarified, is whether the valence states of Cerium atoms at different sites change because of the ST. According to first XANES measurements,(46) the average valence should stay 3.18 between 320 and 100 K. A later XANES study(48) performed on freshly cleaved surface of CeRuSn single crystals revealed that overall valence in fact falls from 3.18 at 320 K to 3.15 at 100 K due to ST. Assigning this change to only sixth of Cerium atoms, which join the short-distanced sites below the ST, valence would change from 3+ at 320 K to 3.26+ at 100 K on these sites. But this does not exclude valence changes on different Cerium sites. Considering complicated environments of each Cerium

crystallographic position and their evolution with temperature, we may speculate that valence may be modified in case of more than one sixth of Cerium sites and cancelled out in average. Taking into account different volumes of Ce^{3+} and Ce^{4+} ions, calculated lattice contraction 0.8 % equals the real lattice contraction obtained from our thermal expansion measurements. Furthermore this would cause local volume contraction 10 % on 1/6 of Cerium sites. That, compared with volume drop 14 % in case of elemental Cerium, confirms our conclusion about similarity with the $\gamma \rightarrow \alpha$ transition. We add that valence changes there from 3.03+ to 3.19+. Moreover the pressure dependence of the transition temperatures in CeRuSn is very alike to the $\gamma \rightarrow \alpha$ transition in Cerium, which shifts to higher temperatures and almost linearly having the slope roughly 250 K/GPa,(54,55) which is twice the value we obtained for CeRuSn. But in our case Cerium atoms are dissolved in a bigger lattice that may have weakened the impact of high pressure here.

There are several mechanisms, which can be responsible for the ST. Taking into account similarity with the transition in elemental Cerium, steps in magnetic susceptibility and electrical resistivity, we may assign the transitions to Kondo-volume-collapse scenario where local moments become partially screened by conduction electrons.(56,57) That would explain both phenomena. The former would origin from screening of local moments by conduction electron spins and the latter by additional scattering conduction electrons off magnetic impurity atoms. More recent papers on the $\gamma \rightarrow \alpha$ transition suggest that the role of lattice vibrations and charge and spin degrees of freedom may be also very important.(58,59) Alternatively we may consider the ST as a sort of Mott transitions, in which the localized Cerium *f*-electrons become itinerant and participate in bonding.(60)

3.4. Low-temperature properties

CeRuSn was reported to undergo a transition into magnetically ordered state at 2.7(1) K.(47) The measurements on polycrystalline samples revealed an anomaly in specific heat and magnetization, which shifts to lower temperatures with magnetic field implying antiferromagnetic arrangement of magnetic moments. A series of at least three metamagnetic transitions was observed in small magnetic fields (< 1.5 T) in the 0.5 K isothermal magnetization measurements corroborated antiferromagnetic state in this temperature. The magnetic moment of 0.53 μ_B/f.u. at 7 T field is significantly lower than expected for appearance of Ce^{3+} ions only (2.16 μ_B). Broadening of ^{119}Sn NMR spectra towards low temperatures also support the scenario of the antiferromagnetic ground state.(61) Finally, neutron powder diffraction experiments(62) confirmed that CeRuSn is antiferromagnetic below 2.8 K. The magnetic structure was described by two incommensurate propagation vectors q_1 = (0 0 0.30) and q_2 = (0 0 0.43) giving a cycloidal structure with Ce ions carrying an effective moment of ≈ 0.7 μ_B. The moments lie in the *a*-*c* plane. However, ambiguous PC data as well as multi-phasing of the low temperature crystal structure, as discussed in the section 4.3., complicated the interpretation. Exact details about the magnetic ground state remained elusive.

Since high quality single crystals are indispensable to gain reliable information about magnetically ordered state and its anisotropy, we performed our whole study at low temperatures purely on single crystalline samples. A number of experimental techniques e.g. magnetization, specific heat, electrical resistivity, thermal expansion, was employed to shed more light on the antiferromagnetic state at low temperatures. If not mentioned explicitly, the measurements were performed on a sample from batch #4 (labeled as #401). In addition, the impact of high pressure on the magnetization and electrical resistivity was studied for temperatures below 10 K.

3.4.1. Magnetization

The temperature scans of magnetic susceptibility (*M/H*) below 10 K are depicted in Fig. 3.19. The ZFC and FC dependences did not differ (i.e. data are lying

on top of each other), thus we show only the latter ones. For field oriented along the *a*- and *c*-axis we found a maximum located at 2.9 K. This anomaly would suggest that the Néel temperature lays higher than reported in literature (2.7 K).(47) But according to Fisher et al.(63), for simple antiferromagnets the correct position of Néel temperature can be established from susceptibility data as the temperature at which the derivative ($\partial T.\chi/\partial T$) has its maximum. The analysis of 0.1 T data gave critical temperatures 2.7 and 2.8 K (marked by arrows with T_N) for the *a*- and *c*-axis data, which are in better agreement with published results. On the other hand we found no anomaly but only saturation of the magnetic susceptibility below 2.8 K for field pointing along the *b*-axis even up to 7 T. The maxima in the *a*- and *c*-axis dependences are suppressed by external magnetic field as can be expected for antiferromagnetic ordering. The effect is stronger in the *c*-axis case where already the 1 T field pushes the maximum almost below our experimental limit of 1.8 K. In contrary, such field only slightly moves the anomaly when applied along the *a*-axis.

Anisotropic response of magnetization to the applied magnetic field is documented in isothermal magnetization curves at 1.8 K shown for all three axes in the bottom panel of Fig. 3.20. While two metamagnetic transitions (MT, marked by arrows) can be found for the *a*- and *c*-axis measurements, which are followed by a tendency to saturation above 4 T, the *b*-axis exhibits only a paramagnetic-like response up to 14 T field with much smaller values of magnetic moment. The metamagnetic transitions, which in fact signify a change of the slope in magnetization, were identified from maxima in ($\partial M/\partial H$) and are located at $\mu_0 H_m^a \approx 0.85$ T and ≈ 1.45 T for the *a*-axis and at $\mu_0 H_m^c \approx 0.56$ and ≈ 0.80 T for the *c*-axis. The appearance of metamagnetic transitions may be expected due to antiferromagnetic ordering and is usually found for crystal axes, where temperature dependence of magnetic susceptibility has maxima, which is also the case here. Above the MT we may expect that the antiferromagnetic coupling is broken and the magnetic structure is aligned-polarized towards one direction. As can be seen in the first two panels of Fig. 3.20, an increase of temperature pushes the MT towards lower fields and they vanish just above the Néel temperature at 3 K. The magnetic moments at 14 T reach values 0.51, 0.08 and 0.71 μB/f.u. for the *a*-, *b*- and *c*-axis, respectively. According to this, we identify the *c*-axis as the easy magnetization

direction, whereas the *b*-axis is the hard magnetization direction. The maximum values of magnetic moments are considerably smaller than anticipated for solely Ce^{3+} ions (2.16 μ_B). Furthermore the easy axis value 0.71 μ_B/f.u. suggests that only every third Cerium atom is in the 3+ valence state and carrying the full Ce^{3+} moment. This has been already suggested from the high-T experiments, see the previous section.

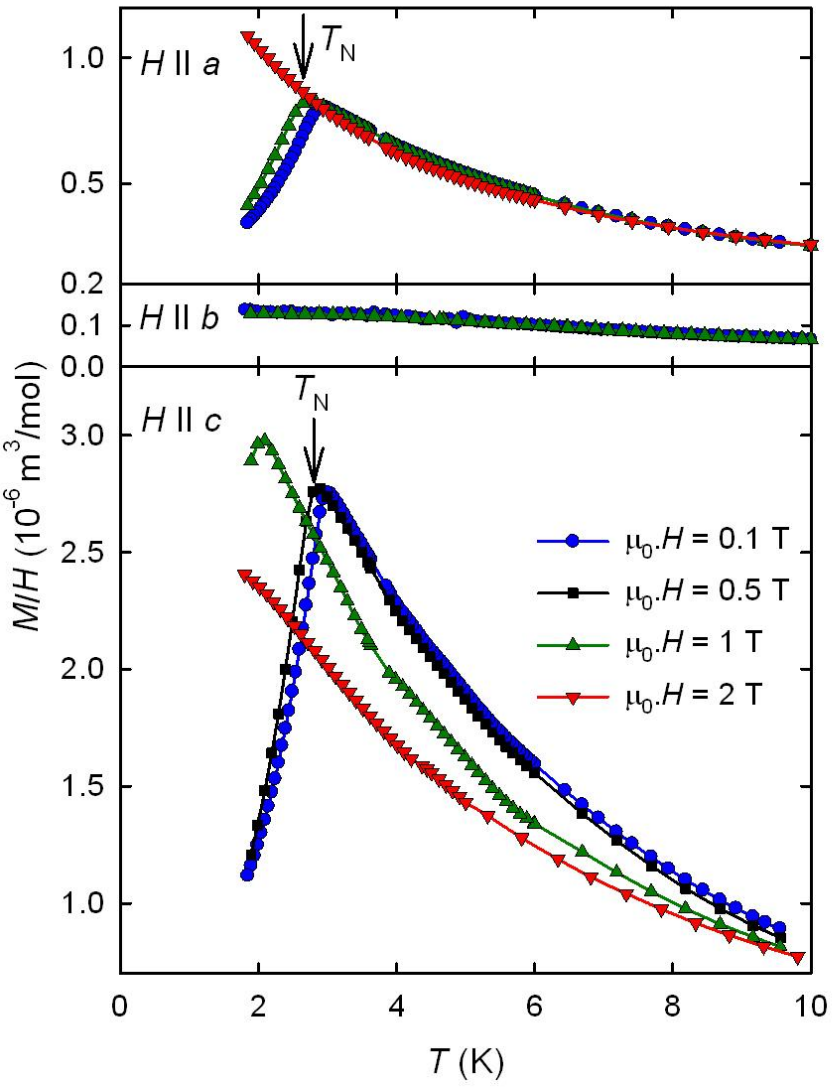

Fig. 3.19: Temperature dependences of *M*/*H* measured along main crystallographic axes at various magnetic fields. The vertical arrows mark the Néel temperatures determined from maxima in $\partial(TM/H)/\partial T$.

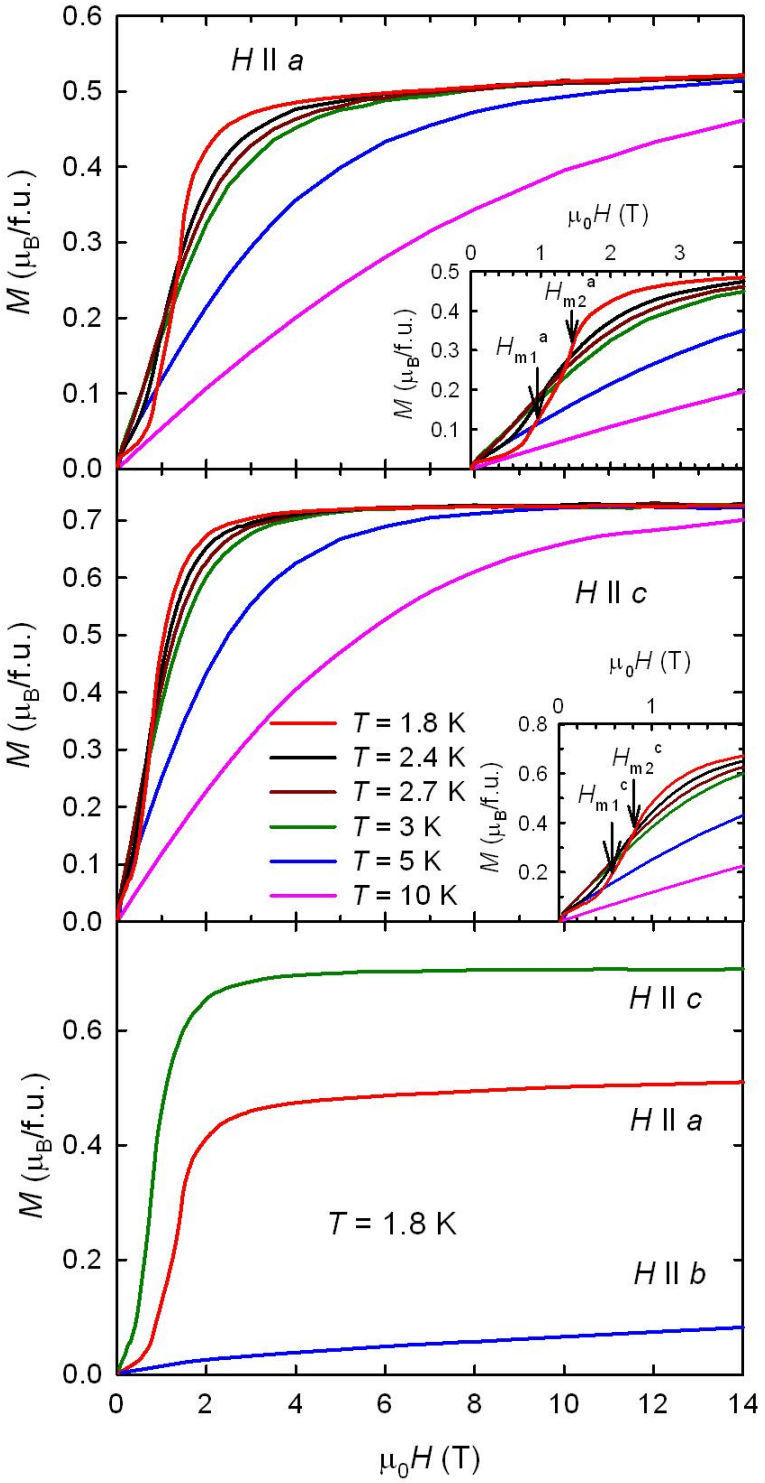

Fig. 3.20: First two panels – isothermal magnetization dependences determined at various temperatures ≤ 10 K along the *a*- and *c*-axis. The insets – low-field details of *M*(*H*). The arrows with H_{mi}^{a} and H_{mi}^{c} signify the MTs along the *a*- and *c*-axis, respectively. Bottom panel – a comparison of isothermal magnetizations collected along main crystallographic axes at 1.8 K.

3.4.2. Specific heat

In order to further document the magnetic anisotropy in the ordered state, we investigated the specific heat also with the magnetic field applied along the main crystallographic axes. As can be seen in Fig. 3.21, the specific heat contains a sharp anomaly at 2.7 K. This anomaly has a similar response to the magnetic field that is T_N moves to lower temperatures with increasing field, which is a clear sign of the AFM transition. As soon as the field exceeds the critical values needed for the second MT, a broad maximum develops and moves with increasing field to higher temperatures. Such behavior is typical for antiferromagnetic transitions where magnetic field helps to destroy antiparallel spin arrangement. When this is broken, the field supports orientation of magnetic moments towards the external magnetic field and such broad characteristics occur at higher temperatures. Contrary to this, the T_N-anomaly is almost intact by magnetic field oriented along *b*-axis even at 9 T, showing that the magnetic coupling is robust against fields along this direction. This behavior is in accordance with the paramagnetic-like response of magnetization to the magnetic field. The magnetic entropy calculated by eq. (9) is displayed in the bottom panel of Fig. 3.21. At these temperatures we may attribute it solely to the magnetic ordering. The entropy reaches 0.32 R ln2 at 4 K, which is very close to 1/3 R ln2. This value goes in hand with the scenario based on the magnetization measurements, that only one third of Cerium atoms participates in the AFM ordering.

In the insets of Fig. 3.21 we show a fitting of zero field data by eq. (7). The obtained Sommerfeld specific heat coefficients above T_N (the 2nd panel) and below it (the 3rd panel) are 45(2) mJ.mol^{-1}K^{-2} and 15(1) mJmol^{-1}K^{-2}, respectively. The three times lower value in the ordered state may point to a substantial Fermi surface modification below the Néel temperature.

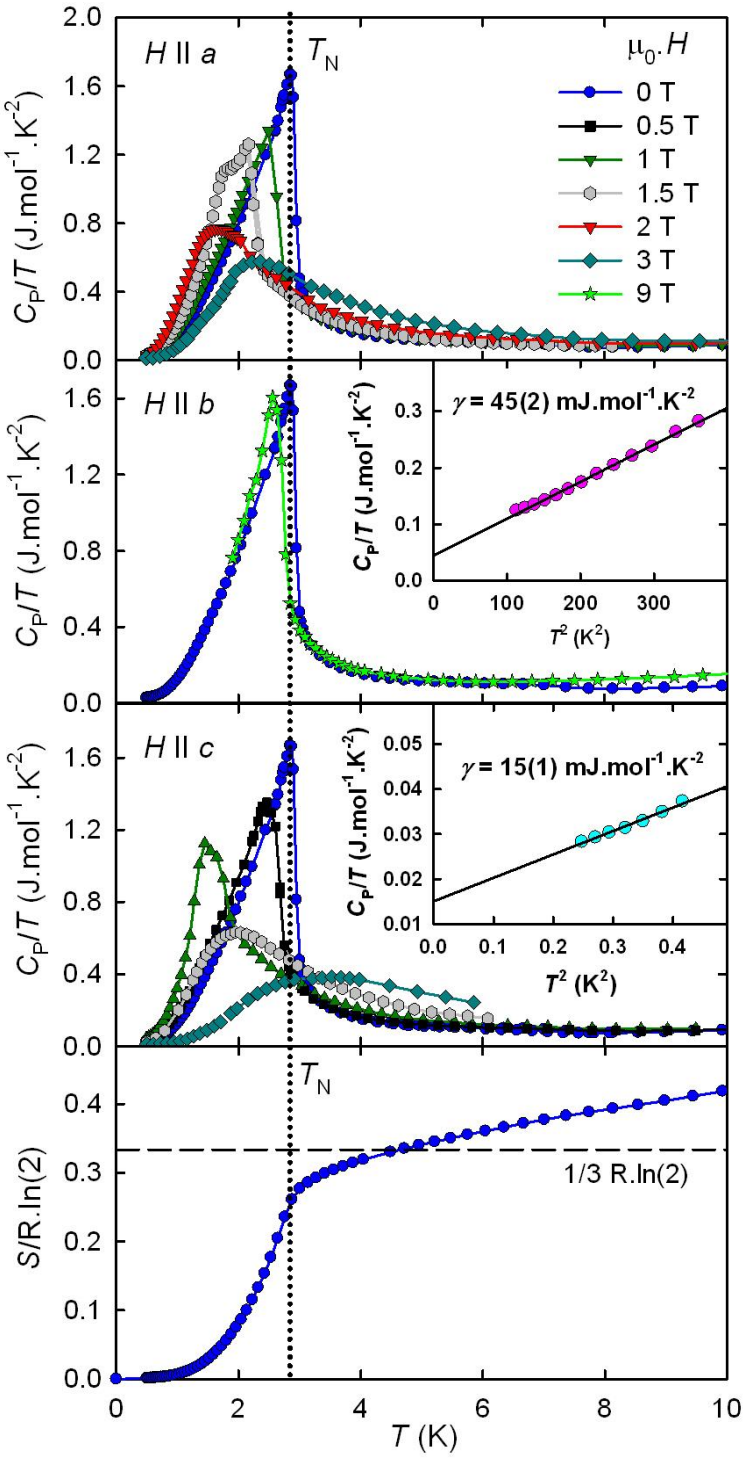

Fig. 3.21: First three panels – temperature dependences of reduced specific heat (C_p/T) in a number of magnetic fields applied along main crystallographic axes. The upper and the bottom inset - fittings of the zero field data by eq. (7) above and below the AFM transition, respectively. Bottom panel – the entropy calculated from zero field data by eq. (9). The vertical dotted line signifies the Néel temperature.

3.4.3. Electrical resistivity and magnetoresistance

Fig. 3.22 shows the temperature dependences of the electrical resistivity along the main crystallographic axes with the magnetic field applied along the current direction. The measurements were performed on the sample, which served also for high temperature electrical resistivity measurements (#209). The inset displays an extension down to 0.5 K on the sample #401. In the vicinity of the Néel temperature, the resistivity sharply drops in zero fields. This is due to a decrease of the spin-fluctuating dependent scattering when going from the paramagnetic state towards more coherent antiferromagnetic state.(64) Magnetic field widens the anomaly and in high fields even changes the resistivity behavior that is the slope for *a*- and *c*-axis becoming more Fermi-liquid like. Contrary no change occurs in behavior of the *b*-axis electrical resistivity in the whole temperature range. This is analogous to the magnetization and specific heat measurements, where the anomaly connected with the AFM transition is intact by magnetic field.

The effect of magnetic field is better illustrated on the longitudinal magnetoresistance (MR) dependencies depicted in Fig. 3.23. At fields close to the MT deduced from $M(H)$ along the *a*- and *c*-axis, we can see two anomalies. The first is a peak below the lower critical fields $\mu_0 H_{m1}^{a} = 0.85$ T and $\mu_0 H_{m1}^{c} = 0.56$ T for both axes. When the second MT is reached $\mu_0 H_{m2}^{a} = 1.45$ T and $\mu_0 H_{m2}^{c} = 0.80$ T, the spin-fluctuations cease. This is connected with a huge decrease of resistivity of about 30 % and 20 % percent for the *a*- and *c*-axis, respectively, suggesting a completely aligned field induced magnetic structure. In contrary, the *b*-axis MR is a smooth function of temperature in agreement with the isothermal magnetization data.

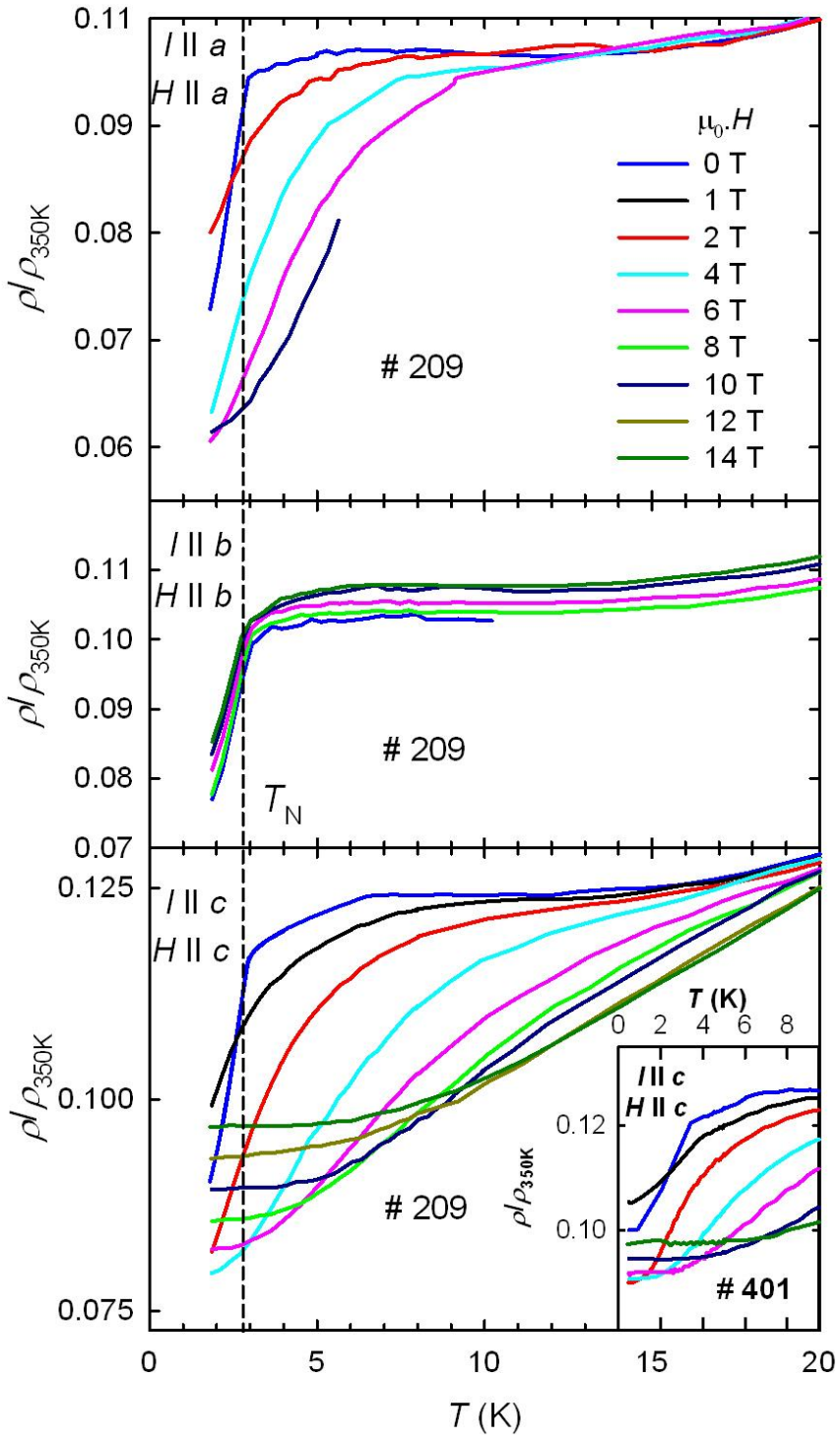

Fig. 3.22: Temperature scans of relative resistivity with both current and magnetic field oriented parallel to each crystallographic direction of a sample #209 from batch #2. The vertical dashed line represents the position of the Néel temperature (2.8 K). The inset shows an extension down to 0.5 K along the *c*-axis of a sample #401.

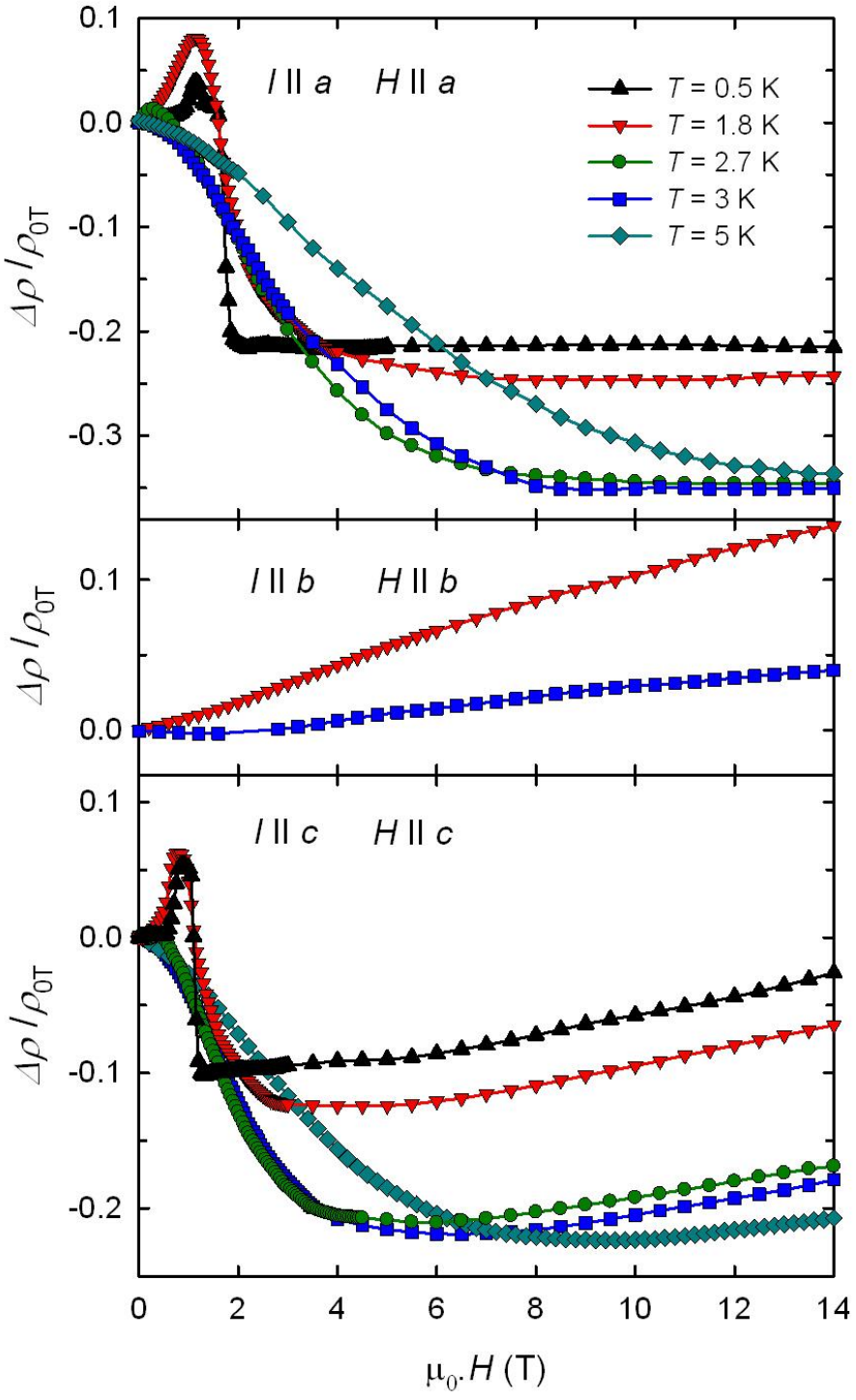

Fig. 3.23: Longitudinal magnetoresistances measured at various temperatures along main crystallographic axes.

3.4.4. Thermal expansion

Thermal expansion was measured in order to find a relation between the formation of the AFM state and lattice dimensions. Results are shown in Fig. 3.24. While for the *b*- and *c*-axis we observed a negative spontaneous magnetostriction below T_N, a positive feedback was found in the reciprocal *a*-axis direction. This is somehow surprising, since up to now behaviors for the *a*- and *c*-axis were much alike. The deviation of the reciprocal axis from the real one, which is 13º in CeRuSn, cannot explain the distinct feature. But in total the relative crystal volume decreases below T_N by 2.10^{-6}, which is usual for AFM materials.

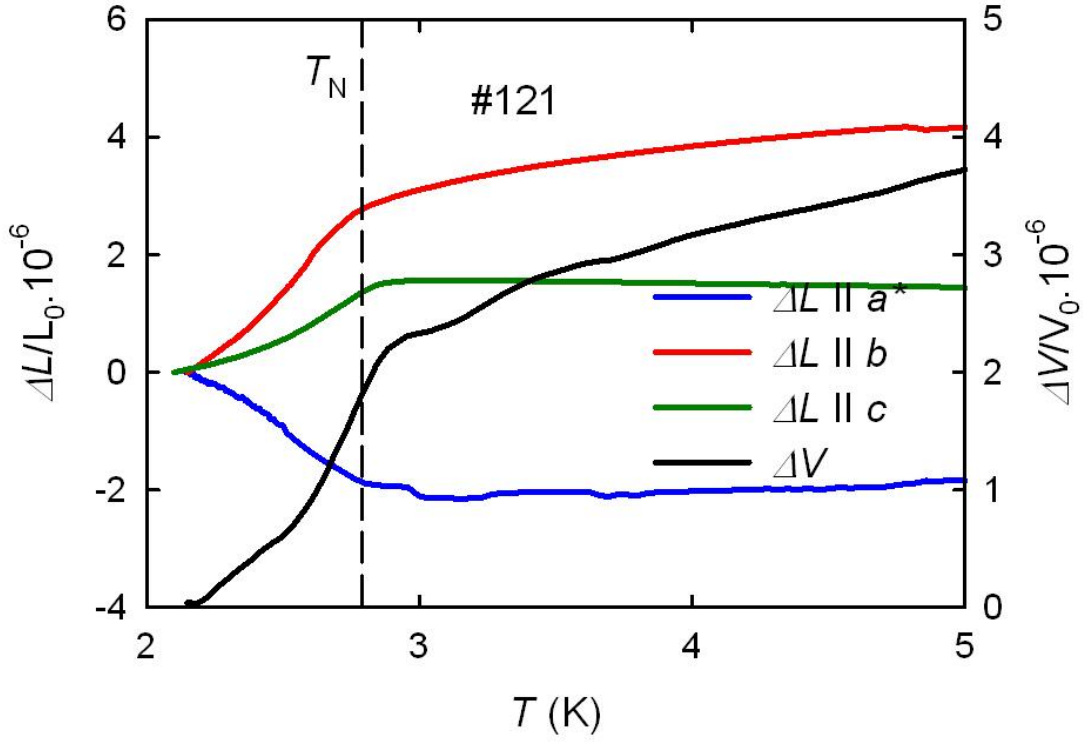

Fig. 3.24: Relative change of crystal dimensions of the sample #121 (batch #12) normalized to the dimensions at 2.1 K and the respective relative change of volume.

The thermal expansion along the *c*-axis under various magnetic fields applied parallel to it is plotted in Fig. 3.25. We can see that magnetic field here suppresses the anomaly connected with the AFM ordering towards lower temperatures too. Above the MT critical field at 2 T, the dependence has exactly opposite character when that is $\Delta L/L_0$ decreases with raising magnetic field.

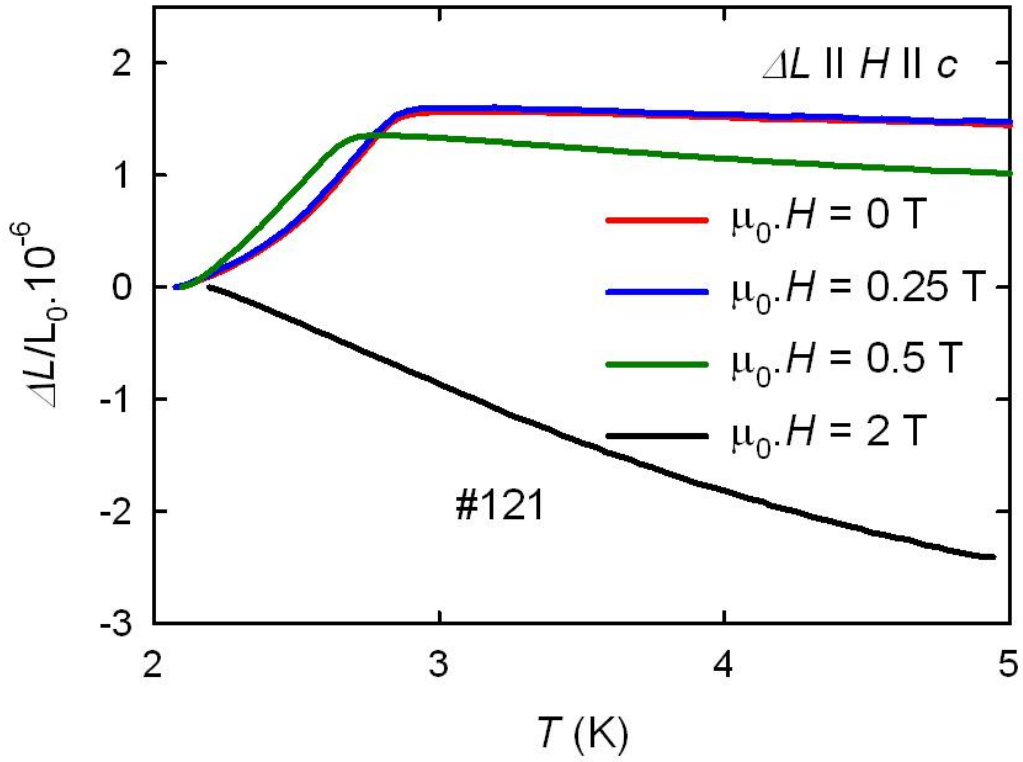

Fig. 3.25: Temperature scans of relative change in the *c*-axis direction of the sample #121 from 2.2 to 5 K under various magnetic fields oriented parallel to the measured direction.

3.4.5. High pressure measurements of magnetization and electrical resistivity

As mentioned in the theoretical background, it is always interesting to apply high pressure on Cerium- an Ytterbium-based compounds at low temperatures. Furthermore the ST appeared to be substantially affected by high pressure as described in the previous part of this chapter, what initiated our motivation for the low temperature study of magnetic properties with an application of high hydrostatic pressure.

The magnetic susceptibility measured along the *c*-axis at the 0.1 T field under various hydrostatic pressures is displayed in Fig. 3.26. With increasing pressure, the magnitude of susceptibility is slightly reduced. But, more interestingly,

the transition temperature is moved by pressure towards higher temperatures. This is very surprising if we recall that *M* becomes slightly suppressed and moreover that Cerium systems are usually driven by pressure to a QCP where the magnetic order vanishes.

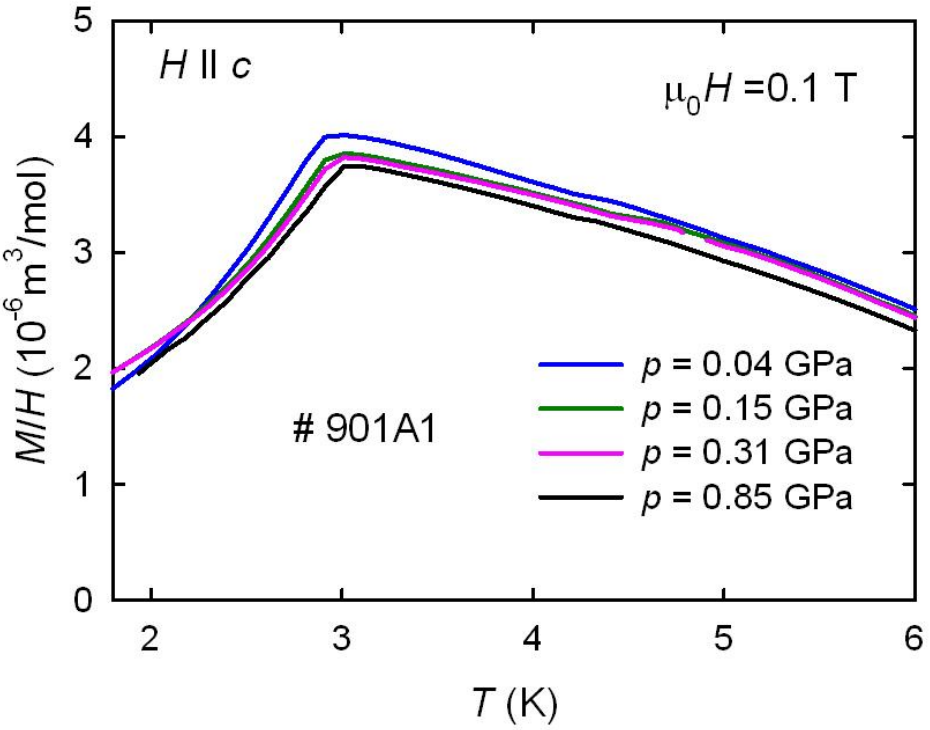

Fig. 3.26: Temperature dependences of magnetic susceptibility of sample #901A1 (batch #9) along the *c*-axis at 0.1 T field under four different hydrostatic pressures.

The isothermal magnetization curves at 1.8 K, which are depicted in Fig. 3.27, confirm the decrease of magnetic moment throughout the whole magnetic field range upon increasing hydrostatic pressure. The decreasing saturated moment is shown in Fig. 3.30. On the other hand the field positions of MT are almost unaffected by the pressure.

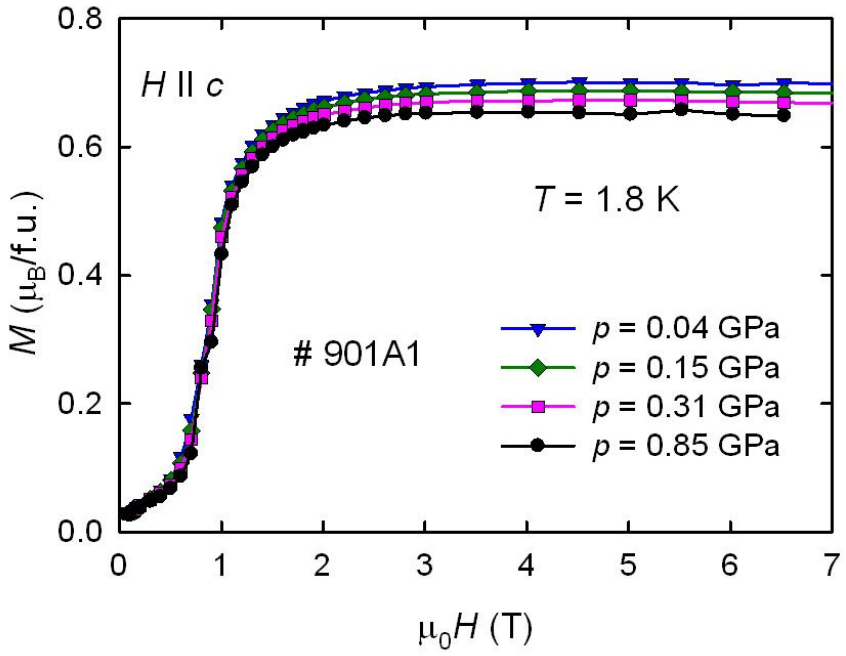

Fig. 3.27: Isothermal magnetization curves at 1.8 K along the *c*-axis of the sample #901A1 at various hydrostatic pressures.

In order to reach higher pressures, we had to use a different experimental technique, namely electrical resistivity measurements. In Fig. 3.28, we can see that the pressure further enhances the ordering temperatures marked by the vertical arrows on the electrical resistivity curves measured with current applied along the *c*-axis. The character of the anomaly is preserved up to the highest pressure 2.75 GPa, but the absolute values of electrical resistivity increase possibly due to worsening of the sample´s quality by pressure-induced cracks in the sample. The dependence of transition temperatures on pressure is shown in Fig. 3.30. The transition temperature position at 0.75 GPa has a bigger uncertainty due to lower number of measured experimental points of the $\rho(T)$ curve.

The longitudinal MR measured at 1.8 K is shown in Fig. 3.28. With increasing pressure the maximum gets broader, but its size is not affected. We may attribute this to an increasing separation between the two critical fields H_{m1} and H_{m2} of the MT, which is possible as well due to deteriorating quality of the sample with increasing pressure causing a distribution of MT critical fields.

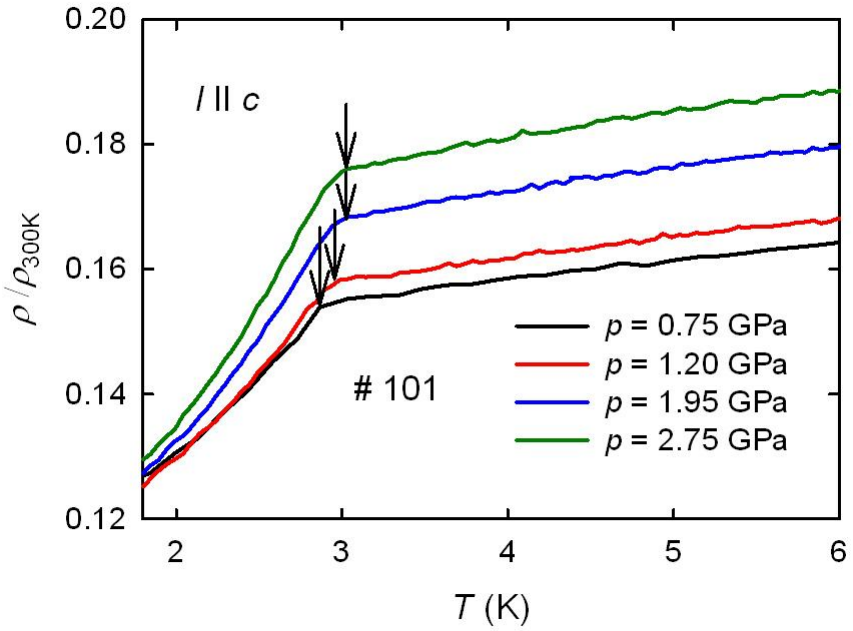

Fig. 3.28: Relative electrical resistivity of the single crystal #101 measured along the *c*-axis under different external hydrostatic pressures. The vertical arrows mark positions where $\partial^2\rho/\partial T^2$ has a maximum.

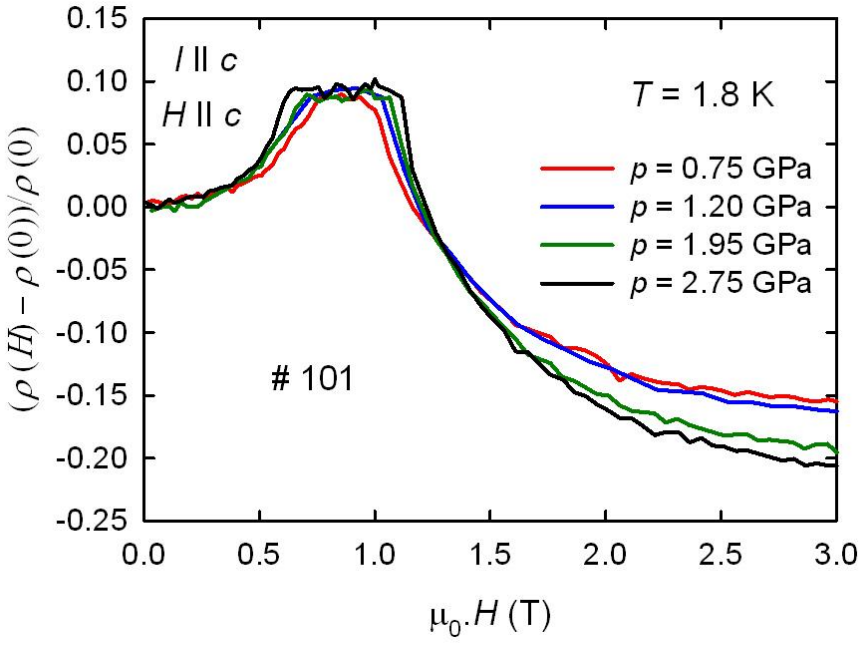

Fig. 3.29: Longitudinal magnetoresistance scans along the *c*-axis of the sample #101 taken at 1.8 K at various hydrostatic pressures.

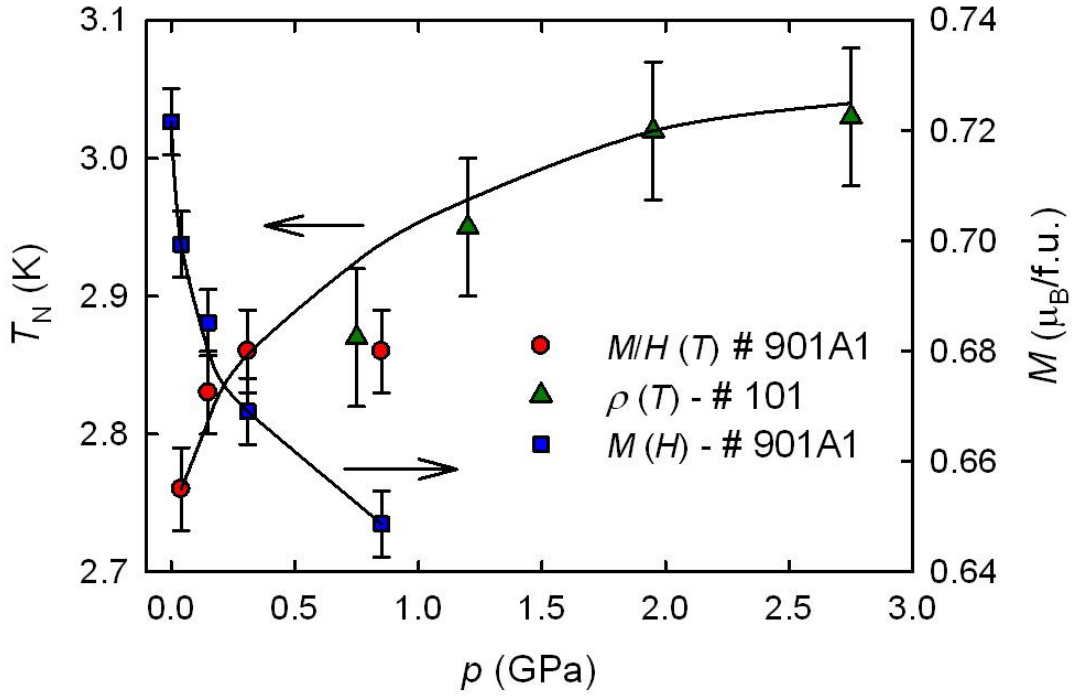

Fig. 3.30: Pressure dependences of (AFM) transition temperatures obtained from temperature scans of magnetization and electrical resistivity under hydrostatic pressure are tagged as M/H (T) and ρ(T), respectively. The evolution of saturated magnetization value at the field 7 T and at 1.8 K with pressure is labeled by M (H).

3.4.6. Discussion

Our measurements of magnetization, specific heat and electrical resistivity confirmed that CeRuSn orders antiferromagnetically below 2.8 K. The significant magnetocrystalline anisotropy, which is present in the paramagnetic state, namely a difference between the magnetic susceptibility measured along the main crystallographic axes (Figs. 4.10 and 4.11), persists down even into the magnetically ordered state. It is manifested in the anisotropic response of CeRuSn to application of magnetic field. Metamagnetic transitions found in fields applied along the *a*- and the *c*-axis are taken as an evidence for easy axes. The hard magnetization direction is oriented parallel to the *b*-axis. This result suggests that magnetic moments are entirely located in the *a*-*c* plane. The weak response of the isothermal magnetization

for field along the *b*-axis may be understood as an unwilling bending of magnetic moments out of the easy magnetization plane. On the other hand the MT can be viewed as spin-flip transitions from the antiparallel orientation of magnetic moments towards parallel oriented magnetic moments (spin-polarized state). The lower value of saturated magnetization in the case of the *a*-axis suggests that the metamagnetically induced phase has a preferential final orientation of magnetic moments somewhere out of the *a*-axis.

Our low field magnetization findings correlate with the microscopic data from both powder(62) and even recent single crystal neutron diffraction(49) studies, where the refined magnetic moments had components pointing along the *b*-axis. The latter also explains why we observe two metamagnetic transitions in the *a*-*c* plane. Two of three Cerium sites where reported to carry a magnetic moments below the Néel temperature. The moments are different, that is they vary between 0.11 and 0.95 μ_B when going along the *c*-axis. Thus the first MT would involve only one half of these moments, whereas second would include the remaining magnetic sites. But we have to emphasize the fact that the average moment reached only 0.61 μ_B in this study,(49) whereas we clearly observed in our bulk magnetization measurements saturated moments of 0.71 μ_B in the easy magnetization direction. That again brings questions about the quality of samples used in the single crystal neutron study.(49)

Specific heat measurements under the magnetic field reflect the anisotropy found in magnetization measurements. The anomalies move to lower temperatures when magnetic field is increasing while being still lower than the critical field of the MT. At higher fields a ferromagnetic-like response of the anomaly is seen. The position of the maximum in C_p/T increases with the magnetic field and its shape is typical for a "ferromagnetic" orientation of magnetic moments. The magnetic entropy determined from zero field measurements connected with the AFM transition reaches only ≈ 1/3Rln2, which suggests that only one third of Cerium sites contribute to the magnetic ordering in contradiction with the neutron experiments.(49) Alternatively we can interpret this low value of entropy also as a consequence of enhanced Kondo screening, although we do not have a direct support by e.g. observation of an increase of electrical resistivity at low temperatures. Thus it

is very difficult to justify how many Cerium sites are in the 3+ state and how many in an intermediate-valence state excluding appearance of a sizable magnetic moment.

The peaks in magnetoresistance emerging in magnetic fields approaching the first MT may be attributed to enhanced scattering of conduction electrons on spin-flip fluctuations tending to induce field-oriented metamagnetic states of magnetic moments on the local scale. When the second MT is reached, the spin-fluctuations cease. Above the MT the spins are flipped in a way that they are no more antiparallel with respect to the other magnetic sublattices. Thus the gaps in the Fermi surface arising due to different periodicity of the magnetic and crystal structure are closed.(22,23) This results in the huge drops in MR of 30 % and 20 % for the *a*- and *c*-axis. At the lowest temperature (0.5 K) these have the form of steps due to reduced thermal fluctuations. Taking into account similarity between the magnetization and electrical resistivity field scans (Fig. 3.31), we further expect that isothermal magnetizations at 0.5 K will also exhibit such sharp MT features. The agreement between anomalies in MR and isothermal magnetization measurements is shown in Fig. 3.31. For the *a*-axis and the 1.8 K curve we can see that the two maxima in $\partial M/\partial H$ are located at roughly the same fields as peaks in the $\partial\rho/\partial H$ curve being $\mu_0 H_{m1}{}^{a} = 0.85$ T and $\mu_0 H_{m2}{}^{a} = 1.45$ T. The MT at 2.7 K also well coincides with the local minimum in $\partial\rho/\partial H$ curve. For the *c*-axis we can trace up the correspondence at 1.8 K for the first MT only at $\mu_0 H_{m1}{}^{c} = 0.56$ T. The second MT in the $\partial M/\partial H$ curve occurs in lower fields ($\mu_0 H_{m2}{}^{c} = 0.80$ T) than the minimum in the $\partial\rho/\partial H$ dependence. We may interpret this discrepancy by the fact that magnetoresistance probes a physical property that is more dependent on the overall quality and shape of measured sample. If we assign the second MT to the point where MR approximately starts to decrease, since the antiferromagnetic coupling is about to be completely destroyed, we arrive to a better agreement between the MR and the magnetization data, especially in the case of the *c*-axis.

Based on the data from magnetization, specific heat and electrical resistivity measurements, we constructed the *H*-*T* phase diagrams depicted in Fig. 3.32. We may identify four different magnetic phases in CeRuSn. The first is an AFI structure located at low fields and below 2.8 K. At higher temperatures CeRuSn undergoes a transition into a paramagnetic phase (PM). Applying the magnetic field induces

a magnetic structure change. This restructured phase is denoted as AFII for H II a and AFIII for H II c, because they are likely different. In addition we observed an induced spin-polarized phase (IFM), which occurs at high fields below the ordering temperature.

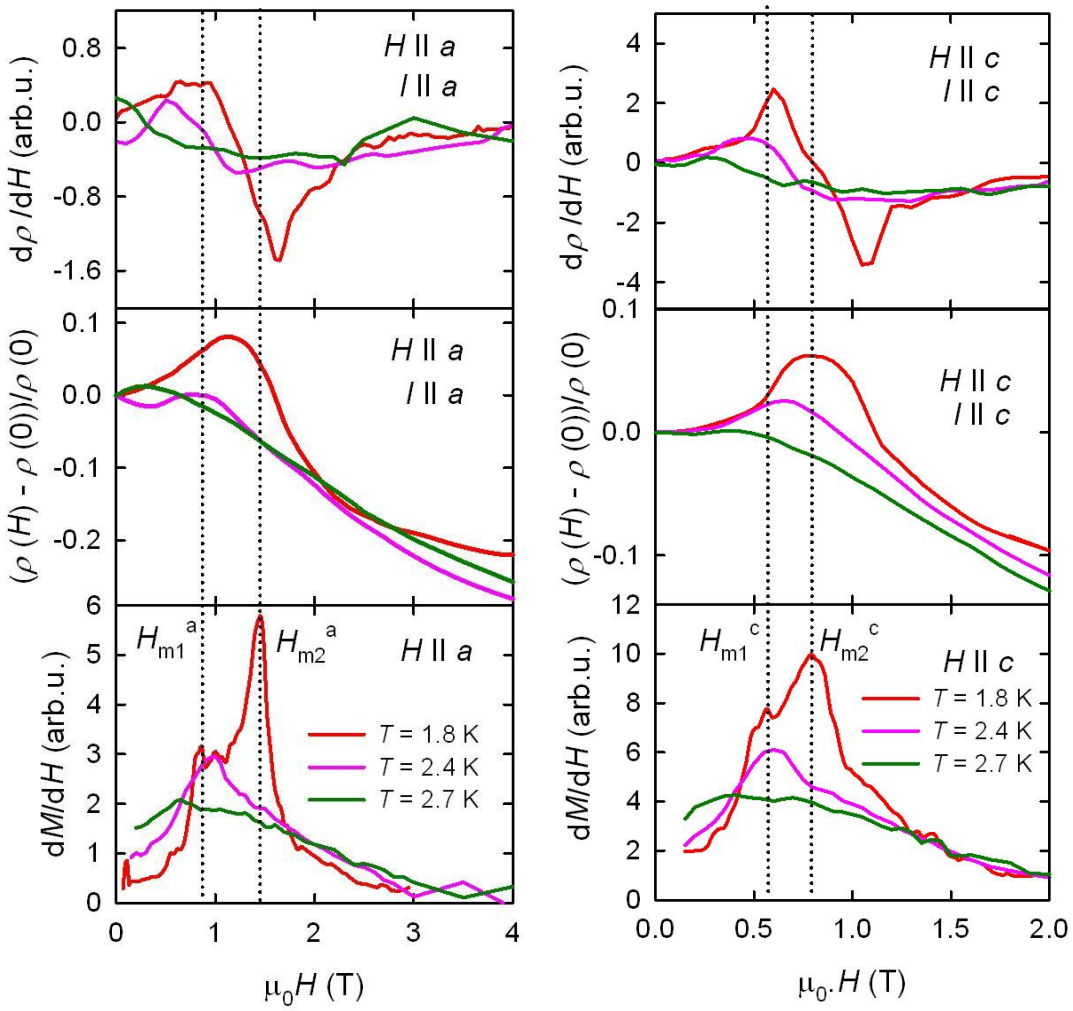

Fig. 3.31: Comparisons of magnetic field derivatives of magnetoresistances and isothermal magnetizations along the a- and c-axis. Additionally a field scan of specific heat along c-axis is shown. The vertical dotted lines represent positions of metamagnetic transitions in isothermal magnetization curves.

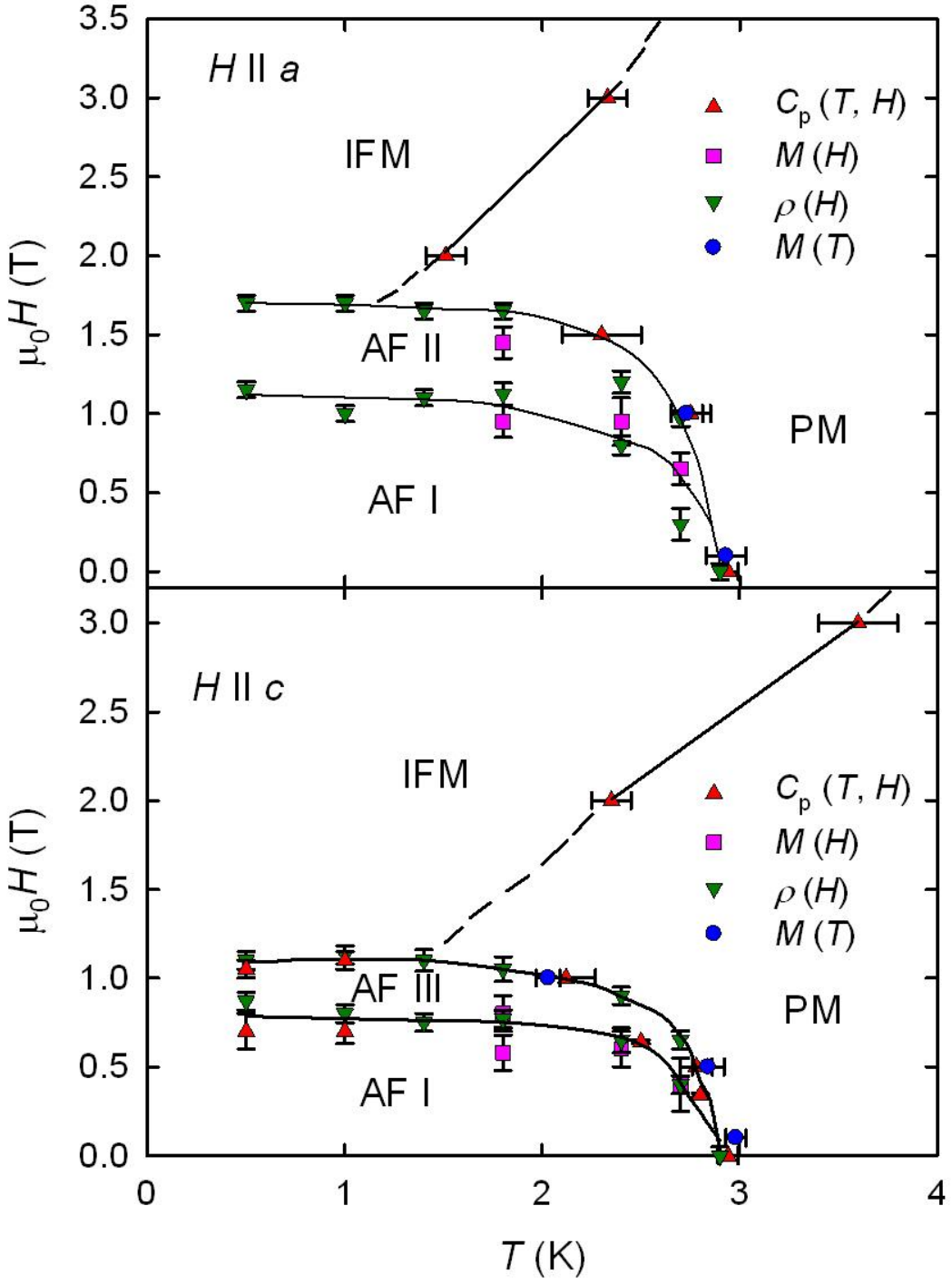

Fig. 3.32: Field-temperature diagrams overviewing magnetic phases below 4 K when magnetic field is applied along the *a*- and *c*-axis. Anomalies in specific heat, magnetoresistances, and temperature scans of magnetization are denoted as C_p (*T*, *H*), ρ (*H*), and *M* (*T*), respectively. Metamagnetic transitions from isothermal magnetizations are labeled *M* (*H*).

In overall hydrostatic pressure in overall shifts the Néel temperature towards higher values, contrary to a suppression of the saturated magnetic moment along the *c*-axis. This is documented in Fig. 3.30. Such behavior is very unusual and can be only interpreted considering rather anisotropic response of CeRuSn to the hydrostatic pressure. Since the structure is quite complex, we can expect that compressibility along different directions is highly anisotropic. That would bring a large difference in change of hybridization strength along different directions. Such scenario may be accompanied by simultaneously strengthening of the ordered state due to further localization (long bounds) and an enhancement of screening of some localized moments (preferably in the easy directions) by conduction electrons as a result of shorting particular Ce-Ru distances.

4. $YbPt_2Si_2$

The RPt_2Si_2 compounds mostly crystallize in the body centered $ThCr_2Si_2$-type crystal structure. It was reported that the 4d-site, which is the Pt-position becomes randomly populated by Si-ions. Vice versa Pt occurs on the Si-4f-site. This interchange of ions leads to a strong disorder.(65) A later study revealed a presence of superstructure peaks, which suggest that the compounds may crystallize in the primitive tetragonal structure of the $CeBe_2Ge_2$-type,(66) which is closely related to the $ThCr_2Si_2$ structure.

In addition only little information was known about physical properties of $YbPt_2Si_2$ from measurements of polycrystalline samples.(67,68) These facts motivated us to synthesize $YbPt_2Si_2$ in single crystalline form by flux growth method and measure its physical properties.

4.1. Preparation by solvent growth method

The preparation of intermetallic compounds containing Ytterbium is quite complicated due to Ytterbium high vapor pressure and a very narrow temperature interval of its liquid phase. The obstacles during single crystal growth limited the number of studies performed on high quality single crystals in the past. But employing the solvent growth method eliminates several of these complications.

The single crystals were prepared by the solvent growth method with Tin flux. Non-stoichiometric amounts of starting pure elements (Yb - 99.9 %, Pt - 99.95 %, Si - 99.9999 % and Sn - 99.9999%) were placed into alumina crucibles as listed in Table 4.1 and sealed inside quartz glass tubes filled by 0.25 Bar of a pure Argon atmosphere. The ampoules were then placed into a high-temperature oven and heated up to 1450 K. After very slow cooling by 0.1 K/min to 970 K, the cooling rate was increased to 1 K/min down to 570 K where the ampoules were centrifuged in order to separate the liquid flux from the grown single crystals. The remaining flux was removed from single crystals surface by a solution of hydrochloric acid.

The first attempts to synthesize $YbPt_2Si_2$ using the ratio of Yb:Pt:Si being 1:2:2 led to growth of a completely novel compound $Yb_2Pt_3Si_5$, which will be subject of the next Chapter.

Using a naive picture considering the binary phase diagrams between Yb, Pt, Si and Sn, we chose a different stoichiometry in order to synthesize $YbPt_2Si_2$ single crystals. The next two growths with an increased Pt and reduced Si content were successful and brought $YbPt_2Si_2$ single crystals prepared for the very first time by solvent growth method. During their characterization it was found that they contained a small amount (5 %) of $Yb_2Pt_3Si_5$ as a spurious phase. After next two unsuccessful attempts to evade this phase, we increased the starting amount of Pt considerably. It turned out that by this, batches PS9 and PS10 were almost free of the $Yb_2Pt_3Si_5$ impurity phase.

The samples from growths PS1 and PS2 contained a non-negligible amount of YbAs in their bottom parts most probably originating from contamination of alumina crucibles. Another two growths PS7 and PS8 repeated the original growth processes (PS1 and PS2) in order to obtain phase pure single crystals of $Yb_2Pt_3Si_5$.

Table 4.1: Solvent method growth conditions during preparation of YbPt2Si2.

Growth	Flux ratio	Mass of elements (g)	Starting stoich.	Result	*RRR* = ($\rho_{max\ T}/\rho_{min\ T}$)
PS1	0.9	0.36	1.0:2:2	SC - $Yb_2Pt_3Si_5$	
PS2	0.95	0.22	1.0:2:2	SC - $Yb_2Pt_3Si_5$	20 (300/4)
PS3	0.95	0.26	1:2.7:1.6	SC - $YbPt_2S_2$*	
PS4	0.95	0.23	1.2:2.7:1.6	SC - $YbPt_2S_2$*	
PS5	0.95	0.26	1:3:1.6	SC - $YbPt_2S_2$*	
PS6	0.95	0.23	1:2.7:1.3	SC - $YbPt_2S_2$*	
PS7	0.9	0.36	1.0:2:2	SC - $Yb_2Pt_3Si_5$	
PS8	0.95	0.22	1.0:2:2	SC - $Yb_2Pt_3Si_5$	
PS9	0.95	0.25	1.0:3.1:1.4	SC - $YbPt_2S_2$*	
PS10	0.95	0.24	1.1:3.1:1.4	SC - $YbPt_2S_2$*	

*with a small amount of $Yb_2Pt_3Si_5$ inclusions

4.2. Characterization

Since our biggest problem was to get the correct stoichiometry and phase purity of our samples, we at first measured EDX after preparation of single crystals in order to inspect their composition. In Fig. 4.1 a view by electron microscope on the polished surface of a single crystal from batch #PS4 is shown. Table 4.2 summarizes the EDX results. No. 2 phase, the main one, had roughly the correct desired stoichiometry. Small inclusions of the $Yb_2Pt_3Si_5$ compound are present; it is labeled by No. 1.

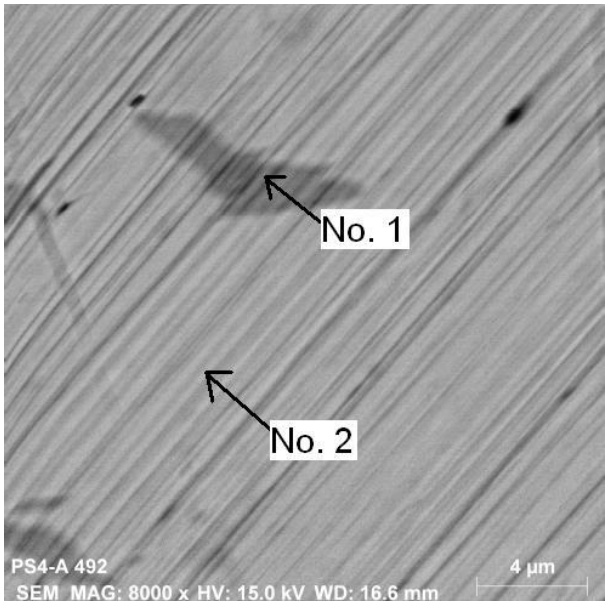

Fig. 4.1: A snapshot of the polished surface of a single crystal grown in batch #PS4. The labels denote points, at which EDX spectra were collected. These are listed in Table 4.2.

Table 4.2: Atomic fractions according to EDX spectra taken at points shown in Fig. 4.1. The correct atomic fractions for $YbPt_2Si_2$ and for $Yb_2Pt_3Si_5$ are 20:40:40 and 20:30:50, respectively.

point No.	At. fraction Yb (%)	At. fraction Pt (%)	At. fraction Si (%)
1	19(1)	29(1)	52(1)
2	19(2)	37(3)	44(2)

A powder X-ray diffraction pattern of $YbPt_2Si_2$ is displayed in Fig 4.2. Two impurity peaks marked by arrows in Fig. 4.2 at 29.5° and 31.5° belong to Yb_2O_3 and Yb_3O_4, respectively. The latter has approximately three times bigger intensity. But these reflections are the strongest for both compounds, so, taking the integral value under the peaks as a measure, the overall contamination should not exceed 1 %. According to the Rietveld refinement we obtained lattice parameters a = 4.0959(2) Å and c = 9.9840(4) Å in good agreement with the reported values.(67,68) The peak at 15° originates from the impurity phase $Yb_2Pt_3Si_5$, which remains present in our samples even after the starting stoichiometry has been changed. But its size is significantly smaller than the reflection of the main phase.

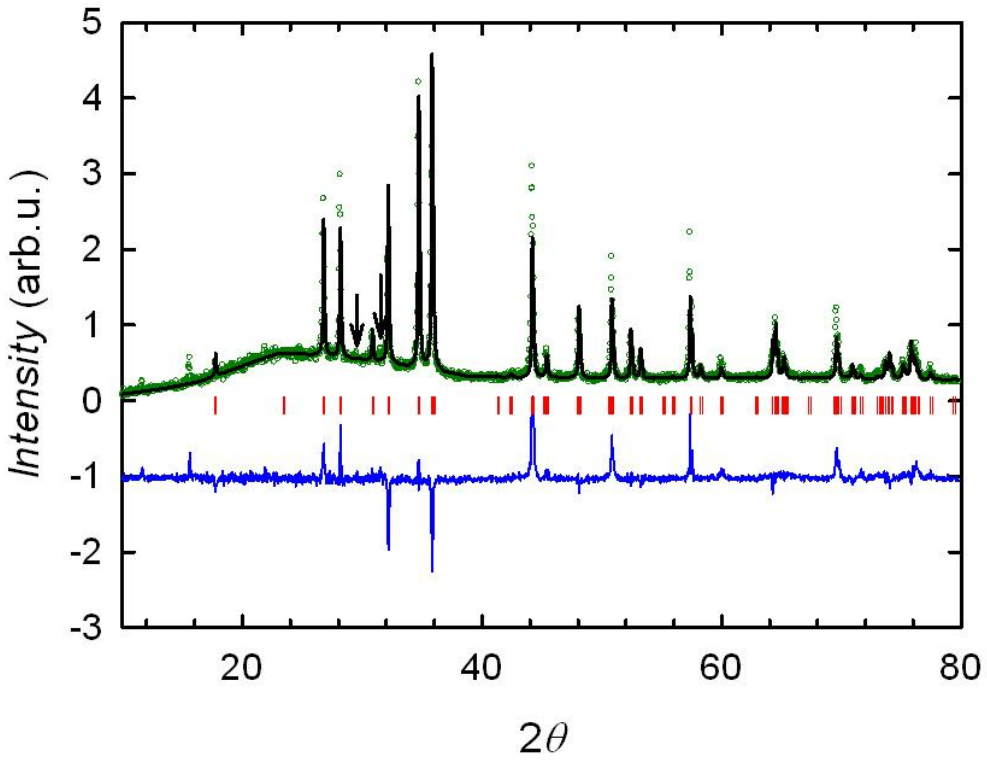

Fig. 4.2: The X-ray diffraction pattern collected on a few crushed single crystals from batch #PS10 (green circles) fitted by the Rietveld method (black line). The difference between measured points and fitted ones is given by the blue line. The red vertical strokes signify Bragg positions.

4.3. Physical properties

Physical properties were mostly studied on the sample #PS10A, which had the highest *RRR* ratio from all inspected samples through different batches. If the data are collected on a different single crystal, it will be explicitly mentioned and labeled in the plot.

4.3.1. Magnetic susceptibility

The magnetic susceptibility measured between 1.8 and 400 K exhibits a significant anisotropy. In addition, a broad maximum is located at around 130 K (280 K) in the field applied along the *c*-axis (*a*-axis). This is usually found in systems containing Yb^{2+} and the maximum arises due to gradual population of the excited Yb^{3+} configuration.(69) At sufficiently high temperatures, the susceptibility can be fitted by an equation alike to Curie-Weiss law, where the paramagnetic Curie temperature is replaced by spin-fluctuation temperature T_{sf}. Well above this temperature the mean occupation of these two configurations is dominated by thermal fluctuation, whereas sufficiently below it is controlled by quantum fluctuations. Another parameter is the energy E_{ex}, which equals to the difference between these two configurations. However, our data allowed an estimation of T_{sf} only yielding 108(5) K and 80(5) K for the *a*- and the *c*-axis, respectively. The magnetization has higher values in the *c*-axis direction in accordance with low-temperature isothermal magnetization curves depicted in Fig. 4.4. The magnetic moments are only tiny, reaching the values of 0.01 μ_B and 0.04 μ_B in a field of 7 T for the *a*- and *c*-axis, respectively.

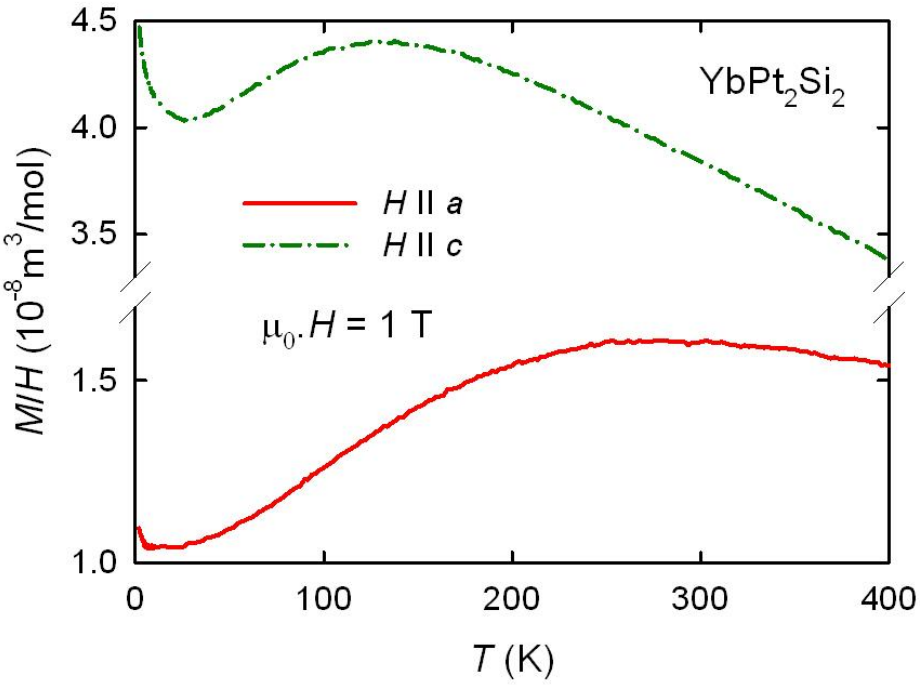

Fig. 4.3: Temperature dependences of magnetic susceptibility *M*/*H* along main crystallographic axes at 1 T field. Mind the brake in the *y*-axis.

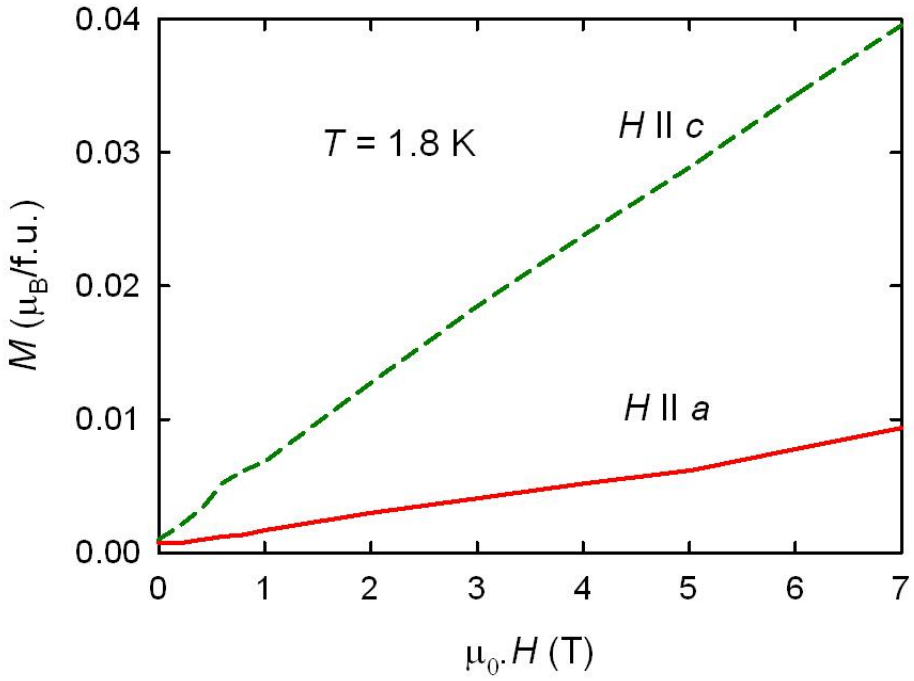

Fig. 4.4: Isothermal magnetization determined at 1.8 K in the field applied along the *a*- and the *c*-axis, respectively.

At low temperatures an upturn is observable in low magnetic fields (0.1 T), which is easily suppressed by a higher magnetic field hinting at a magnetic impurity as origin. In the 7 T field a temperature independent Pauli paramagnetic susceptibility is restored.

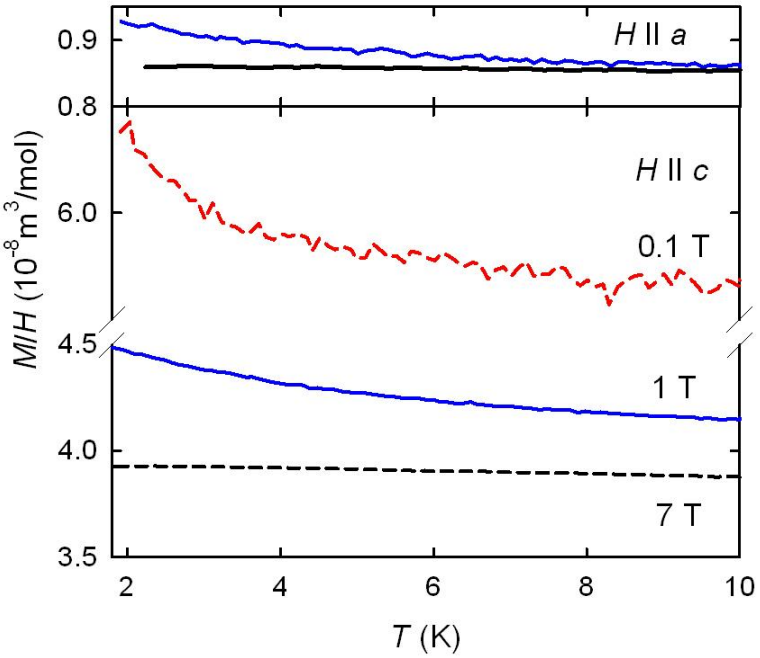

Fig. 4.5: temperature scans of magnetic susceptibility below 10 K along main crystallographic directions. at various magnetic fields.

4.3.2. Specific heat

The temperature dependence specific heat divided by temperature is depicted in Fig. 4.6. Below 1 K we can observe a weak upturn, which may be an indication of magnetic ordering occurring below 0.5 K. The inset of Fig. 4.6 shows a fitting of the specific heat to eq. (7). According to this, the gamma coefficient of specific heat reaches 26.9(2) $mJ.mol^{-1}.K^{-2}$.

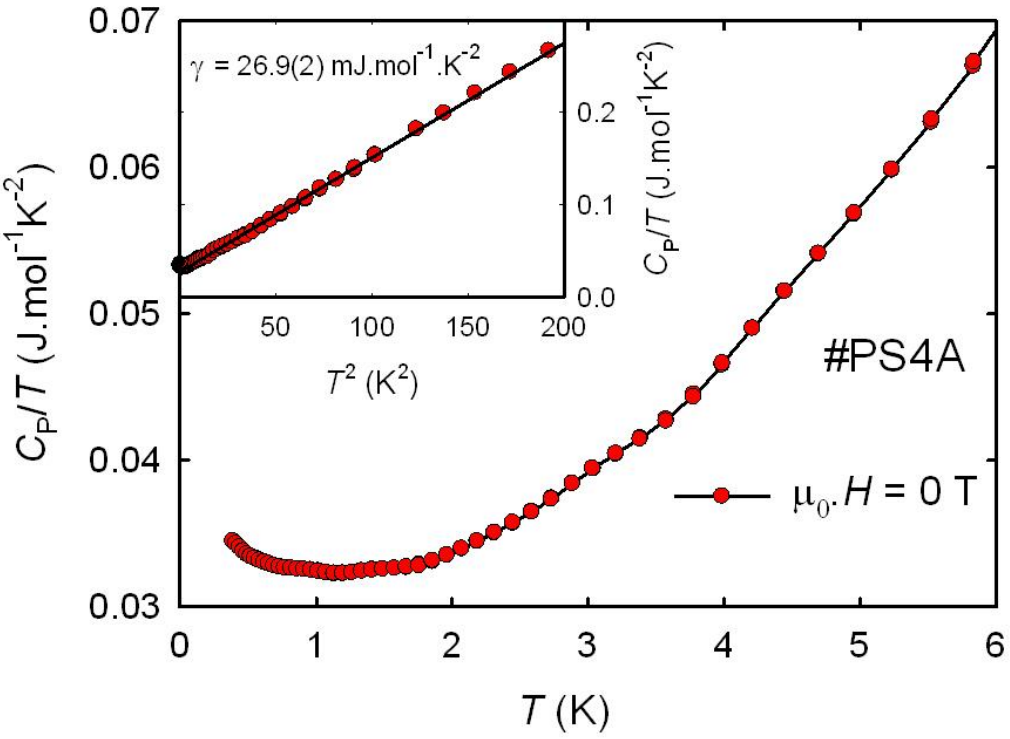

Fig. 4.6: Specific heat divided by temperature vs. temperature at various magnetic fields applied along *c*-axis of the sample #PS4A. The inset shows fitting of specific heat to eq. (7).

4.3.3. Electrical resistivity

The electrical resistivity does not exhibit any anomaly from 300 K down to 0.5 K where it stays constant as can be expected for an ordinary metal, see Fig. 4.7. The low-temperature (< 50 K) resistivity data can be fitted to the equation derived from the classical Landau-Fermi liquid description $\rho = \rho_0 + aT^2$, see inset in Fig 5.7. For current along the *a*-axis we obtained $a = 2.59(2).10^{-5}$ K^{-2} and $2.46(2).10^{-5}$ K^{-2} for #PS10A and #PS10B sample, respectively. Including the term describing phonons, which is proportional to T^5, we can fit the data up to 80 K with $a = 2.66(2).10^{-5}$ K^{-2} and $2.53(2).10^{-5}$ K^{-2} for #PS10A and #PS10B sample, respectively. On other hand the data for the *c*-axis of the sample #PS10A can be fitted up to 40 K and 60 K (with phonons) yielding $a = 2.54(4).10^{-5}$ K^{-2} and

2.94(4).10^{-5} K^{-2}, respectively. The coefficients of the T^5-term reach negative values ≈ 10^{-11} K^{-5}.

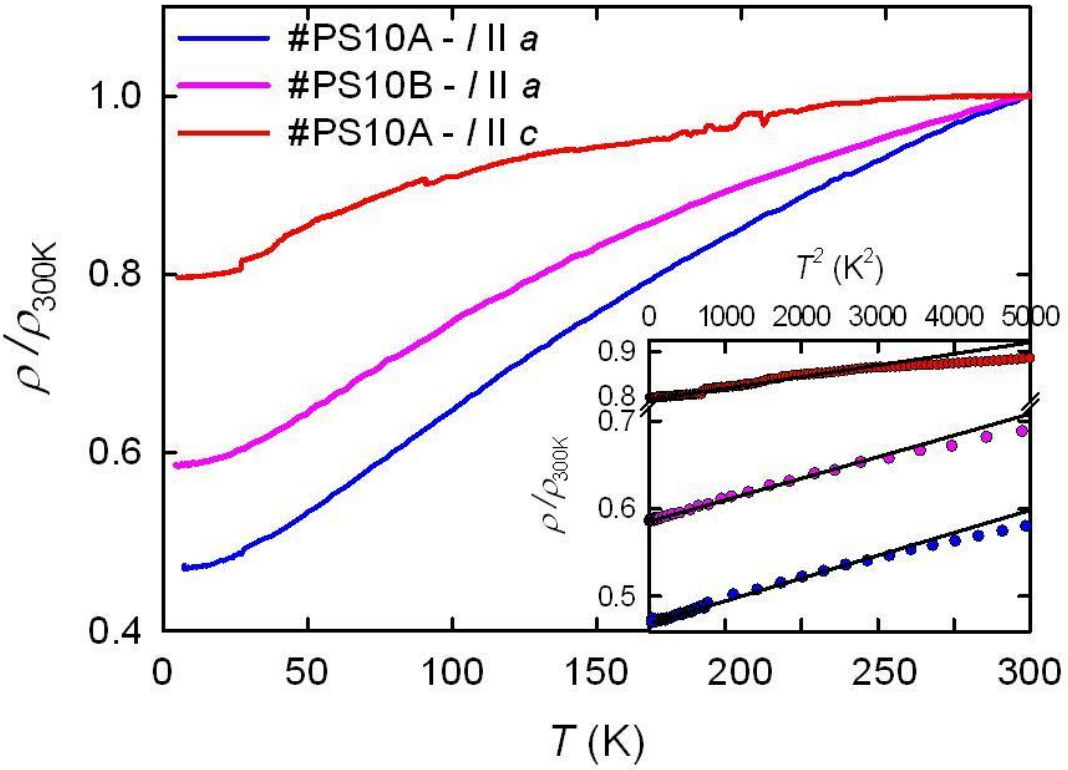

Fig. 4.7: The temperature dependences of electrical resistivity along main crystallographic axes of two samples from batch #PS10 normalized to room temperature

4.3.4. Electrical resistivity under high pressure

We applied high pressure during electrical resistivity measurements in order to probe $YbPt_2Si_2$ for possibly emerging magnetic ordering, found in some Yb-based intermetallics due to pressure induced valence change. Results of our measurements are displayed in Fig. 4.7. The data below 6 K are temperature dependent and a very slight decrease occurs below approximately 3.5 K. Since this feature is easily removed by 0.5 T magnetic field applied in the same direction as current, we attribute it to a small amount of Tin inclusion inside the sample. Tin is

superconducting below 3.7 K and already field of 0.25 T suppress the transition below our experimental limit (1.8 K).(70)

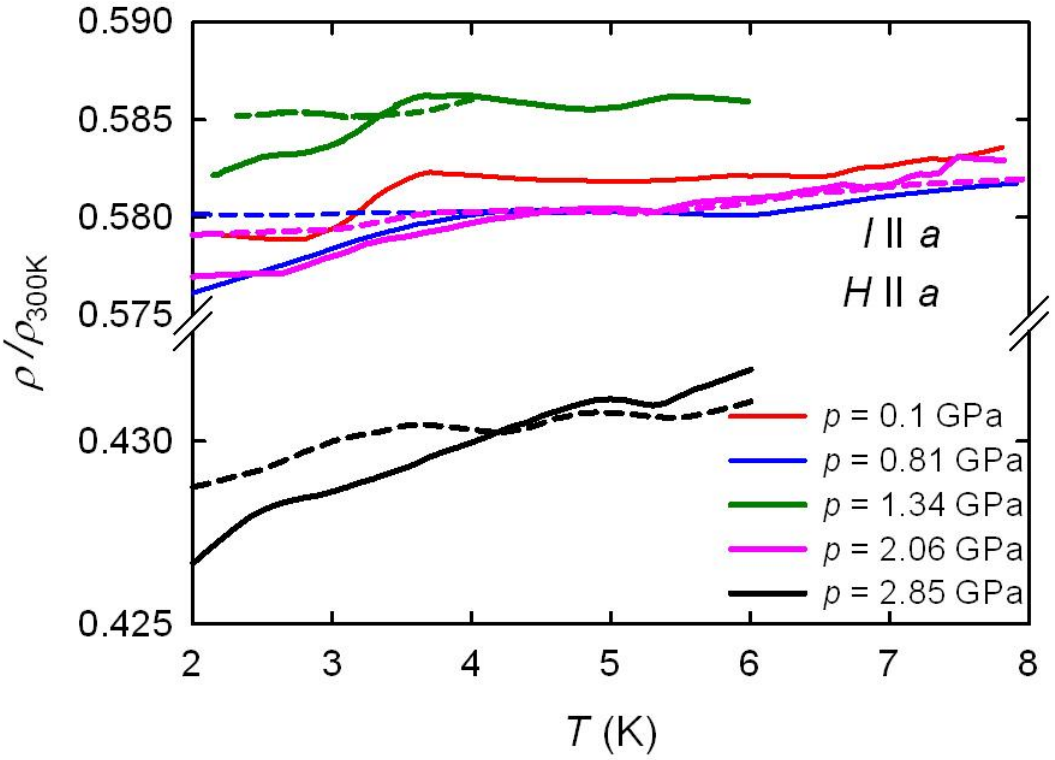

Fig. 4.8: Electrical resistivity of $YbPt_2Si_2$ along *a*-axis of the sample #PS10A under various hydrostatic pressures. The full lines represent zero field data, whereas the dashed ones show data measured in 0.5 T field applied along *c*-axis.

4.3.5. Theoretical calculations

In order to explain the anomalous behavior of magnetic susceptibility, we performed *ab-initio* calculations in the framework of density functional theory based on local-spin-density approximation of exchange correlation energy.(71) Kohn-Sham equations were solved by Full-potential Augmented-plane-waves plus local-orbitals method, which is included in the code of the WIEN2k program.(72)

A comparison between the calculated and experimentally determined dependences of *H*/*M* at 1 T field is shown in Fig. 4.9. We can see that the calculated

data are far from the theoretical ones, although the estimation of the anisotropy is correct.

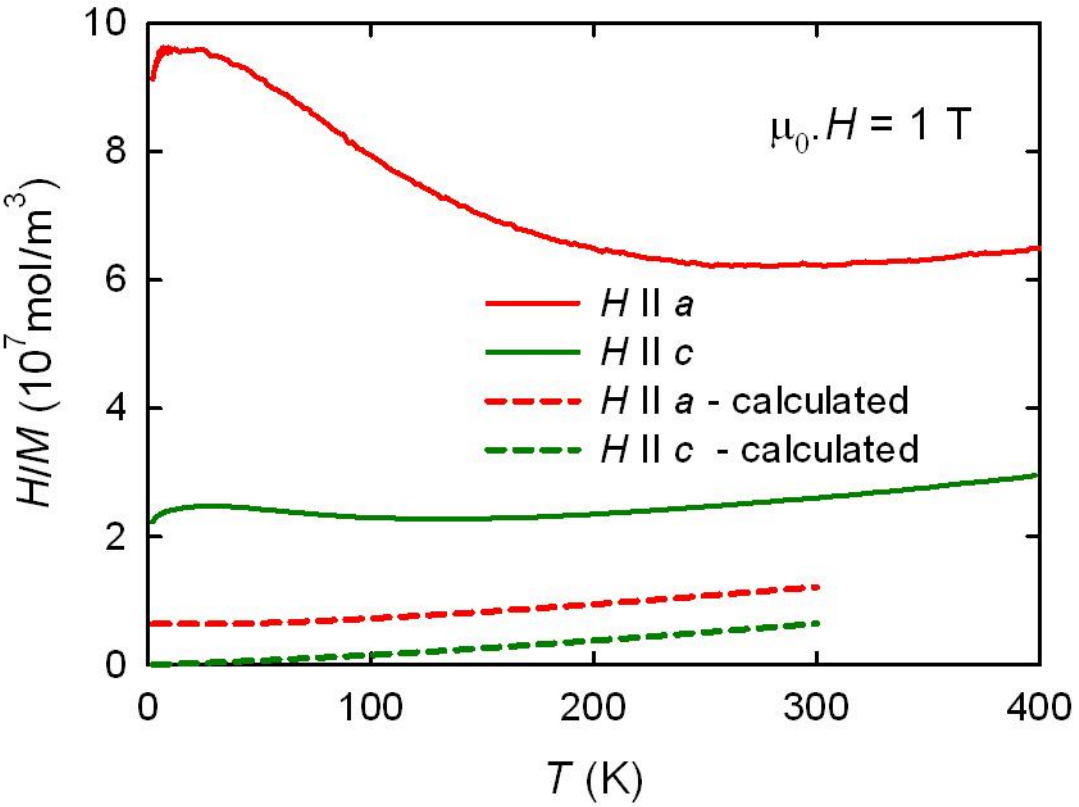

Fig. 4.9: A comparison between experimentally (full lines) and theoretically (dashed lines) calculated *H*/*M* dependences.

4.4. Discussion

Our measurements revealed no magnetic ordering in down to 0.5 K. The maximum observable in the temperature dependences of magnetic susceptibility reminiscences valence fluctuating systems. We expect that at higher temperatures, an admixture of Yb^{3+} states arise in the compound due to a gradual thermal population, which are at low temperatures separated from the ground state by E_{ex}. That would also explain the restoration of Curie-Weiss like behavior of magnetic susceptibility at high temperature above the observed maxima as well as magnetic anisotropy in the whole temperature range. At low temperatures we expect that a small amount of either magnetic Yb^{3+} ions or of magnetic impurity reside in

the lattice, which manifest in the increase of magnetic susceptibility below 10 K. The suppression of this feature by higher magnetic fields (> 1 T) proposes that the latter scenario is more favorable.

Our pressure experiment revealed that $YbPt_2Si_2$ most probably lies far on the left from the first QCP or on the right from the second QCP. Since we did not observe any magnetic transition neither in the highest pressure, we expect that the low temperature anomaly in specific heat was not connected with any magnetic ordering, because in this case, two situations would have taken place: (1) $YbPt_2Si_2$ is situated on the right side of the 1^{st} QCP. The magnetic order is supported by increasing pressure resulting in an enhancement of the transition temperature and its observation in the available experimental limit. (2) $YbPt_2Si_2$ is on the left side of the 2^{nd} QCP and the magnetic ordering is suppressed by the applied pressure to zero temperature. In this case the electrical resistivity would exhibit an unusual temperature scaling, e.g. $\rho \sim T$.

The disagreement between theoretical calculations of magnetic susceptibility and the measured data may come from the fact that Yb^{3+} is expected to lie lower in energy than in fact is located. That would increase the theoretically expected values of magnetization. Nevertheless the qualitative agreement coming from the correct prediction of the easy and hard magnetization directions shows at least partially appropriate approach used in the theoretical calculations.

5. $Yb_2Pt_3Si_5$

The $Yb_2Pt_3Si_5$ is a completely new compound, which was for the first time prepared during our studies when attempting to grow $YbPt_2Si_2$ from Tin flux. Our single-crystals prove to be of high-quality (according to *RRR* values), although a small amount of Tin inclusions was revealed inside the samples. In this chapter we will present the first measurements of the physical properties of this new compound.

5.1. Characterization

The preparation of $Yb_2Pt_3Si_5$ single crystals is discussed in the section 5.1. Since it is a completely new compound, the crystal structure was characterized by single crystal X-ray diffraction employing a Rigaku diffractometer. From this we found that it crystallizes in the orthorhombic $U_2Co_3Si_5$-type structure (space group Ibam) with the lattice parameters: a = 10.005 Å, b = 11.334 Å, c = 5.952 Å. The single crystal composition was then inspected by EDX measurements (Fig. 5.1). Beside the main phase $Yb_2Pt_3Si_5$ (No. 1 in Fig. 5.1), we discovered small areas with Tin inclusions inside the crystal (No. 2), which cover the area of approximately 2 % of the whole measured surface.

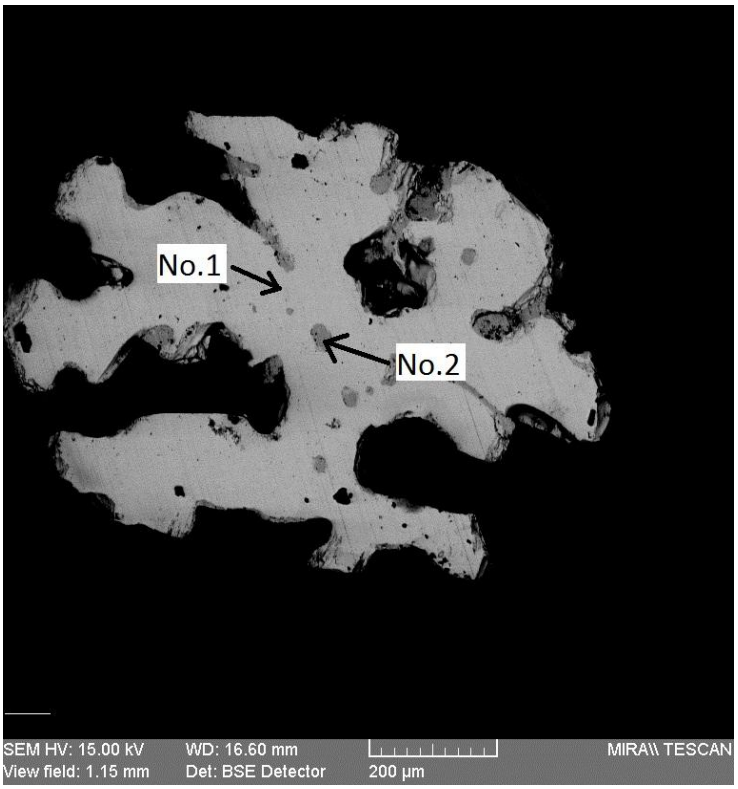

Fig. 5.1: A view made by an electron microscope via a back-scattered electrons detector on the polished surface of the single crystal #PS7A1 after cutting, which was done in order to separate the #PS7A2 sample. The labels denote points, at which EDX spectra were collected. These are listed in Table 5.1.

Table 5.1: Atomic fractions according to the EDX spectra taken at points shown in Fig. 5.1. The correct ratio for the $Yb_2Pt_3Si_5$ is 20:30:50 (Yb:Pt:Si).

point No.	At. fraction Yb (%)	At. fraction Pt (%)	At. fraction Si (%)	At. fraction Sn (%)
1	22(1)	29(2)	49(1)	
2	11(2)	2(3)	2(2)	85(3)

5.2. Physical properties

Most of physical properties were measured on the sample A1 from batch #PS7, which has the *RRR* ~ 90 (along the *c*-axis) at the beginning of our study. If the data are collected on a different single crystal, it is explicitly mentioned in the text and labeled in the plot.

5.2.1. Magnetic susceptibility

Like in the case of $YbPt_2Si_2$, we may trace up a tendency of magnetic susceptibility to reach a maximum above 350 K, see Fig. 5.2. The high-temperature data (not shown) reveal that it occurs at 450(5), 500(5) and 440(5) K in the case of the *a*-, *b*- and *c*-axis, respectively. The magnetic susceptibility measured between 1.8 and 350 K is anisotropic, although the *a*- and *b*-axis dependences are very close to each other. Here we also expect that the local maxima above room temperature are caused by gradual population of the magnetic Yb^{3+} state located at low temperatures above the non-magnetic Yb^{2+} one.(69) At high temperatures (> 750 K) the susceptibilities can be fitted to the equation alike to Curie-Weiss law similarly to the situation in $YbPt_2Si_2$. The spin fluctuation temperature T_{sf} reaches the values of 476(10) K (the *a*-axis), 1414(30) K (the *b*-axis) and 455(9) K (the *c*-axis).

The high-temperature anisotropy of magnetic susceptibility is reflected also at the lowest measured temperatures (< 10 K). An upturn is observable in low magnetic fields (0.1 T), which is easily suppressed by magnetic field, see Fig. 5.3. Again, similarly to $YbPt_2Si_2$, at 7 T field the temperature independent Pauli paramagnetic susceptibility is observable.

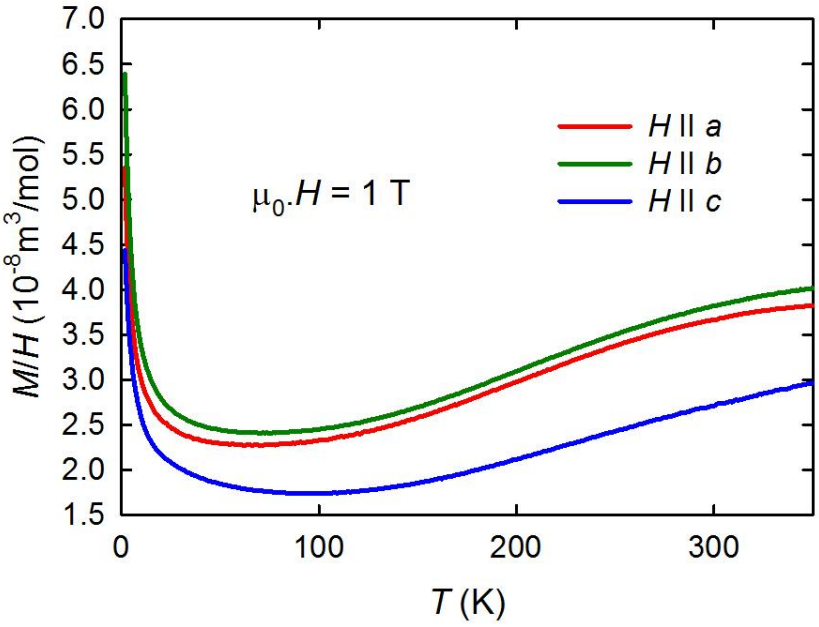

Fig. 5.2: Temperature dependences of magnetic susceptibility *M*/*H* measured along main crystallographic axes at 1 T field.

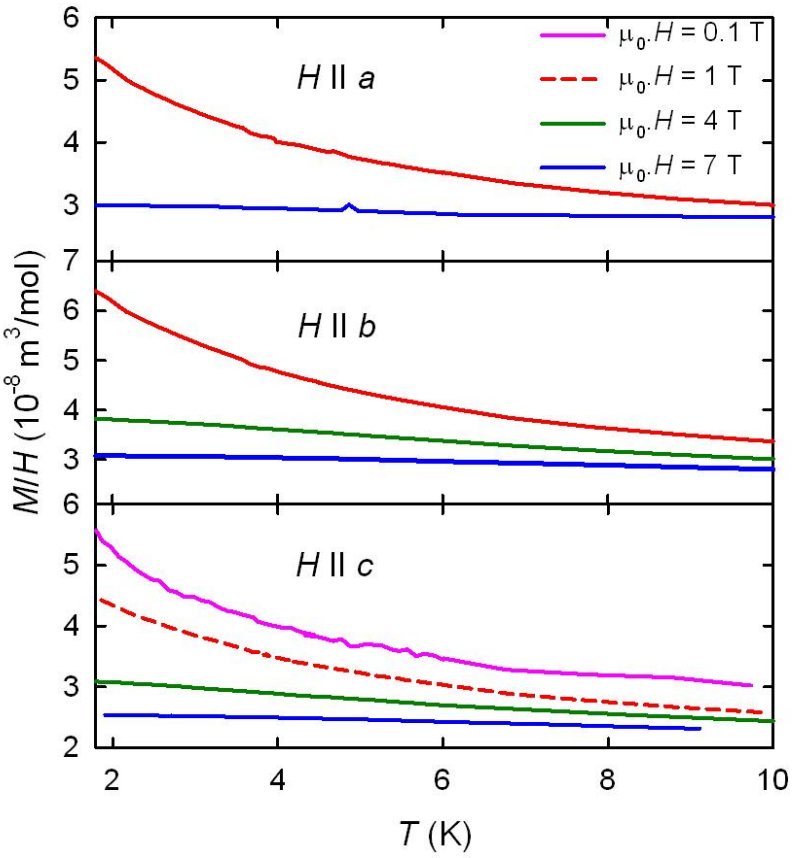

Fig. 5.3: Temperature scans of magnetic susceptibility *M*/*H* below along main principal directions below 10 K measured at various fields.

The isothermal magnetization dependences taken at 1.8 K, which are shown in Fig. 5.4, confirm the anisotropy observed in the temperature scans of magnetic susceptibility. Magnetic moments at 7 T reach only very low values of 0.030 μ_B, 0.031 μ_B and 0.026 μ_B along the *a*-, *b*- and *c*-axis, respectively.

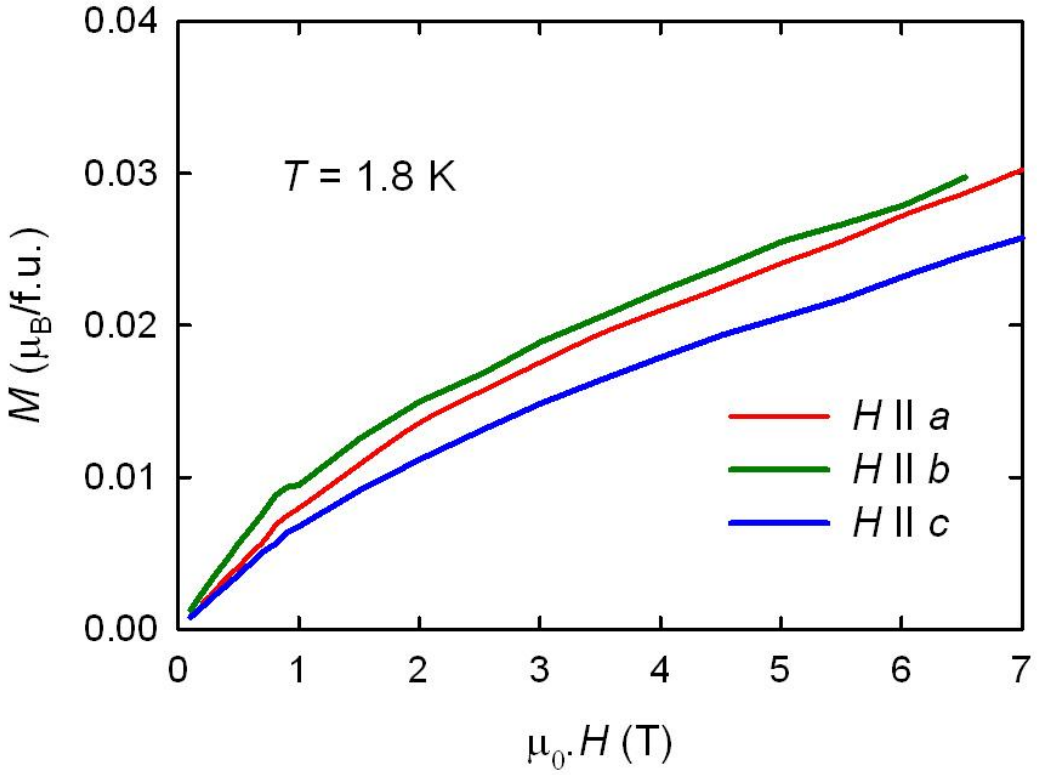

Fig. 5.4: Isothermal magnetization determined along main crystallographic axes at 1.8 K.

5.2.2. Specific heat

In Fig. 5.5 we can see the temperature dependence of specific heat divided by temperature between 2 and 20 K. The inset of Fig. 5.5 shows a fitting of the specific heat to eq. (7). According to this, the gamma coefficient of specific heat reaches 34.5(5) $mJ.mol^{-1}.K^{-2}$. We measured the data up to 300 K with no sign of any

transition. An analysis of the data to eventual Schottky magnetic contribution arising from the gradual population of the magnetic Yb^{3+} state was not possible due to absence of a non-magnetic analog compound (e.g. $Lu_2Pt_3Si_5$).

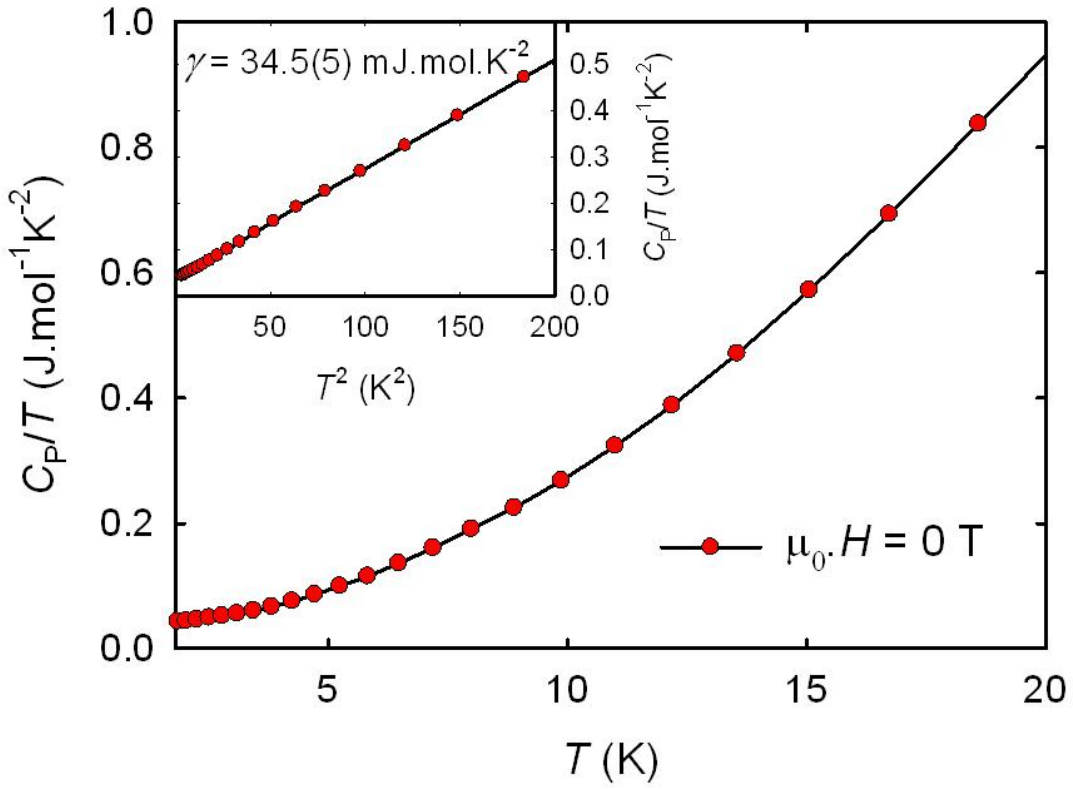

Fig. 5.5: Specific heat divided by temperature at zero field. The inset shows a fitting of the specific heat to eq. (7).

5.2.3. Electrical resistivity

The electrical resistivity of $Yb_2Pt_3Si_5$ measured on the sample #PS7A1 and on a piece cut from it (#PS7A2) exhibits no anomaly from 300 K down to 0.5 K, as can be seen in Fig. 5.6. Below 60 K the curves can be fitted to the equation: $\rho = \rho_0 + aT^2$. For the *a*-, *b*- and *c*-axis we obtained a =2.52(2).10^{-5} K^{-2}, 2.48(1).10^{-5} K^{-2} and 2.61(1).10^{-5} K^{-2}, respectively. Like in the case of $YbPt_2Si_2$, including the additional term for the phonon contribution, which is proportional to T^5, we were able to fit the data up to 100 K. The coefficients of these terms ranged

from -4.8 to -6.10^{-12} K^{-5}. The *RRR* ratios reach 59 and 82 in the case of the *a*- and *c*-axis, respectively. The high values prove very good quality of our sample. The much smaller *RRR* for the *b*-axis is caused by the fact that this measurement was performed after the pressure experiment discussed in the next section, during which the sample quality apparently deteriorated by the acting of high pressure.

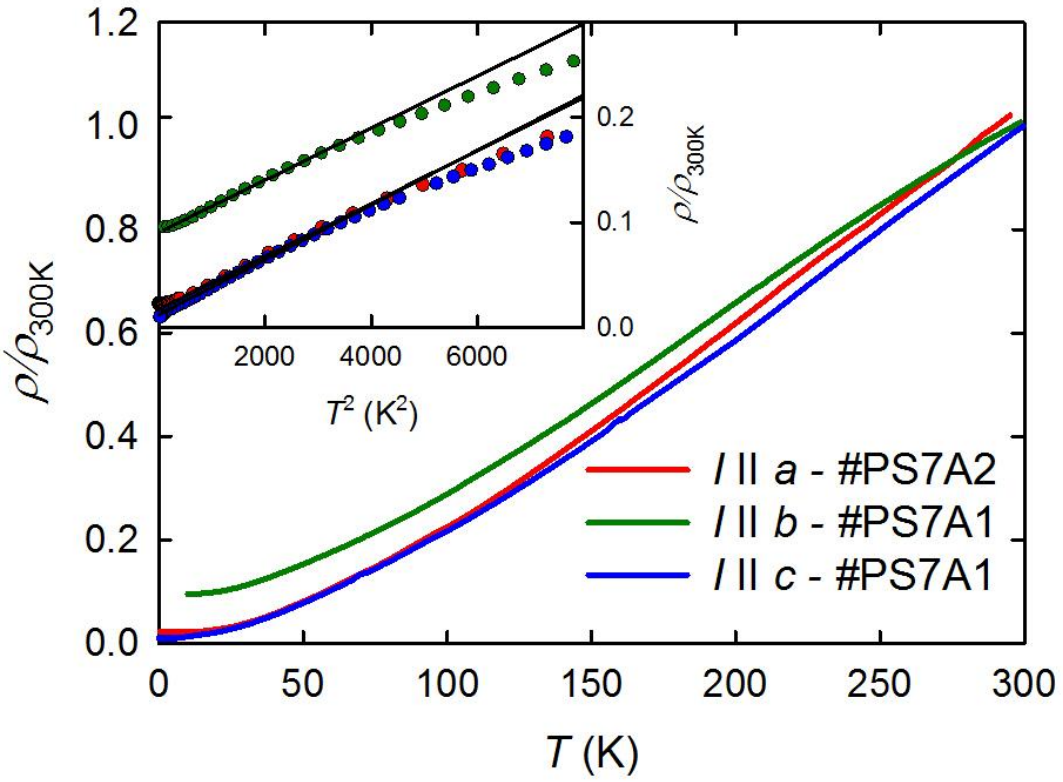

Fig. 5.6: The temperature dependences of electrical resistivity normalized to room temperature measured along main crystallographic axes of the sample #PS7A1 and a cut piece from it (#PS7A2). The inset displays fittings (black lines) of the low temperature data (full circles) to the formula mentioned in the text.

5.2.4. Electrical resistivity under high pressure

Our electrical resistivity data measured along the *c*-axis (sample #PS7A1) under high hydrostatic pressure, as shown in Fig. 5.7, again exhibited an anomaly around 3.5 K (1.4 GPa). It was slightly shifting with increasing pressure down to 2.7 K at 3.1 GPa. This feature was visible also in ambient pressure data (not shown). Since an application of a small magnetic field (> 0.3 T) restores

temperature-independent behavior between 5 and 2 K, we again attribute this again to the superconducting transition of Tin inclusions residing on the surface or inside the sample.

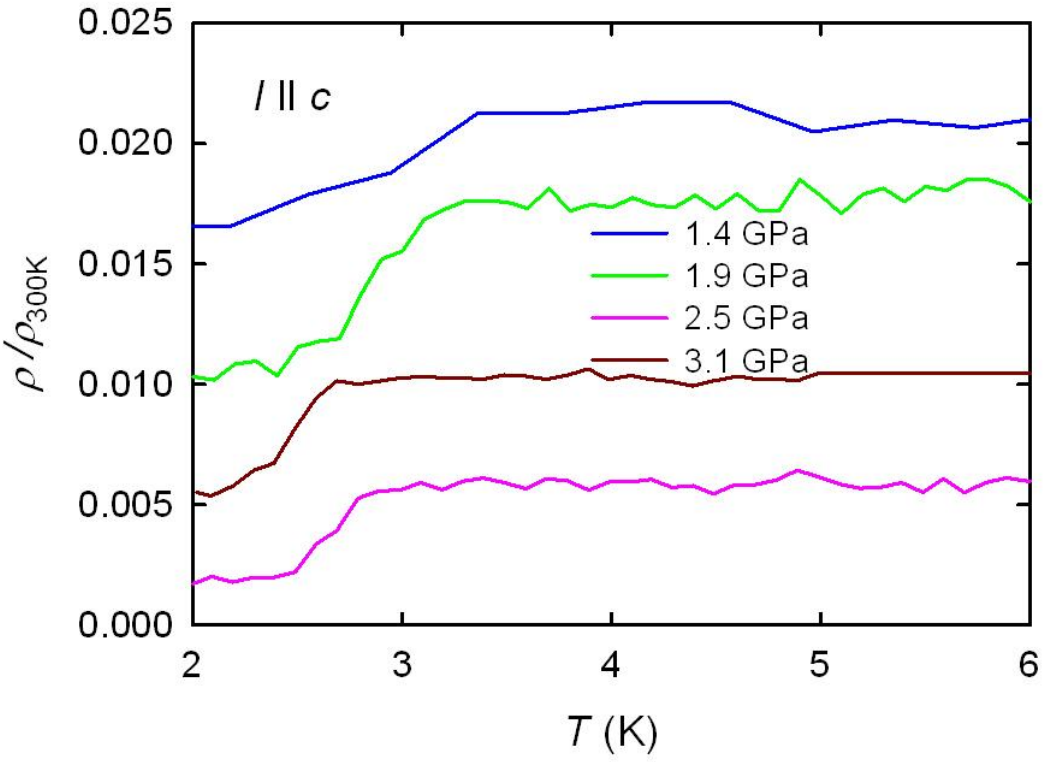

Fig. 5.7: Temperature scans of electrical resistivity measured along the *c*-axis of the sample #PS7A1 under various high pressures.

5.3. Discussion

Our measurements of $Yb_2Pt_3Si_5$ provided a basic knowledge about the crystal structure and the magnetic state of this novel compound. Although the compound is non-magnetic (at least down to 0.5 K), we have observed an interesting evolution of magnetic susceptibility with temperature due to a thermally induced ad-mixture of Ytterbium atoms in the magnetic 3+ valence state. Anisotropy of magnetic susceptibility is here a little bit weaker than in case of $YbPt_2Si_2$. On the other hand the similarity of spin-fluctuation temperatures for measurements taken along the *a*- and *c*-axis in contrast to the much higher value for the *b*-axis puts a question mark

about anisotropy, if the compound was driven into magnetically ordered state by e.g. high-pressure or an element substitution The electrical resistivity measurements under high-pressure did not reveal an emergence of magnetically ordered state at low temperatures, but this does not exclude that an application of higher-pressures (including uniaxial ones) would do so.

6. Summary and outlook of further research

The structural transitions taking place in CeRuSn were investigated by a large number of different experimental techniques, which prove their connection with the valence states of Cerium atoms. The similarity between the structural transitions in CeRuSn and the $\gamma \rightarrow \alpha$ transition in elemental Cerium was illustrated on the valence change and the crystal lattice contraction. But the complexity of the environment surrounding Cerium atoms still brings uncertainty about the correct interpretation of valence on the different Cerium sites. Although the structure was determined to be describable by a larger unit cell below the transitions, its precise form has to be confirmed by further measurements of single-crystal X-ray diffraction on high-quality single crystals. Similarly to the pure Cerium, the undergoing mechanism, which forces CeRuSn to change its structure on cooling, has not been clearly established yet. One of the possible explanations, the role of strong lattice vibrations, can be confirmed by inelastic neutron measurements.

At low temperatures we investigated and ascertained the magnetic anisotropy of the antiferromagnetically ordered state with magnetic moments lying in the *a*-*c* plane. This can be understood as a consequence of the anisotropic hybridization, which should be stiffer in the *a*-*c* plane, namely along the *c*-axis, to which the shortened Ce-Ru separations are almost parallel. According to our magnetization and specific heat data, two thirds of Cerium atoms should be intermediate-valent in the magnetically ordered state. Pressurizing CeRuSn has a very surprising impact on the ordering temperature, which grows contrary to the generally observed behavior in Ce-based compounds, where the ordering temperature is continuously suppressed by pressure towards a quantum critical point. Although the anisotropic compressibility can be anticipated considering the complicated crystal structure, further experiments utilizing uniaxial high-pressure measurements should be realized in the future. Another possibility would be using a chemical substitution in order to increase or shrink the crystal lattice. In addition, a substitution of some of Cerium atoms by non-magnetic ions would help to resolve the issue about the valence on different Cerium sites, especially if certain Cerium positions would be preferentially occupied by the substituting atoms.

The Ytterbium-based compounds, $YbPt_2Si_2$ and $Yb_2Pt_3Si_5$, studied in this thesis appeared to be in many aspects alike to each other, even though the quality of single-crystals was remarkably different. Both compounds were for the first time synthesized in form of single-crystals. They have a non-magnetic ground state owing to the presence of Yb^{2+} or intermediate valence state Ytterbium ions in the lattices. The magnetic Yb^{3+} state is (on our energy scale) not very distanced from the ground state and is hence thermally populated at temperatures close to room temperature. No magnetic ordering was induced by an application of high pressures during our studies. Experiments capable to reach higher pressures should be taken to fully exclude the conclusion that the compounds are much distanced from their quantum critical points. Also here a chemical substitution can be alternatively used to study the impact of changing the interatomic distances on the magnetic ground state. In case that these compounds are somewhere on the right side of the 2^{nd} QCP, expanding the lattice via chemical pressure by an element substitution or by hydrogenation would be the only possibility. The high quality of our $Yb_2Pt_3Si_5$ single-crystals is a precursor for performing further measurements involving de Haas van Alphen effect. This would provide information about the Fermi surface and would help in the explanation of the big difference among T_{sf} along different axes despite the lack of such significant anisotropy in the magnetic susceptibility.

Appendix A

Our low-temperature measurements on single-crystals of CeRuSn revealed an antiferromagnetic phase transition at 2.8 K The transition is clearly visible by a kink-like structure at ≈ 2.8 K in M/H *vs.* T. However, as is clearly visible in the panel 1 of Fig. A.1, M/H shows a tremendous increase starting already at ≈ 8 K. The onset of this additional contribution can be derived by the maximum in $\partial(M/H)/\partial T$ While in low field (0.01 T) the contribution is significant, in higher fields (0.1 T) it is largely suppressed. The 8 K feature may be attributed to a small amount of a ferromagnetic impurity residing in our sample. This would explain the pronounced appearance in small fields. At higher fields - when the denominator of the relation M/H, from which we count the magnetic susceptibility, is bigger – the enhancement below 8 K is negligible. Thus the field virtually suppresses the anomaly in magnetic susceptibility. In specific heat data, the impurity manifests by an enhancement starting at 8 K (panel 3 of Fig. A.1). In magnetic field the anomaly shifts to slightly higher temperatures as expected for a typical ferromagnet, because magnetic field in general stabilizes ferromagnetic ordering. For a ferromagnetic transition, one would expect a drop in electrical resistivity due to a decrease in the spin-dependent scattering. Indeed, we observe a tiny change in the slope of its temperature dependence at the same temperature, as it is shown in panel 2 of Fig. A.1. Comparing the first and the second temperature derivatives of magnetic susceptibility and electrical resistivity, respectively, we can see that the anomalous behavior starts at the same temperature yielding 7.7 K in both cases. As possible impurity Ce_5Sn_4 comes into focus. The compound orders ferromagnetically at 8 K [5]. Ce_5Sn_4 rapidly oxidizes on air, which could have made it invisible in initial EDX measurements, because it was covered by cerium oxide. Thus we have performed another EDX analysis on a sample with surface polished right before the measurement. Although none of our spectra had the 5:4 ratio for Ce:Sn, we have observed spectra where the amount of ruthenium was significantly reduced to some 15%. The rest of the intensity was divided between cerium and tin. The area belonging to this stoichiometry is denoted as No. 2 in Fig. 3.4. and the related spectrum is shown in Table 3.2. Spectra from the remaining area have the correct 1:1:1 stoichiometry. By comparing areas of the impurity and the main

phase, we have estimated the contamination to be in the order of only a few percent.

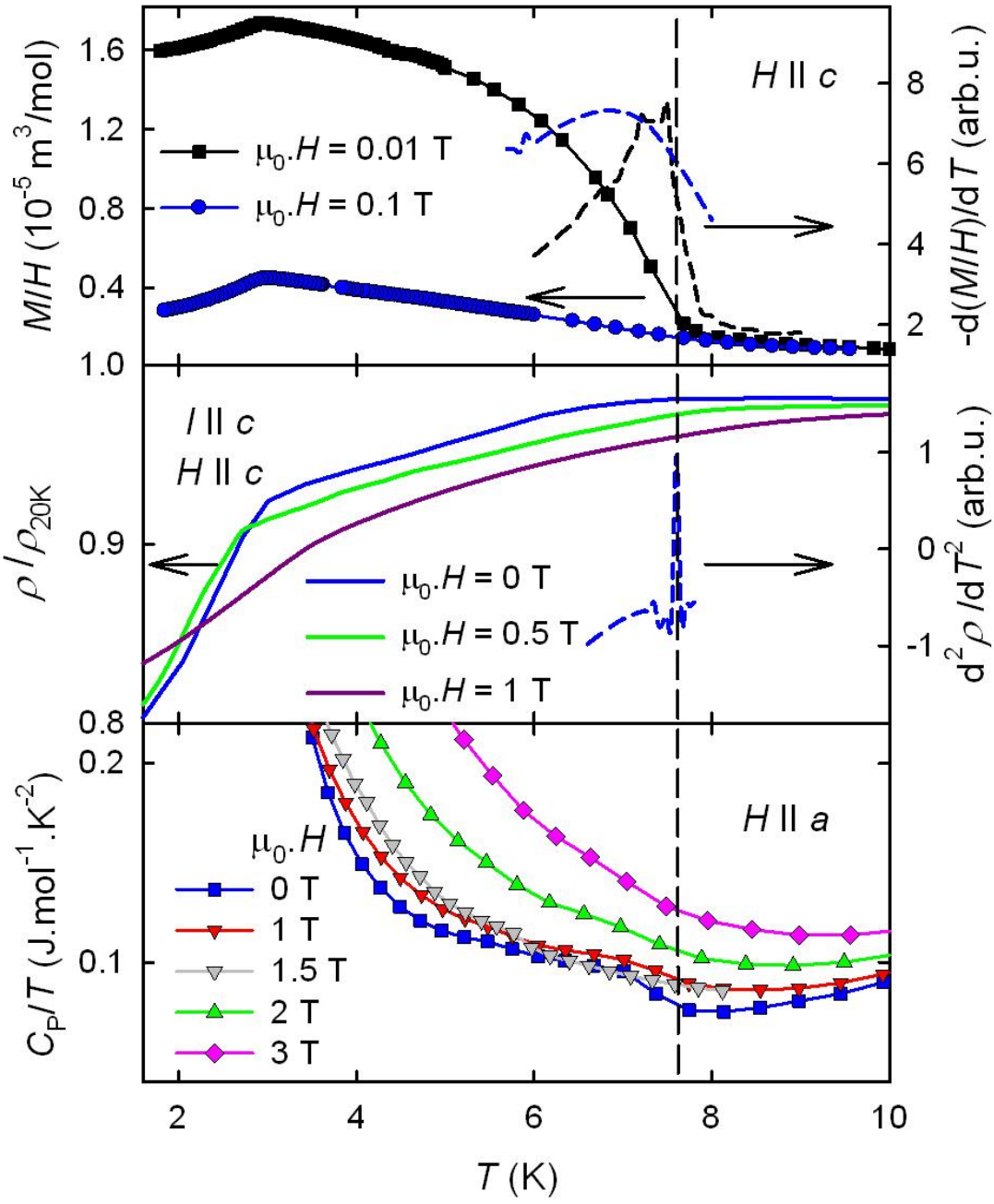

Fig. A.1. Panel 1 – *M*/*H* dependencies measured in two different fields along the *c*-axis. Their respective temperature derivatives are represented by dotted lines. Panel 2 – Electrical resistivity with magnetic field and current applied along the *c*-axis. The dotted line represents the second temperature derivative of the zero field curve.

Panel 3 – Specific heat divided by temperature at various fields applied along the *a*-axis. The vertical dashed line marks the temperature of 7.7 K where a maximum in $-\mathrm{d}(M/H)/\mathrm{d}T$ and $\mathrm{d}^2\rho/\mathrm{d}T^2$ has been found.

In order to reduce the amount of Ce_5Sn_4 in our single crystals, we have put more ruthenium into the source button for Czochralski method growth, see Table 3.1 in Section 4.2. Since the EDX only shows a small surface area/has limitations in resolution, the outcome of such investigation is rather arbitrary – means the impurity content could be reduced or the Ce_5Sn_4 phase is spread throughout the sample in smaller areas. Therefore we measured magnetization, which is very sensitive to its presence. Results of magnetic susceptibility measurements for various Ru excesses are shown in Fig. A.2. The enhancement at 8 K is clearly smaller already for the sample with 10 % Ruthenium excess. The fact that increasing the Ru amount is not followed by a continuous suppression of the 8 K anomaly, and additionally samples with same amounts of Ru excess deviate from one another, suggests that complete phase purity may not be achieved even for a higher ruthenium excess. Nevertheless the amount of Ce_5Sn_4 had been considerably reduced by our procedure. Furthermore, the anomaly in electrical resistivity has not been observed already for the lowest 10% Ru excess (not shown).

The incongruently grown CeRuSn goes in hand with the fact that large polycrystalline buttons of CeRuSn and additional buttons remaining from the Czochralski growth all contain unreacted ruthenium in their bottom parts. Powder X-ray diffraction pattern for CeRuSn is rather complicated due to the monoclinic crystal structure, which hides peaks belonging to Ce_5Sn_4. But more importantly, a careful look on the patterns revealed only a very tiny enhancement of intensity at the angle where the strongest reflection for Ce_5Sn_4 should occur. It should be pointed out that the spontaneous magnetization is approximately 2 μ_B/f.u. at 1.8 K for Ce_5Sn_4.(73) The offset in zero field value of magnetization in CeRuSn was only negligible. It supports our estimation of just a few percent of Ce_5Sn_4 in our samples.

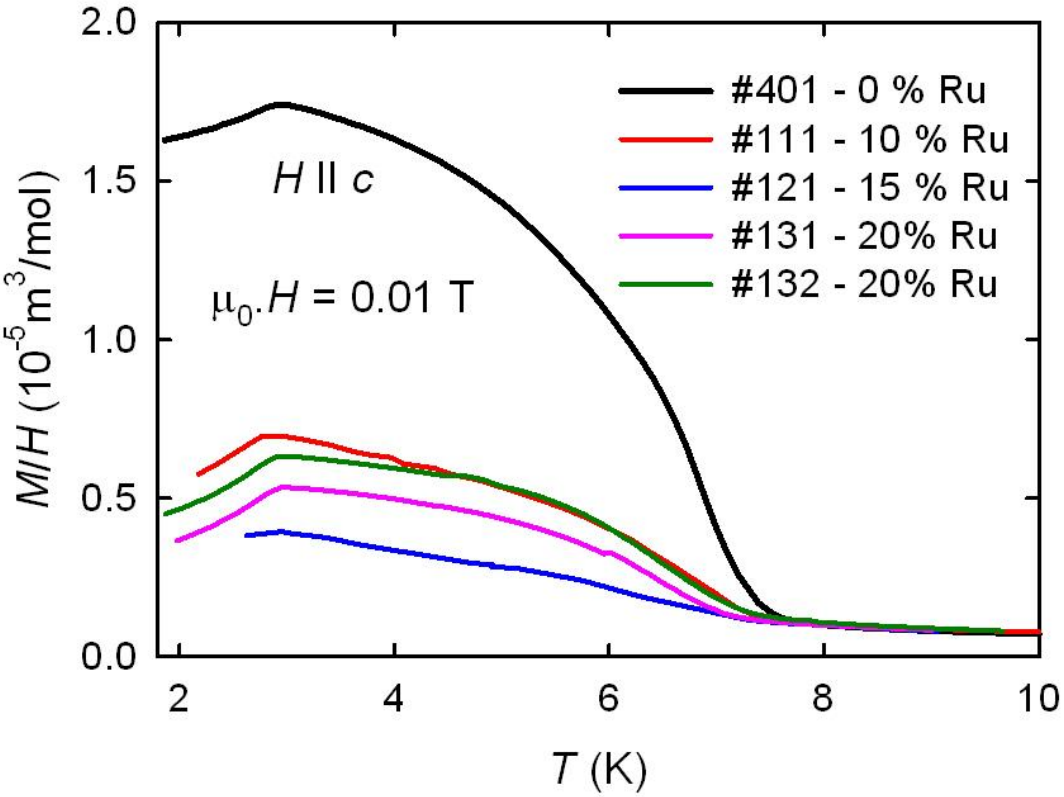

Fig. A.2. *M*/*H* temperature dependencies of various CeRuSn single crystals prepared from polycrystalline buttons containing different excesses of Ru measured in 0.01 T field along the *c*-axis.

Bibliography

1. B.K.Cho, P.C.Canfield, L.L.Miller, and D.C.Johnston (1995) Magnetism and superconductivity in single-crystal ErNi2B2C. *Phys. Rev. B* **52,** 3684.

2. P.C.Canfield, P.L.Gammel, and D.J.Bishop (1998) New Magnetic Superconductors: A Toy Box for Solid-State Physicists. *Physics Today* **51,** 40-46.

3. R.Valenzuela (2011) The Temperature Behavior of Resonant and Non-resonant Microwave Absorption in Ni-Zn Ferrites. In *Electromagnetic Waves*. In Tech.

4. N.Kioussis, B.R.Cooper, and J.M.Wills (1991) Magnetic instability with increasing hybridization in cerium compounds. *Phys. Rev. B* **44**.

5. M.A.Ruderman and C.Kittel (1954) Indirect Exchange Coupling of Nuclear Magnetic Moments by Conduction Electrons. *Phys. Rev.* **96,** 99-102.

6. T.KASUYA (1956) A Theory of Metallic Ferro- and Antiferromagnetism on Zener's Model. *Prog. Theor. Phys.* **16,** 45-57.

7. Q.G.Sheng and B.R.Cooper (1991) Absolute evaluation of combined hybridization-induced and RKKY-induced two-ion interaction in correlated electron systems. *J. Appl. Phys.* **69**.

8. J.H.van Vleck (1937) On the Anisotropy of Cubic Ferromagnetic Crystals. *Phys. Rev.* **52,** 1178.

9. B.D.Cullity and C.D.Graham (2005) In *Introduction to Magnetic Materials*. John Willie and Sons.

10. P.Blónski, A.Lehnert, S.Dennler, S.Rusponi, M.Etzkorn, G.Moulas, P.Bencok, P.Gambardella, H.Brune, and J.Hafner (2010) Magnetocrystalline anisotropy energy of Co and Fe adatoms on the (111) surfaces of Pd and Rh. *Phys. Rev. B* **81,** 104426.

11. R.Řezníček, V.Chlan, H.Štěpánková, P.Novák, and M.Maryško (2012) Magnetocrystalline anisotropy of magnetite. *J. Phys. : Condens. Matter* **24,** 055501.

12. B.Johansson and N.Martensson (1987) Thermodynamic aspects of 4f levels. In *Handbook on the Physics and Chemistry of Rare Earths* Vol. 10. Elsevier Science Publishers B. V..

13. D.T.Adroja, S.K.Malik, B.D.Padalia, S.N.Bhatia, R.Walia, and R.Vijayaraghavan (1990) Valence-fluctuation behavior of Yb ions and YbCuGa . *Phys. Rev. B* **42,** 2700.

14. J.Kondo (1964) Resistance Minimum in Dilute Magnetic Alloys. *Prog. Theor. Phys.* **32,** 37-49.

15. S.Doniach (1977) THE KONDO LATTICE AND WEAK ANTIFERROMAGNETISM. *Physica B* **91,** 231-234.

16. N.B.Brandt and V.V.Moshchalkov (1984) CONCENTRATED KONDO SYSTEMS. *Adv. Phys.* **33,** 373-468.

17. H.v.Löhneysen, A.Rosch, M.Vojta, and P.Wölfle (2014) Fermi-liquid instabilities at magnetic quantum phase transitions. *Rev. Mod. Phys.* **79,** 1015-1074.

18. T.Mito, S.Kawasaki, Y.Kawasaki, G.-q.Zheng, Y.Kitaoka, D.Aoki, Y .Haga, and Y.Onuki (2003) Coexistence of Antiferromagnetism and Superconductivity near the Quantum Criticality of the Heavy-Fermion Compound CeRhIn5. *PHYSICAL REVIEW LETTERS* **90**.

19. Y.Onuki, R.Settai, K.Sugiyama, T.Takeuchi, T.C.Kobayashi, Y.Haga, and E.Yamamoto (2004) Recent Advances in the Magnetism and Superconductivity of Heavy Fermion Systems. *Journal of the Physical Society of Japan* **73,** 769-787.

20. A.V.Goltsev and M.M.Abd-Elmeguid (2005) *J. Phys. : Condens. Matter* **17,** 813-821.

21. Z.Fisk (1971) THE EFFECT OF CRYSTAL FIELD SPLITTINGS ON THE ELECTRICAL RESISTIVITY OF NdB6. *Solid State Communications* **18,** 221-223.

22. R.J.Elliott and F.A.Wedgwood (1963) Theory of the Resistance of the Rare Earth Metals . *Proc. Phys. Soc.* **81,** 846.

23. H.Miwa (1962) *Prog. Theor. Phys.* **28,** 208-210.

24. P.Noziéres (1974) A "fermi-liquid" description of the Kondo problem at low temperatures. *Journal of Low Temperature Physics* **12,** 31-42.

25. P.W.Bridgman (1948) Rough Compressions of 177 Substances to 40,000 Kg/Cm? *Proc. Am. Acad. Arts Sci.* **76,** 71-87.

26. A.V.Andreev (1995) THERMAL EXPANSION ANOMALIES AND SPONTANEOUS MAGNETOSTRICTION IN RARE-EARTH INTERMETALLICS WITH COBALT AND IRON. In *Handbook of Magnetic Materials* Vol. 8.(Edited by K.H.J.Buschov), pp. 61-187. Elsevier Science.

27. J.J.Rhyne and S.Legvold (1965) Magnetostriction of Tb Single Crystals*. *Phys. Rev.* **138,** 507-514.

28. J.Czochralski (1918) Ein neues Verfahren zur Messung der Kristallisationsgeschwindigkeit der Metalle" [A new method for the measurement of the crystallization rate of metals]. *Zeitschrift für Physikalische Chemie* **92,** 219-221.

29. P.C.Canfield and Z.Fisk (1992) GROWTH OF SINGLE-CRYSTALS FROM METALLIC FLUXES. *Philosophical Magazine Part B* **65,** 1117-1123.

30. C.Hammond (2009) The diffraction of X-rays. In *Basics of Crystallography and Diffraction*. p. 221. Oxford University Press.

31. W.I.F.David (2002) Laboratory X-ray powder diffraction. In *Structure determination from powder diffraction data*. p. 55. Oxford University Press.

32. C.Hammond (2009) The diffraction of X-rays. In *The basics of crystallography and diffraction*. pp. 267-269. Oxfor University Press.

33. R.B.Von Dreele (2008) Rietveld Reifnement. In *Powder Diffraction: Theory nad Practise*. p. 266. Cambridge : Royal Society of Chemistry.

34. J.Rodríguez-Carvajal (1990) FULLPROF: A Program for Rietveld Refinement and Pattern Matching Analysis. *Journées de la Diffusion Neutronique*, 127.
35. G.M.Sheldrick (2007) Shell X. *Acta Crystallogr. Sect. A* **64**.

36. J.P.Eberhart (1991) WDX and EDX spectrometers. In *Structural and chemical analysis of materials : X-ray, electron and neutron diffraction : X-ray, electron and ion spectrometry : electron microscopy*. Bew York: Wiley.

37. Heat Capacity Option User's Manual (2004) Heat Capacity Option User's Manual . In *Physical Property Measurement System* . Quantum Design.

38. M.Rotter et al. (1998) *Rev. Sci. Instrum.* **69,** 2742.

39. H.Muller and M.Rotter (2012) Capacitance Dilatometer DIL20-11 - Users Manual. 2012. *Capacitance Dilatometer DIL20-11 - Users Manual*.

40. H.E.Kissinger (1957) Reaction Kinetics in Differential Thermal Analysis. *Analytical Chemistry* **29,** 1702-1706.

41. H.J.Bochhardt and D.Farrington (1957) The Application of Differential Thermal Analysis to theStudy of Reaction Kinetics. *Journal of the American Chemical Society* **79,** 41-46.

42. N.Murasawa, H.Koseki, X.-R.Li, Y.Iwata, and T.Sakamoto (2012) Study on Thermal Behaviour and Risk Assessment of Biomass Fuels. *International Journal of Energy Engineering* **2,** 242-252.

43. K.Murata, H.Yoshino, H.O.Yadav, Y.Honda, and N.Shirakawa (1997) *Rev. Sci. Instrum.* **68,** 2490.

44. J.F.Riecken, W.Hermes, B.Chevalier, R.-D.Hoffmann, F.M.Schappacher, and R.Pöttgen (2007) Trivalent-Intermediate Valent Cerium Ordering in CeRuSn A Static
Intermediate Valent Cerium Compound with a Superstructure of the CeCoAl Type. *Z. Anorg. Allg. Chem.* **633,** 1094-1099.

45. S.F.Matar, J.F.Riecken, B.Chevalier, R.Pöttgen, A.F.Al Alam, and V.Eyert (2007) Electronic and magnetic properties and chemical bonding of Ce*M*Sn „*M*=Rh,Ru… from first principles. *Phys. Rev. B* **76**.

46. R.Feyerherm, E.Dudzik, S.Valencia, J.A.Mydosh, Y.K.Huang, W.Hermes, and R.Pöttgen (2012) Complex charge ordering in CeRuSn. *Phys. Rev. B* **85**.

47. J.A.Mydosh, A.M.Strydom, M.Baenitz, B.Chevalier, W.Hermes, and R.Pöttgen. Hysteretic behavior and magnetic ordering in CeRuSn. PHYSICAL REVIEW B **83**, 054411-1-054411-6. 2011.

48. R.Feyerherm, E.Dudzik, K.Prokeš, J.A.Mydosh, Y.-K.Hua, and R.Pöttg (2014) Valence modulations in CeRuSn. *arXiv*.

49. K.Prokeš, V.Petříček, E.Ressouche, S.Hartwig, B.Ouladdiaf, J.A.Mydosh, R-D.Hoffmann, Y-K.Huang, and R.Pöttgen (2014) 3+1 dim stuctures CeRuSn. *J. Phys. : Condens. Matter* **26,** 122201-1-122201-6.

50. O.N.Carlson and F.A.SCHMIDT (1977) ELECTROTRANSPORT OF SOLUTES IN RARE EARTH METALS. *Journal of the Less-Common Metals* **53,** 73-84.

51. J.Fikáček, J.Prokleška, M.Míšek, J.Custers, S.Daniš, J.Prchal, V.Sechovský, and I.Císařová (2012) Physics of polymorphic transitions in CeRuSn. *Phys. Rev. B* **86,** 054108-1-054108-8.

52. F.Decremps, L.Belhaldi, D.L.Farber, K.T.Moore, F.Occelli, M.Gauthier, A.Polian, D.Antonangeli, C.-M.Aracne Ruddle, and B.Amaden (2011) Diffusionless gamma reversible arrow alpha Phase Transition in Polycrystalline and Single-Crystal Cerium . *PHYSICAL REVIEW LETTERS* **106,** 065701.

53. M.J.Lipp, A.P.Sorini, J.Bradley, B.Maddox, K.T.Moore, H.Cynn, T.P.Devereaux, Y.Xiao, P.Chow, and W.J.Evans (2012) X-ray Emission Spectroscopy of Cerium Across the ?-? Volume Collapse Transition. *PHYSICAL REVIEW LETTERS* **109,** 195705.

54. D.C.Koskenmaki and Jr. K.A.Gschneidner (1978) In *Handbook on the Physics and Chemistry of Rare Earths*.(Edited by Jr. K.A.Gschneidner and L.Eyring), p. 337. Elsevier Science Publishers B. V., Amsterdam.

55. M.N.Francillon and D.Jeromé (1973) LOW TEMPERATURE ELECTRICAL RESISTIVITY OF a-CERIUM UNDERPRESSURE. *Solid State Communications* **12,** 523-526.

56. J.W.Allen and R.M.Martin (1982) Kondo Volume Collapse and the y ~ a Transition in Cerium. *PHYSICAL REVIEW LETTERS* **49,** 1106-1110.

57. J.W.Allen and Z.Liu (1992) ALPHA-GAMMA-TRANSITION IN CE .2. A DETAILED ANALYSIS OF THE KONDO VOLUME-COLLAPSE MODEL. *Phys. Rev. B* **46,** 5047-5054.

58. I.-K.Jeong, T.W.Darling, M.J.Graf, T.Proffen, and R.H.Heffner (2004) Role of the Lattice in the $\gamma \rightarrow \alpha$ Phase Transition of Ce:A High-Pressure Neutron and X-Ray Diffraction Study. *PHYSICAL REVIEW LETTERS* **12**.

59. M.J.Lipp, .Jackson, H.Cynn, .Aracne, .J.Evans, and .K.McMahan (2008) Thermal Signatures of the Kondo Volume Collapse in Cerium. *PHYSICAL REVIEW LETTERS* **101**.

60. B.Johansson (1974) *Philosophical Magazine* **30,** 469-482.

61. F.M.Schappacher, P.Khuntia, A.K.Rajarajan, M.Baenitz, J.A.Mydosh, B.Chevalier, S.F.Matar, and R.Pöttgen (2012) Solid-state 119Sn NMR and Mössbauer Spectroscopic Studies of the Intermediate-valent Stannide CeRuSn. *Z. Naturforsch.* **67b,** 473-478.

62. K.Prokeš, J.A.Mydosh, O.Prokhnenko, W.-D.Stein, S.Landsgesell, W.Hermes, R.Feyerherm, and R.Pöttgen (2013) Antiferromagnetic ordering in a mixed-valent cerium compound CeRuSn. *Phys. Rev. B* **87,** 094421.

63. Fisher, M. E. (1962) Relation between the specific heat and susceptibility of an antiferromagnet. *Philosophical Magazine* **7,** 1731-1743.

64. H-Yamada and S.Takada (1972) Magnetoresistance due to Electron-Spin Scattering in Antiferromagnetic Metals at Low Temperatures. *Prog. Theor. Phys.* **49,** 1401-1419.

65. J.Mayer and P.D.Yetor (1977) MPt2Si2 compounds of the ThCr2Si2 type. *Journal of the Less-Common Metals* **55,** 171-176.

66. T.T.M.Palstra, A.A.Menovsky, G.J.Nieuwenhuys, and J.A.Mydosh (1986) Magnetic properties of the ternary compounds CeT2Si2 and UT2Si2. *Journal of Magnetism and Magnetic Materials* **54-57,** 435-436.

67. K.Hiebl and R.Pogl (1985) Magnetism and structural chemistry of ternary silicides: (RE, Th, U)Pt2Si2 (RE = rare earth). *Journal of Magnetism and Magnetic Materials* **55,** 39-48.

68. Dhar, S. K., E. V. Sampathkumaran, N. Nambudripad, and R. Vijayaraghavan (1988) Heat capacity and magnetic susceptibility of mixed valent YbPt2Si2. *Solid State Communications* **67,** 949-951.

69. B.C.Sales and D.K.Wohlleben (1975) Susceptibility of Interconfiguration-Fluctuation Compounds*. *PHYSICAL REVIEW LETTERS* **35,** 1240-1244.

70. R.W.Shaw, D.E.Mapother, and D.C.Hopkins (1960) Critical Fields of Superconducting Tin, Indium, and Tantalum*. *Phys. Rev.* **120,** 88-91.

71. J.P.Perdew and Y-Wang (1992) Accurate and simple analytic representation of the electron-gas correlation energy. *Phys. Rev. B* **45,** 13244.

72. P.Blaha, K.Schwarz, G.K.H.Madsen, D.Kvasnicka, and J.Luitz (2001) *Vienna University of Technology*.

73. F.Givord, P.Jelay, A.Munoz, and J.Schweizer (1992) Magnetic structures of Ce-rich compounds Ce5Sn3 and Ce5Sn4. *Journal of Magnetism and Magnetic Materials* **116,** 419-431.

List of Tables

List of Abbreviations

RKKY	Rudermann-Kittel-Kasuya_yosida interaction
MAE	magnetocrystalline anisotropy energy
QCP	quantum critical point
NFL	non-Fermi liquid
RRR	residual resistivity ratio
EDX	energy dispersive X-ray analysis
PPMS	Physical Property Measurement System
MPMS	Magnetic Property Measurement System
SQUID	Superconducting Quantum Interference Device
CC	closed-cycle refrigerator
VSM	Vibrating Sample Magnetometer
DTA	differential thermal analysis
RT	room temperature
XANES	X-ray Absorption Near Edge Structure
ST	structural transitions
CEF	crystal electric field
S	Cerium sites with shortly-distanced Ruthenium neighbors
L	Cerium sites with long-distanced Ruthenium neighbors

I	Cerium sites with intermediate-distanced Ruthenium neighbors
AFM	antiferromagnetic
ZFC	zero-field cooled
FC	field cooled
MT	metamagnetic transition(s)
MR	(longitudinal) magnetoresistance
PM	paramagnetic phase
IFM	induced spin-polarized phase